

University of Southampton Research Repository

Copyright © and Moral Rights for this thesis and, where applicable, any accompanying data are retained by the author and/or other copyright owners. A copy can be downloaded for personal non-commercial research or study, without prior permission or charge. This thesis and the accompanying data cannot be reproduced or quoted extensively from without first obtaining permission in writing from the copyright holder/s. The content of the thesis and accompanying research data (where applicable) must not be changed in any way or sold commercially in any format or medium without the formal permission of the copyright holder/s.

When referring to this thesis and any accompanying data, full bibliographic details must be given, e.g.

Thesis: Author (Year of Submission) "Full thesis title", University of Southampton, name of the University Faculty or School or Department, PhD Thesis, pagination.

Data: Author (Year) Title. URI [dataset]

University of Southampton

Faculty of Engineering and Physical Sciences Department of Aeronautical and Astronautical Engineering

Experimentally Modelling Urban Air Pollution and Measuring Turbulent Dispersion

DOI: n/a

by

Tomos Jared Rich

MSc BEng

ORCiD: 0000-0002-6259-4225

A thesis for the degree of Doctor of Philosophy

February 2025

University of Southampton

Abstract

Faculty of Engineering and Physical Sciences
Department of Aeronautical and Astronautical Engineering

Doctor of Philosophy

Experimentally Modelling Urban Air Pollution and Measuring Turbulent Dispersion

by Tomos Jared Rich

The study of urban aerodynamics is a field of aerospace engineering that falls into the broader category of wind engineering. Within this field, there is interest in modelling both the dispersion of pollutants as well as the air flow around buildings. In this thesis, urban air pollution is experimentally modelled as a neutrally buoyant scalar introduced into a scale-model urban landscape. The aim of the experiments that were carried out was to obtain high-fidelity measurements of turbulent diffusion processes in idealised and realistic landscapes.

All experiments were carried out in the University of Southampton's recirculating water tunnel using simultaneous Particle Image Velocimetry (PIV) and Planar Laser Induced Fluorescence (PLIF). The investigation into the accuracy of the PLIF technique revealed some problems in the way that attenuation is corrected for in existing PLIF studies. These were fixed in a version of a PLIF post-processing code that is aimed to be published in the future. A verification study proved the accuracy of this code by calculating the known flow rate of a scalar jet within experimental uncertainty values.

The data acquired in these experiments has provided insights into both simplified and realistic flows. The investigation into flow structures around an individual building was carried out for a case with scalar plume impingement below the leading edge stagnation point of the building. It was shown that, for this case, the scalar was drawn into the leading horseshoe vortex and formed a dual plume shape behind the building with very little vertical scalar transport. The measurements of a scalar plume in a scaled urban model showed a deflection in the direction of plume propagation from the mean flow direction. It could also be seen that the tallest buildings had a disproportionately large effect on flow fields in their local area with regard to both velocity and scalar concentration statistics.

Contents

Li	st of 1	Figures	3	ix
D	eclara	ation of	f Authorship	xv
A	cknov	wledge	ments	xvii
N	omen	clature	?	xix
1	Intr	oductio		1
	1.1		n Air Pollution	1
	1.2		rch Problem	2
	1.3	Orgar	nisation of Thesis	4
2	Lite	rature l	Review	5
	2.1	Urbar	n Flow	5
		2.1.1	The Thermally Neutral Atmospheric Boundary Layer	5
		2.1.2	Defining Urban Length-scales	7
		2.1.3	Turbulent Characteristics: The Roughness Sublayer and the Log-	
			Law Region	7
		2.1.4	Homogeneous Surface Conditions and the Meteorological Approach	
	2.2		llence Characteristics and Species Flux	10
		2.2.1	Defining Species Transport	10
		2.2.2	Existing Approaches to Modelling Species Transport	11
		2.2.3	Gaussian Plumes	12
	2.3		sed Roughness	13
		2.3.1	Single Cube Approximations	13
		2.3.2	Defining an Array	14
		2.3.3	Street Canyons	16
		2.3.4	Scalar Source type and sensitivity	17
	2.4	2.3.5	A Note on Urban Comparison	19
	2.4		tigations into Realistic Urban Environments	19
		2.4.1	Velocity Measurements in Real Cities	19
			Concentration Measurements in Real Cities	20
	2 5	2.4.3	Dispersive Flux Measurements over Realistic Scaled Models	20
	2.5	2.5.1	imental Approaches	21 21
		2.5.1	Why Experiments are Necessary	
		2.5.2	Water Tunnel Experiments	22
	2.6		Sap in the Literature	23
	∠.∪	1116 0	Bay III LIC LICIALUIC	20

vi *CONTENTS*

3	Met	hodolo	ogy	25
	3.1	Detail	ls of the Flow Setup	25
		3.1.1	The Water Tunnel Facility	25
		3.1.2	Atmospheric Boundary Layer	26
	3.2	Meası	urement Techniques	27
		3.2.1	Particle Image Velocimetry	27
		3.2.2	Basics of Planar Laser Induced Fluorescence	29
		3.2.3	Combined PIV-PLIF	31
	3.3	Know	on issues to be addressed when conducting PLIF	32
		3.3.1	Non-linearity of the dye response	32
		3.3.2	Secondary Fluorescence Effects	33
		3.3.3	Attenuation in Calibration	33
		3.3.4	Fluctuations in laser intensity	34
	3.4	Metho	odology study into calibration methods and accuracy	34
		3.4.1	Developing improvements to the PLIF methodology	36
	3.5	Exper	riments overview	37
		1		
4			ogy: Advancement of the Planar Laser Induced Fluorescence Tech	
	niqu			39
	4.1		nar Laser Induced Fluorescence Software Package	39
		4.1.1	Summary	39
		4.1.2	Statement of Need	40
		4.1.3	Package Overview	41
		4.1.4	Package Functions	43
		4.1.5	PLIF Calibration functions - Calculate Calibration	43
		4.1.6	PLIF Processing Function - Apply Calibration	44
		4.1.7	Epsilon Optimisation Function (Optional)	44
		4.1.8	File Accessing Sub-functions	44
		4.1.9	Acknowledgements and Author Contribution Statement	45
	4.2		sing the accuracy of the Planar Laser Induced Fluorescence tech-	
			using a Mass Balance experimental case	45
		4.2.1	Introduction	46
		4.2.2	Methodology	46
		4.2.3	Explanation of PLIF Calibration Process	48
		4.2.4	Results	50
		4.2.5	Attenuation Correction	53
		4.2.6	Conclusion	54
5	Do11	utant T	Dispossion Around a Single Tall Building	55
3	5.1		Dispersion Around a Single Tall Building	55 55
	5.2		ture Review	57
	5.3			60
	5.4		odology . .	65
	J. 4	5.4.1		65
		9.4.1	Centre-plane measurements	65
			5.4.1.2 Turbulence Statistics	65
				66
			5.4.1.3 Species Mean and Variance	66
		5.4.2		69
		J.4.Z	Cross-stream measurements	09

CONTENTS vii

		F 4 O 4 N X X 1 1	60
		5.4.2.1 Mean Velocity	69
		5.4.2.2 Cross-stream concentration measurements	71
		5.4.2.3 Turbulent and Advective Structures	72
		5.4.3 Discussion	73
	5.5	Conclusions	74
6	Scal	-model Experiments of Turbulent Dispersion over a Realistic Urban Envi-	
	roni	ent	77
	6.1	Literature Review	78
		6.1.1 Experimental Urban Cases	78
	6.2	Methodology	80
	6.3	Results	84
		6.3.1 Characterisation of the Flow	84
		6.3.2 Characteristics of the Plume	86
		6.3.3 The Components of Flux	92
	6.4	Discussion	95
		6.4.1 The Fluid Dynamic Characteristics of a City	95
		6.4.2 With Regards to Modelling the Plume	96
	6.5	Conclusion	97
7	Con	lusions	99
	7.1	Summary of Content	99
	7.2	· · · · · · · · · · · · · · · · · · ·	101
			102
		T	102
			103
	7.3		103
Re	eferer	ces	105

List of Figures

2.1	This figure depicts the thickening of the ABL over a city and the different flow regimes within (Fernando 2010).	6
2.2	The roughness sublayer created by flow over an urban environment (Bar-	
2.3	low 2014)	14
2.4	Regular staggered arrays, with (b) and without (a) height variation (Boppana et al. 2010)	15
2.5	Vertical turbulent diffusivity around a tall building in a regular array, with turbulent diffusivity (<i>D</i>) calculated as $\overline{c'w'\frac{h^2}{Q}}$ (Fuka et al. 2018). In which <i>Q</i> is the mass flow rate at the source, <i>h</i> is the building height, <i>c'</i> is the fluctuating concentration, and <i>w'</i> is the fluctuating vertical velocity component.	18
2.6	The experimental setup used to approximate an atmospheric boundary layer by Tomas et al. (2017)	22
3.1	The Recirculating Water Tunnel at the University of Southampton's Boldrewood Innovation Campus	25
3.2	A plan view of the initial version of the roughness elements that were intended to create an atmospheric boundary layer	26
3.3	The atmospheric boundary layer false floors, with test section used in chapter 6, prior to installation in the water tunnel	27
3.4	An example schematic of a PIV setup, (From Von Karman Institute PIV Training 2021.)	28
3.5 3.6	Emittance and absorbance spectrum of Rhodamine 6G (Baj et al. 2016) A graph showing fluorescent light intensity against dye concentration in a study into the PLIF calibration process. Error bars were calculated using the variance in fluorescence across each tank, and the uncertainty in dye concentration	30
3.7	An image of one of the calibration tanks	36
4.1	A diagram of an example PLIF experimental setup	40
4.2	A diagram of PLIF post processing	42
4.3	A diagram showing a top and side view of the experimental setup used to measure the Rhodamine 6G jet	46
4.4	Photos showing the experimental setup used during this investigation	47
4.5	(a) The mean streamwise velocity, and (b) the streamwise velocity variance. These were averaged from 2000 PIV images	50
4.6	The mean concentration field across the jet, calibrated with an attenuation correction. The centreline of the jet is indicated by the black line.	51

X LIST OF FIGURES

4.7	A comparison of profiles of the mean dye concentration. Calibrated both with and without an attenuation correction. These profiles were extracted at $x/D = 80$	51
4.8	A full field of the mean mass flow rate calculated across the jet. The area used to calculate the absorptivity (ϵ) necessary for the attenuation correc-	
4.9	tion used in figure 4.9, is shown bordered by the black lines Light intensity measured in the calibration tanks against the concentration of the tanks, when corrected for attenuation. The linear fit is between the points at $C = 0.03$, $C = 0.05$, and the origin. The background value at $C = 0.00$ is included for reference	53 54
5.1	(a) The flow structures around the front, top, and side faces of a bluff body attached to a wall. (b) The flow structures in the wake of the same bluff body. Both figures (a) and (b) are inspired by the work of Martinuzzi and	
5.2	Tropea (1993)	57 60
5.3	A diagram of the cross-stream measurement setup used for stereo PIV and PLIF. This setup allows measurement of an area 7H tall by 5H wide (210mm by 150mm).	61
5.4	A photo taken inside the University of Southampton's recirculating water tunnel while fully drained. This photo is taken from the test section looking upstream, it shows the upstream roughness and spires used to	01
5.5	generate an incoming atmospheric boundary layer	62
5.6	coming flow that was averaged in the streamwise direction (a) The extent of the recirculation region in the wake of the tall building, defined as a contour of zero streamwise velocity. Contour is on a plot of normalised streamwise velocity (U/U_{∞}) . (b) The velocity deficit $(U-U_{BL})/U_{\infty}$ in the wake of the tall building. The extent of this region is defined as a contour of $U=0.95*U_{BL}$. (c) The normalised vertical velocity	63
	(W/U_{∞}) in the vicinity of the tall building	64
5.7 5.8	The $u'w'$ Reynolds Stress component around the tall building (a) Three instantaneous slices of species concentration near the tall build-	66
3.6	ing on a log_{10} scale, normalised by the source concentration; the three slices were taken at different times and were later stitched together. (b) The mean species concentration around the tall building on a log_{10} scale, normalised by the source concentration. (c) The species variance, also normalised by source concentration and shown on a log_{10} scale. In all three figures dotted lines represent the lines along which different datasets have been stitched together	67
5.9	(a) The vertical turbulent flux field $(\overline{c'w'}/C_sU_\infty)$. (b) The vertical advective	07
	flux field (CW/C_sU_∞)	68

LIST OF FIGURES xi

5.10	(a) The mean vertical velocity W (m/s) at the closest PIV measurement to the front of the tall building ($x/H = 4.98$), showing the stagnation point (marked with an X) across this leading face is at $z/H = 0.62$. (b) The concentration profile at the same x location as this PIV measurement, nor-	
	malised by source concentration. (c) The cumulative total of the concentration profile shown in (b), normalised by the sum of this profile	69
5.11	(a) Cross-stream slices of mean streamwise velocity normalised by the local freestream velocity, this being $0.77*U_{\infty}$, as calculated using data shown in figure 5.5. (b) A comparison of the stereo and planar PIV results at each downstream distance in which stereo data was aquired. Data from planar	
5.12	PIV is shown in light blue, data from stereo PIV is shown in dark red Species concentration downstream of the tall building on a log_{10} scale, normalised by source concentration. The values of contour lines are displayed on the colour bars of each figure. Downstream distances shown in (a) and (b) are equal to $x - x_B = 2H$ and $x - x_B = 12H$. Only these two slices were shown for the sake of clarity, the other four are positioned in-between these two and do not reveal anything different to the relationship visible in these two. The two figures are not shown on the same colour map due to the in-	70
5.13	tensity in scalar measured varying significantly between the two planes (a) The Vertical Advective flux field (CW/C_sU_∞) . (b) The Horizontal Advective flux field (CV/C_sU_∞) . (c) The Vertical Turbulent flux field $(\overline{c'v'}/C_sU_\infty)$. (d) The Horizontal Turbulent flux field $(\overline{c'v'}/C_sU_\infty)$. All plots are taken from $x-x_B=2H$ downstream of the tall building, or $x=7.71$ downstream of the dye source. All have contours of mean concentration super-	
5.14	imposed for clarity, the values of these contours are visible in figure 5.12a. A diagram of the regions of highest dye concentration, based on the data from both experimental setups. This is intended as a qualitative figure to show the observed effect that the plume is impinging below the building stagnation, and then being trapped in the horseshoe vortex	72 73
6.1	A map of the centre of Southampton with a zoom in on the experimental area under investigation. The predominant wind direction is marked and this was used as the flow direction when the model was in the water tun-	
6.2	nel. This figure was generated using ordnance survey data	80
6.3	ness elements are visible, followed by the 3D printed city model A diagram of the experimental setup used during acquisition of streamwise planar PIV-PLIF. An example un-calibrated PLIF image is shown under the laser sheet	81 81
6.4	The 3D model that was used to generate the experimental 3D print. Dashed lines indicate the planes of the stream-wise vertical measurements. Green areas indicate the field of view of the wall-parallel measurements. Locations that the vertical profiles in figure 6.6 were extracted are represented as nine red dots. The relative location of the scalar point source has been indicated outside the model. This 3D model was produced using Ordnance Survey data	82

xii LIST OF FIGURES

6.5	(a) The incoming streamwise flow velocity U/U_{∞} . (b) The incoming streamwise flow velocity normalised by the friction velocity (U^+), plot on a semi-	
	log scale so that the log law region of the boundary layer can be observed. (c) The profile of the variance of the streamwise velocity $\overline{u'u'}/U_{\infty}^2$ of the incoming flavor (d). The profile of the Power aldo stress $\overline{u'u'}/U_{\infty}^2$ of the incoming flavor (d).	
	incoming flow. (d) The profile of the Reynolds stress $\overline{-u'w'}/U_{\infty}^2$ of the incoming flow. On plots (a), (c), and (d) error bars of one standard deviation	
	are displayed in grey representing the uncertainty in the region of the incoming flow that was averaged in the streamwise direction.	84
6.6	Vertical profiles of the streamwise velocity U/U_{∞} , extracted at locations shown in figure 6.4. The profiles in line with the tall building are shown	
	in dark red, all others are shown in light blue. These are the left column of red dots on figure 6.4	85
6.7	Mean streamwise velocity fields above the city model normalised by U_{∞} , (a) shows data on the centerline and (b) shows data at $(y/H = -5)$	86
6.8	Examples of the planar concentration results used to define the scalar plume taken from the planar slice at $y/H = -5$, all shown on log scales for clar-	
	ity. (a) An example of the instantaneous results. (b) The mean concentration field along this slice. (c) The concentration variance field. These	
	fields were all calculated using two stitched fields of view taken at differ-	
6.9	ent times which were normalised by their source release concentration C_s . A figure showing the vertical growth of the scalar plume. This was cal-	87
	culated using the local half height at half max and plot against the down-	
	stream distance (x/H) . Both axis are on a log scale and each line represents a different cross stream location. This is with the exception of the final line	
<i>(</i> 10	in the legend, which is a reference value for the exponent of 0.5	88
6.10	(a) A map of the plume width defined using an isocontour of mean concentration calculated from profiles of the planar concentration slices as	
	shown in figure 6.8b. These profiles were taken at $z/H=3$ and extrapolated spanwise as a Gaussian profile with a zero offset, example profiles	
	are shown in (b). The displacement of the centre of the mean plume is shown in blue. The best-fit line in green shows the centre follows a mean	
	direction of 4.5 degrees to the left of the mean flow direction. (c) A map of	
	the upper limit of the plume as defined as the isosurface of 0.002 percent of the source concentration. The displacement of the centre of the mean	
	plume is shown in blue. The best-fit line in green shows the centre follows	
	a mean direction of 5.1 degrees to the left of the mean flow direction. (d) Examples of the data used to calculate the cross-stream profiles of plume	
	height. This data was extrapolated using a Gaussian fit	89
6.11	A zoomed section of the planar slice taken at $y/H = -5$, shown fully in figure 6.8. (a) Mean concentration on a log_{10} scale. (b) The vertical advec-	
	tive flux CW. (c) The vertical turbulent flux $\overline{c'w'}$. The area zoomed in on in	
	this figure is at a location that a measurement plane intersects with one of the longest street canyons in the model	90
6.12	(a) Plume half width against increasing downstream distance from the	
	scalar source, this is defined using the half-max. This curve follows equation 6.3 where $c = 0.90$ and is only fit to data beyond $x/H = 20$. (b) Plume	
	half width against increasing downstream distance from the scalar source, this is defined using the half-height of the isosurface. This curve follows	
	equation 6.3 where $c = 0.55$ and is only fit to data beyond $x/H = 20$	91

LIST OF FIGURES xiii

6.13	Figures (a) and (b) show the vertical advective scalar flux field on the centreline and profiles extracted from this field respectively. Figures (c) and (d) show the vertical turbulent scalar flux field on the centreline and profiles extracted from this field respectively. Figures (e) and (f) show the vertical advective scalar flux field at $y/H = -5$ and profiles extracted from this field respectively. Figures (g) and (h) show the vertical turbulent scalar flux field at $y/H = -5$ and profiles extracted from this field respectively.	
	All scalar flux fields are shown on the same colourmap and all profiles are	
	scaled the same as each other to aid in comparison.	93
6.14	The vertical turbulent and advective flux fields above the centreline and	
	tallest building of the city model, as marked in figure 6.4. Planes (a) and (b)	
	were extracted at position 1 in figure 6.4, graphs (c) and (d) were extracted	
	at position 2. These slices were extracted at 3H (60 mm) above the tunnel	
	floor. The location of the tall building is outlined by a black rectangle in	
	figures 6.14 (c) and 6.14 (d)	94

Declaration of Authorship

I declare that this thesis and the work presented in it is my own and has been generated by me as the result of my own original research.

I confirm that:

- 1. This work was done wholly or mainly while in candidature for a research degree at this University;
- 2. Where any part of this thesis has previously been submitted for a degree or any other qualification at this University or any other institution, this has been clearly stated;
- 3. Where I have consulted the published work of others, this is always clearly attributed;
- 4. Where I have quoted from the work of others, the source is always given. With the exception of such quotations, this thesis is entirely my own work;
- 5. I have acknowledged all main sources of help;
- 6. Where the thesis is based on work done by myself jointly with others, I have made clear exactly what was done by others and what I have contributed myself;
- 7. Parts of this work have been published as: Rich T, Vanderwel C (2024) Pollutant dispersion around a single tall building. Boundary-Layer Meteorology 190(8):34

Signed:	Date:
_	

Acknowledgements

I would like to thank my supervisory team. My co-supervisors Dr Desmond Lim, and Professor ZhengTong Xie, and particularly my main supervisor Professor Christina Vanderwel. This PhD would not have been possible without all their support.

Nomenclature

Α	Absorbance
A	Ansornance

a PLIF calibration constant / curve fitting variableb Background light intensity / curve fitting variable

 b_i Local background light intensity, as a function of image number

C Mean concentration
 c Curve fitting variable
 c'c' Concentration variance

 c_{cal} Concentration of dye in a calibration tank

 C_i Instantaneous concentration C_s Scalar release concentration

 C_{total} Total concentration

CU Streamwise advective scalar flux c'u' Streamwise turbulent scalar flux CV Cross-stream advective scalar flux c'v' Cross-stream turbulent scalar flux

CW Vertical advective scalar flux c'w' Vertical turbulent scalar flux

d Curve fitting variable

D Jet diameter

 D_{ij} Turbulent diffusivity tensor

E Fluorescent emittance

 e_i Local experimental image light intensity, as a function of image number

FAC2 Ratio of points within a factor of 2 when comparing 2 simulations

H Local lengthscale

 H_{Bmax} Height of the tallest obstacle to the flow

I Laser light intensity

 i_{cal} Light intensity measured from a calibration tank

J Species fluxL Reference length

*m*_{rhodamine} Mass flow rate of Rhodamine 6G

 m_{cal} PLIF Calibration gradient

r Path length

Re Reynolds number

 Re_{τ} Friction Reynolds number

XX NOMENCLATURE

Sc	Schmidt number
Q	Volume flow rate
r	Laser path length
и	Streamwise velocity
U_BL	Streamwise velocity in the boundary layer without model present
u'u'	Streamwise velocity variance
u'w'	Reynolds shear stress
u_{τ}	Friction velocity
U_{∞}	Freestream velocity
v	Cross-stream velocity
w	Vertical velocity
\boldsymbol{x}	Streamwise coordinate
x_B	Distance behind building
y	Cross-stream coordinate
z	Vertical coordinate
z_0	Roughness length
$Z_{0.002\%}$	Maximum height at which a scalar concentration of 0.002% is detected
γ	Molecular diffusivity
ϵ	absorptivity
η_{eta}	Batchelor length scale
η	Kolmogorov length scale
κ	von Karman constant
λ_F	Frontal solidity
λ_F	Planform density

Density

Dynamic viscosity

ρ

μ

Chapter 1

Introduction

1.1 Urban Air Pollution

Air pollution is a risk factor to human health for which it is difficult to fully quantify either the threat it poses, or the concentration present in a particular location. The negative health effects of air pollution can be severe (Dziubanek et al. 2017) with the highest impact being on respiratory and cardiac based conditions (UK Government 2024), and people living in cities are exposed to a significantly higher amount than people living in rural environments. With the proportion of the world's population living in urban environments increasing (United Nations Department of Economic and Social Affairs 2018), it is becoming increasingly urgent to be able to predict the intensity of air pollution exposure.

Weather forecasting and air quality forecasting are both dependent on the computational modelling of urban wind patterns. Two of the primary providers of this data within the UK are the Department of Environment, Food, and Rural Affairs (DEFRA) and the Met Office. DEFRA uses a range of modelling techniques to predict air quality, which range from simple ones that can run on a personal computer to advanced models that necessitate the use of a high-performance-computer (HPC) (Williams et al. 2011). The work of DEFRA is focused on broad trends and national averages. The Met Office produces more of the general weather forecasts within the UK, but also models air quality (Met Office 2022; Bermous and Steinle 2015). In order to produce these weather forecasts and predict air quality, the Met Office has exclusive use of an HPC that, at the time of its launch in 2016 was ranked within the top 50 most powerful computers in the world (Met Office 2016). However, these forecasts are still produced at a relatively coarse resolution. The highest resolution that the Met Office runs at, in more than an experimental capacity, is 1.5 km in the inner domain of its UK atmospheric simulation (Met Office 2024). For global simulations, the Met Office uses a much larger grid resolution of 20 km. There is also a growing interest in creating more detailed simulations that resolve individual buildings. For example, London city council has recently introduced new guidance that large new building developments within

London must conduct studies on their potential influence on the local urban micro-climate (City of London 2022). This shows the increasing awareness of the importance of urban micro-climates and air quality.

Information about the spread of pollutants is also useful for more specific applications. In the case of Clements et al. (2024), a pollutant plume from an urban fire was analysed both computationally and using sensors in the field. This allowed the authors to demonstrate that, given enough data about the fire and meteorological conditions, the pollutant concentration downstream could be calculated with a reasonable degree of accuracy. This verifies the use of simplified fast response models for the calculation of public exposure to pollutants in emergency situations. Alternatively, air pollution sensor data can be used to solve the inverse problem of identifying pollutant sources, as was shown by Vanderwel et al. (2024).

Computational models for urban air flow and air pollution like those detailed above are popular because of their speed and convenience. However, realistic data remains crucial for the development and calibration of these models. Acquiring realistic data for this purpose can only be done through either sensor data in real world scenarios, or through scaled experiments in wind or water tunnels.

This project has a specific focus on studying air pollution within Southampton. This is not just due to the fact that it is being carried out at the University of Southampton, but also because Southampton has higher levels of air pollution than you would expect for a city of its size. The annual mean levels of PM 2.5 pollutants, which are considered by the World Health Organisation to be the most dangerous kind (World Health Organisation 2021), were 9.6 $\mu g/m^3$ (Southampton City Council 2021). This is very close to double the World Health Organisation's recommended limit for average annual exposure, which is $5 \mu g/m^3$ (World Health Organisation 2021). This high level of pollution is in part because of the large port in the city and the industrial facilities associated with this. Other than the higher level of air pollution, Southampton is representative of many mid-sized coastal cities in the UK such as Liverpool and Bristol. Therefore, findings from this project may be useful in developing insights into other similar cities.

1.2 Research Problem

Investigating pollutant dispersion in a flow requires detailed information about the movement of the flow and air pollutants. In this thesis, the novel method that is Planar Laser Induced Fluorescence (PLIF) has been used. When paired with Particle Image Velocimetry (PIV) to study the turbulence in the flow, this is a very useful tool to study the relationship between turbulence and scalar dispersion. However, the PLIF methodology has innate uncertainties that must be quantified or reduced to an acceptable level in order to use it with as much confidence as PIV.

Due to the necessity of using simultaneous PIV and PLIF to acquire fields of turbulence and scalar concentration in the same place, and the difficulty of carrying out both of these techniques, there is very little of this data that currently exists. The influence of the flow structures that form around simple bluff bodies on the scalar field are, consequentially, poorly understood. There is also no existing dataset in which simultaneous PIV-PLIF is used to measure the dispersion of pollutants across a realistic city model, within an atmospheric boundary layer. In this dissertation, using these techniques over an urban test case was possible. This was due to the water tunnel facility that was used having sufficient length to develop an atmospheric boundary layer. Coupled PIV-PLIF data of fluid flow over a city is a valuable tool and can be used for various applications, from development of dispersion models to validation of meteorological models for weather simulation. This project aimed to generate and analyse this coupled data for the city of Southampton.

The specific objectives of this PhD research were set out as:

- 1. Objective 1 was to develop and validate the PLIF methodology for passive scalar measurements in the water tunnel. Specifically, to assess and improve the validity and accuracy of the process of translating the measured fluorescence intensity to concentration. An additional objective was to assess the suitability of the new consumer LaVision software package compared to custom MATLAB analyses. This goal was intended to result in the development of a methodology allowing for the PLIF technique to be carried out accurately.
- 2. Objective 2 was to utilise coupled PIV/PLIF to explore the fundamental features of air pollution transport in urban boundary layer flows. This was used as a baseline to compare to previous studies into idealised geometries, with the goal of providing new insights while also being a reasonable starting point for carrying out PIV/PLIF experiments.
- 3. Objective 3 was to build a model of the city of Southampton, and obtain high-fidelity measurements of air pollution distribution and transport for comparison with sensor data and ongoing Computational Fluid Dynamics (CFD) model development by collaborators. The completion of this goal requires the acquisition of a simultaneous PIV-PLIF dataset over a realistic city model.

This thesis will detail the progress that was made in these areas. The studies towards these objectives align with both current United Nations strategy (United Nations 2015), and UK government strategy (UK Government 2023). Both organisations have set goals for air quality reduction that are currently not being met across the entire UK (Owusu-Mfum et al. 2023). Therefore, it is hoped that by directly measuring key processes, deficiencies in current methods will be addressed, and that the studies in this thesis will be of value towards the goals set by these organisations.

1.3 Organisation of Thesis

Chapter 2 gives a brief review of relevant literature. Focusing on atmospheric flows and methods of experimentally modelling urban landscapes.

Chapter 3 begins to explain the methodology that was used in this thesis, specifically with regard to the facilities and particle image velocimetry. It also introduces the planar laser induced fluorescence technique and shows some preliminary work that was done to evaluate its accuracy. This chapter finishes with an overview of the experiments carried out in this thesis.

Chapter 4 delves deeper into the planar laser induced fluorescence technique. In section 4.1, the code package developed during this thesis is introduced, alongside the improvements to the PLIF methodology. In section 4.2, the accuracy of the PLIF technique with these improvements is demonstrated using a jet-flow validation case. It is in this chapter that objective 1 is completed.

Chapter 5 contains the content of a paper that was written based on a study into dispersion around an individual tall building. In this paper, the dispersion of a plume was measured around this building using simultaneous PIV and PLIF. This paper has been published in the journal Boundary Layer Meteorology and satisfies objective 2.

Chapter 6 contains the results of a case study into a realistic city model. For this experiment, a scalar plume was released upstream of the city model so that simultaneous PIV and PLIF could be used to measure the behaviour of the plume and its interaction with the city model. This case study builds on the work in previous chapters, on developing measurement techniques and applying them to a simplified case. In this chapter, objective 3 is completed.

Chapter 7 concludes this thesis, giving an overview of the work carried out. A summary of the conferences attended and some of the future work in this field that is required is also discussed.

Chapter 2

Literature Review

2.1 Urban Flow

2.1.1 The Thermally Neutral Atmospheric Boundary Layer

The atmospheric boundary layer (ABL) refers to the boundary layer that forms over the planet's surface due to the motion of air. The profile of the ABL is complex and varies in part based on the landscape below. It is estimated that the atmospheric boundary layer typically has a depth of between 1 and 10 kilometres (Garratt 1994). An example of this is shown in figure 2.1. There are various ways in which the boundary layer is defined, but the consensus is that it is the area of the atmosphere directly affected by the surface of the Earth. For warmer areas like deserts, this is towards the top of the range of boundary layer depths, sometimes in excess of 10 kilometres, whereas for ocean surfaces it is approximately 1 kilometre (Garratt 1994).

Due to the influence of tall buildings, there can be a significantly increased level of turbulence in urban environments, relative to rural ones. This increase in turbulence is of particular relevance, as in the urban environment, it can directly impact the comfort of people living in the city. This turbulence can also affect the levels of turbulent mixing at the pedestrian level (Talluru et al. 2018). The effects of a change in turbulent mixing can be an increase in air flow between indoor and outdoor environments, and also different levels of pollutant dispersion. The increased roughness of an urban environment causes a thicker boundary layer to form than might be found at other places in the atmosphere (Barlow 2014).

Atmospheric flows can also be characterised as, thermally; unstable, stable, or neutral, depending on if a temperature gradient between the surface of the landscape and the air is causing a buoyant effect (Fernando 2010). Making the assumption of a neutral atmosphere above a landscape removes the complexity of any turbulence or thermal plume caused by buoyancy. Unstable atmospheric flows have an increased level of pollutant dispersion and aid in preventing stagnant flow and an accumulation of

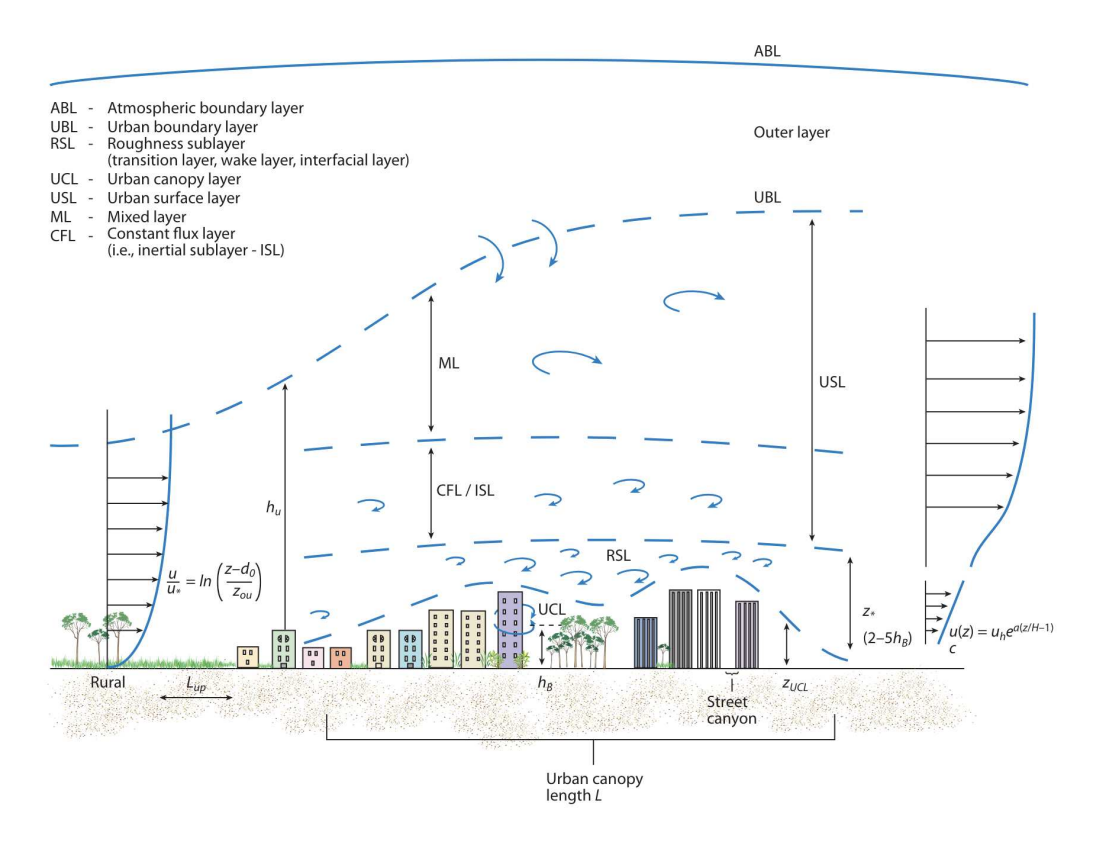


FIGURE 2.1: A diagram depicting the atmospheric boundary layer over an urban area. This figure depicts the thickening of the ABL over a city and the different flow regimes within (Fernando 2010).

pollution at the street level, when compared with neutral flows (Samad et al. 2023). Due to the difficulty in the experimental modelling of buoyancy, work carried out in this thesis will assume a neutral atmospheric boundary layer, and disregard buoyancy effects.

The boundary layer depth is defined as the distance from a surface at which the flow velocity becomes equal to 99% of the freestream velocity. This definition can sometimes fall apart in the case of the atmospheric boundary layer due to the fact that there is no freestream at which the flow velocity stabilises, and it continues to vary into the upper atmosphere. The idea of the standard atmosphere has been in use for over a hundred years (Gregg 1923), and only refers to the static properties of a flow, for example the temperature and pressure of the air (Georgantopoulou and Georgantopoulos 2018). When considering the atmospheric boundary layer this becomes even less predictable, as there is now a non-uniform motion to the atmosphere, in conjunction with its non-uniform static properties.

Accurate atmospheric modelling is a requirement for meteorological models, and the complexity of both the ABL and the variation in the standard atmosphere make this difficult (Best 2005). There are currently attempts to take specific urban geometry into account when calculating friction drag with the planet's surface (Sützl et al. 2021), however these are limited by the available computing power for simulations. It is clear,

2.1. Urban Flow 7

however, that the standard atmospheric boundary layer is highly complex, and this complexity is amplified by its interaction with an urban environment.

2.1.2 Defining Urban Length-scales

Urban environments and atmospheric flows in general, can be characterised through a variety of length scales. Urban features such as buildings are described on the building or obstacle scale, this being between 10^0 and 10^1 metres (Barlow 2014). For studies concerned with this characteristic length-scale, the individual wakes and recirculation zones in a flow must be well defined and well resolved. Next, there is the street scale, at roughly 10^2 metres. At this scale, buildings begin to act more uniformly on a flow, and the effect of larger features, such as street canyons, can play a significant role on the urban flow. Beyond this there is the neighborhood scale, at around 10^3 metres. At this scale the city is a more uniform structure. This makes modelling physical characteristics a more valid assumption. Above this, there is the city scale at 10^4 metres and the countryside scale past this.

When neglecting buoyancy effects by assuming a neutral atmospheric boundary layer, the only dimensionless number that must be matched to model an urban flow is the Reynolds number; which is defined as:

$$Re = \frac{\rho u L}{u}. (2.1)$$

In this equation, ρ is the density, u is the velocity, L is the lengthscale, and μ is the dynamic viscosity. When defining the Reynolds number for an urban flow, there are a multitude of ways to choose the length scale that is appropriate. The urban length-scales described above can be used; however, it is also reasonable to use the boundary layer depth of the atmosphere, or the average characteristic building height. Building height can also be defined in a more aerodynamic sense, as the vertical offset to the mean drag force (d). This is a useful aerodynamic parameter as it represents the offset at which a smooth wall with uniform friction would be located, to create a boundary layer with the same shape as that observed over the rough wall of the urban environment. It can be considered as the aerodynamic height of the city, and in environments with a large blockage ratio to the flow (Grimmond and Oke 1999), this offset can become quite large.

2.1.3 Turbulent Characteristics: The Roughness Sublayer and the Log-Law Region

The roughness sublayer is defined as the region of a boundary layer in which the flow is highly inhomogeneous and affected by individual obstacles. This is shown in figure 2.1 within an urban boundary layer. It is not purely a term used in atmospheric flows, but when applied to atmospheric boundary layers it frequently extends to 2-5 times the height of the tallest obstacles to the flow (H_{Bmax}) (Fernando 2010; Barlow 2014). Due to

the nature of highly urban environments and the increasing average height of buildings in cities, the roughness sublayers in urban environments can extend far into the atmospheric boundary layer, particularly in the vicinity of extremely tall buildings. This large inhomogeneous region increases the difficulty in predicting urban flows. This region is dominated by smaller turbulent vortices, and it has a much higher turbulence intensity than the freestream. The urban canopy layer shares characteristics with the roughness sublayer but is a term used to specify the region below the maximum building height. This is shown in figure 2.1.

The log layer of the atmospheric boundary layer extends from the roughness sublayer to roughly 100 m above the ground and is the section in which average wind speed observes a logarithmic rule with relation to its elevation above the planet's surface (Hoxey and Richards 1992). Within this region, the Reynolds stresses are also nearly constant. This region can be known as the inertial sublayer and extends further into the atmospheric boundary layer than the roughness sublayer does, as shown in figure 2.2. The region of the inertial sublayer which is not also within the roughness sublayer can still have its velocity dominated by turbulence components, however the flow begins to become spatially homogenous at this distance from the urban surface. Within this log layer, the mean flow velocity (*u*) varies according to

$$u = \frac{u_{\tau}}{\kappa} \ln \left(\frac{z - d}{z_0} \right), \tag{2.2}$$

where z refers to the height above the ground. In this equation, z_0 is the roughness length, which is the theoretical height at which velocity becomes zero according to the log law. The friction velocity u_{τ} is the velocity related to the wall shear stress, and κ is the Von Kármán constant. The variable d is the elevation of the mean body force, meaning it is effectively a variable used to account for the offset to the log law region, that can be caused by dense urban environments (Jackson 1981). Naturally, due to the highly turbulent nature of the log law region, this velocity profile is only an averaged value, and this average has to be taken in both space and time. This is because the time average can be very different in particular places in a city. For example, in the wake of a building there will be a localised lower wind velocity, that is present in the time averaged field.

Cheng and Castro (2002) defined the height of the roughness sublayer and inertial sublayer mathematically using point data from a hot wire anemometer. The upper limit of the roughness sublayer was defined as the height at which vertical profiles from different points above the wall morphology converge. The inertial sublayer is defined as the region in which the vertical variation of the spatially averaged shear stress is not above 5%.

It is problematic when attempting to model and predict urban turbulence, that the roughness sublayer can be extremely large where tall buildings are present, and simply using the log law is not valid within this roughness sublayer. Rather, within the roughness sublayer, fluid flow is defined by individual roughness elements, and so

2.1. Urban Flow

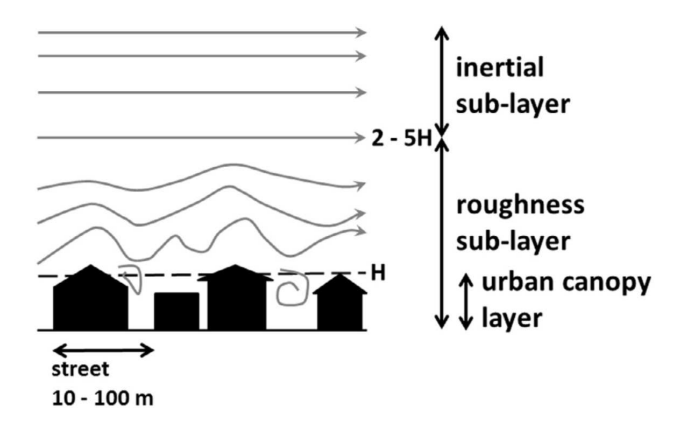


FIGURE 2.2: The roughness sublayer created by flow over an urban environment (Barlow 2014).

generalising rules are difficult to apply accurately. Outside this layer the flow becomes more predictable. In rural atmospheric flows, the roughness sublayer will depend on the height of local foliage, whereas in an urban environment, the roughness sublayer extends above the mean building height. Due to the fact that nearly all pollutant release happens within this sublayer, and all people living in a city live within this sublayer, it is necessary to model the chaotic flow within it accurately. This can allow us to know whether pollutant levels are being kept safe within particular areas of cities.

2.1.4 Homogeneous Surface Conditions and the Meteorological Approach

When attempting to characterise a physical urban surface geometry, there are many possible variables that can be examined. The characteristics of zero plane displacement and roughness length can be used to represent a building array's mean approximate shape. There are two approaches to assigning these characteristic lengths, the first being morphometric methods, and the second being micrometeorological methods. Morphometric methods use known geometries and arrays that have previously been experimentally tested and extrapolate values from these for new urban terrains. Micrometeorological methods practically measure the urban flow, naturally this approach is more certain, but taking real data of an urban flow is not an easy task. Grimmond and Oke (1999) studied uniform arrays of buildings and showed that it is possible that arrays with the same mean element height and element density have different measured roughness values if they have different roughness element height variances, proving the difficulty in characterising an array in a way that fully represents it.

Cowen et al. (2001) investigated how air temperature and turbulence vary with height in an urban environment. Their research is uncommon in that it directly uses measurements of the urban boundary layer. They found that some of the peculiarities in the measured data are caused by one or two nearby high-rise buildings. These buildings cause local inhomogeneity in the ABL. The directly measured data was compared with

large eddy simulation (LES) models and found to be reasonably consistent. However, as the direct data is only taken in one place, it is difficult to comment confidently on its accuracy as the turbulence in an urban environment can be highly inhomogeneous. The conclusions drawn from this paper showcase the difficulty in understanding urban flows well.

It is common within meteorological simulations to model surface topology in all but the most detailed simulations. This is because grid resolution is of the order of multiple kilometres in size, even for simulations by the Met Office (Bush et al. 2020). The Met Office's JULES land configuration models the surface turbulent flux through a function of the friction velocity and the convective velocity scale, and it is through simple variables such as these that the difference between an urban and rural atmospheric boundary layer is accounted for.

2.2 Turbulence Characteristics and Species Flux

2.2.1 Defining Species Transport

In order to model pollutant dispersion in an urban flow, the turbulent transport processes must be quantified. The flux J_i of a species, with concentration C, along direction x_i , is given by Fick's law of diffusion, with γ being the molecular diffusivity of the species,

$$J_i = -\gamma \frac{dC}{dx_i}. (2.3)$$

This equation, however, only defines species transport due to diffusion. When the fluid is in motion, species transport is defined instead by the advection-diffusion equation,

$$\frac{\partial C}{\partial t} + U_j \frac{\partial C}{\partial x_j} = \gamma \frac{\partial^2 C}{\partial x_j \partial x_j}.$$
 (2.4)

The advection-diffusion equation describes the transport of a passive scalar, and assumes the effects of buoyancy, body forces, or actively reacting substances are negligible. In this equation, the first term $(\frac{\partial C}{\partial t})$ represents the change in the species in the flow over time, the second term $(U_j \frac{\partial C}{\partial x_j})$ represents the change in species transport caused by the mean flow velocity. The third term $(\gamma \frac{\partial^2 C}{\partial x_j \partial x_j})$ is the change in the species due to molecular diffusivity.

For turbulent flows, it is possible to separate variables into mean and fluctuating components using Reynolds decomposition. For velocity, this looks like $U_i = \overline{U_i} + u_i'$, and for scalar species this looks like $C = \overline{C} + c'$. Applying this to equation 2.4 gives the Reynolds-averaged advection diffusion equation,

$$\frac{\partial \overline{C}}{\partial t} + \overline{U_j} \frac{\partial \overline{C}}{\partial x_j} = \frac{\partial}{\partial x_j} \left(\gamma \frac{\partial \overline{C}}{\partial x_j} - \overline{c' u_j'} \right). \tag{2.5}$$

This is the turbulent transport equation for passive scalars (Pope 2001). The $-\overline{c'u'_j}$ term is the turbulent scalar flux, and it is the cross product of the instantaneous velocity fluctuation and scalar fluctuation. This term is complex to fully resolve and, therefore, closure is most often achieved through the use of the first-order gradient transport model,

$$-\overline{c'u_i'} = D_{ij}\frac{\partial \overline{C}}{\partial x_i}. (2.6)$$

In this model, D_{ij} is the turbulent diffusivity tensor, with nine components, depending on the local turbulence. This first-order gradient transport model is based on the assumption that the macroscopic lengthscale of the flow is greater than the turbulent lengthscale, and that the flow characteristics are homogenous across the turbulent lengthscale.

The smallest scale at which scalar diffusion is dominated by turbulent diffusivity, as opposed to molecular diffusivity, is known as the Batchelor length scale (η_{β}). The Kolmogorov length scale (η) represents the smallest scale at which turbulent eddies can exist in a flow without being suppressed by the viscosity of the fluid, and therefore the smallest turbulence length present overall. The ratio between Kolomogorov lengthscale and Batchelor lengthscale is different for every substance, and is proportional to the square root of the Schmidt number $Sc \equiv v/\gamma$. For nearly all substances this is a number greater than 1.

2.2.2 Existing Approaches to Modelling Species Transport

The ways in which species transport is modelled differ based on both the case being simulated, and the type of simulation (Barlow 2014). Current best practice for simplified modelling is to assume a constant, uniform, species-flux within the log-law region of a boundary layer.

The effect that urban features have on local fluid flow and dispersion was collated by Britter and Hanna (2003). An initial observation was that an increase in ground-level turbulence correlates with an increase in plume growth rate, and therefore with an increase in scalar dispersion. This is the most simple form of the relationship between increased turbulence and increased dispersion. The flow within urban canopies and streets follows certain rules. For example, it is suggested in the review by Britter and Hanna (2003) that for some flow structures within an urban canopy it can be assumed that the mean flow velocity will be 1/2 to 1/3 of the value it is at the rooftop level. It is also suggested that the turbulence level within the canopy is in the region of 10%. These

guidelines can give numbers that can be applied to models, such as those used in Reynolds-averaged Navier-Stokes (RANS) simulations.

The gradient diffusion hypothesis is most often used within RANS simulations because all scales of the turbulent and molecular scalar flux terms must be modelled (Tominaga and Stathopoulos 2012), and it is a relatively simple model to apply. This hypothesis makes the assumption that turbulent motions, such as eddies, increase mixing. It is also assumed that the direction of transport caused by this is always down concentration gradients (da Silva and Pereira 2007). The simplest way to functionally use the gradient diffusion hypothesis is with the eddy diffusivity model. In this case the turbulent scalar transport is modelled in the form shown in 2.6, in which D_t is the eddy diffusivity. This in turn is modelled as

$$D_{ij} = \frac{\nu_t}{Sc_t},\tag{2.7}$$

which is a relationship between the eddy viscosity (ν_t), and the turbulent Schmidt number (Sc_t). It is the standard within wall bounded flows to use a value of (Sc = 0.9) (Rossi 2010). In addition, it was recently shown by Lim and Vanderwel (2023) that the turbulent Schmidt number (Sc_t) can accurately be assumed to be 1, which makes the eddy diffusivity model particularly easy to apply.

The gradient diffusion hypothesis can be applied qualitatively to a case of a ground-source plume within a flow over a rough environment. When applied to a case like this, the implication of this model is that turbulent fluxes will always transport a scalar in the upwards vertical direction, as the highest concentration will generally be found close to the ground.

This thesis aims to enable study into the accuracy of the available modelling methods through direct measurement of the terms they would normally be used to model. There is currently only a very small amount of literature that has directly measured the dispersive flux terms, and none that have done it in full fields within a realistic boundary layer.

2.2.3 Gaussian Plumes

The solution for the advection-diffusion equation for a continuous point source is known as the Gaussian plume equation. This equation is given as;

$$C = \frac{Q}{u} \frac{f}{\sigma_y \sqrt{2\pi}} \frac{g_1 + g_2}{\sigma_z \sqrt{2\pi}},\tag{2.8}$$

in which C is the local concentration, Q is the source emission rate, u is the mean wind velocity, f is the crosswind dispersion parameter, σ_y is the horizontal standard deviation of the emission distribution, and σ_z is the vertical standard deviation of the emission distribution (Cambridge Environmental Research Consultants 2023). In this equation, g_1 and g_2 are the components of the vertical dispersion parameter. The vertical dispersion

parameter is an exponential function that varies based on the source interaction with the ground. For a release with no ground reflection it takes the form

$$g_1 = exp\left[-(z-H)^2/(2\sigma_z^2)\right],$$
 (2.9)

in which H is the source height above the ground. With ground reflection the additional g_2 term is added, which is otherwise assumed to be zero:

$$g_2 = exp \left[-(z+H)^2/(2\sigma_z^2) \right].$$
 (2.10)

The crosswind dispersion parameter only has one form and appears as:

$$f = exp \left[-y^2/(2\sigma_y^2) \right]. \tag{2.11}$$

In mostly homogenous rough terrain, it is accurate to assume that the concentration (C) in a pollutant plume forms a Gaussian profile (Carpentieri et al. 2004; Marucci and Carpentieri 2020) according to equation 2.8. In unbounded flows, the widths, σ_y and σ_z , are expected to grow according to an $x^{0.5}$ function, however variation has been shown in atmospheric flows (Hertwig et al. 2018). It is still not well known how the characteristics of a Gaussian pollutant plume are affected by rough urban terrain.

2.3 Idealised Roughness

2.3.1 Single Cube Approximations

The study of urban models is all built upon previous studies into bluff bodies, and the most fundamental possible example of this is a wall-attached cube, as carried out by Castro and Robins (1977) and Martinuzzi and Tropea (1993). Martinuzzi and Tropea (1993) studied the flow structures around these cubes and there are certain flow structures that are common between them and other bluff body flows. In the image by Martinuzzi and Tropea (1993), shown in figure 2.3, the horseshoe vortex that forms below the stagnation point ahead of a cube is visible very prominently, accompanied by another large attached vortex in the wake of the cube. The small vortices visible in the diagram on the top and side of the cube are also common to most cubes, and represent flow separation. Because flow separation is fixed at these sharp edges the flow does not change much with Reynolds number and can be considered Reynolds number independent above a certain value (Lim et al. 2007). However, Castro and Robins (1977) proved that the reattachment of flow behind these vortices, but before the trailing edges, does not always occur. The reattachment area depends on the turbulence intensity of the flow, and the ratio of boundary layer depth to cube height.

The cubes studied by Castro and Robins (1977) are shown to have limited Reynolds number effects, with Reynolds number being calculated based on the cube height.

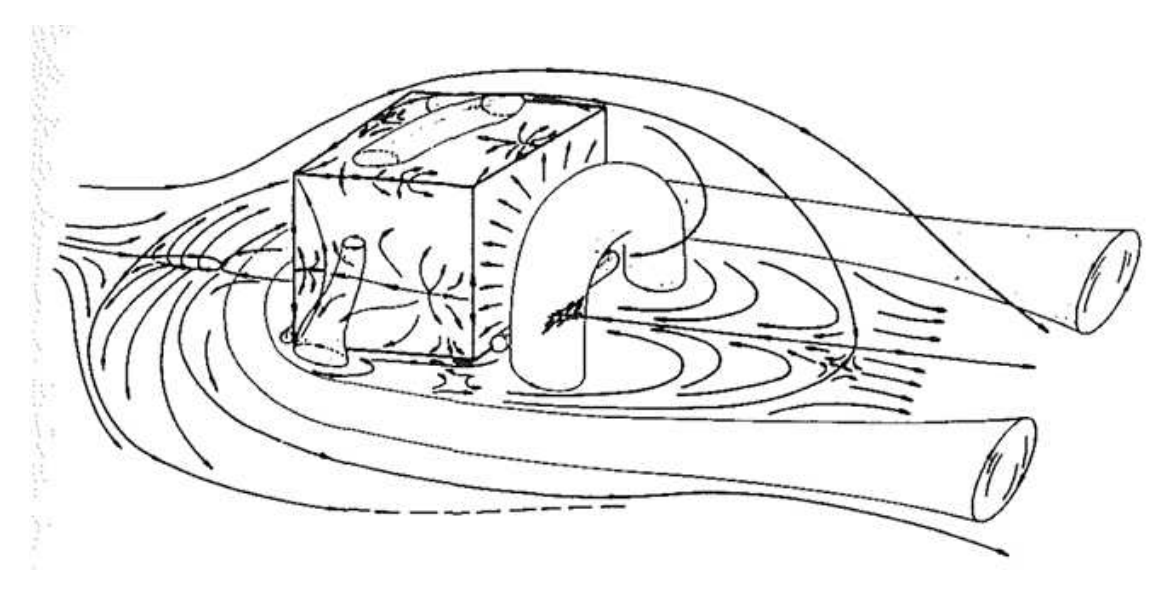


FIGURE 2.3: Martinuzzi and Tropea (1993) The flow structures typical to a wall-attached cube perpendicular to a fluid flow.

Specifically the shear layer in the flow passing above the top of the cube moved upwards as Reynolds number increased, until the Reynolds number reached 30,000. The other effect measured is that, with a cube at a 45 degree angle to the flow, the pressure gradient above the leading edge increased in magnitude as Reynolds number increased.

Recirculation bubbles are a well studied fluid phenomenon in bluff body flows, and are known to decrease the predictability of dispersion by introducing strong, non flow aligned velocity components. The effect is much more pronounced in flow over a bluff body perpendicular to an incoming flow. In the immediate wake of these bluff bodies it is possible to detect reversed flow, instead of just a velocity deficit, the extent of the time-averaged reversed flow can be used to define the size of the recirculation bubble. Reversed flow is not observed at all in the case for the bluff body at 45 degrees to the incoming flow, but can be measured in the case of the bluff body perpendicular to the flow (Castro and Robins 1977). This recirculation region had the highest reversed velocity very close to the tunnel floor, in the near wake of the cube. This region only extended slightly more than a single cube height downstream, and therefore only took up a small portion of the velocity deficit region. The velocity deficit measured in the wake of a single cube was measured by Castro and Robins (1977) to be entirely gone by 8.5 cube lengths downstream of the cube, and by this point the flow velocity was within experimental error of free stream values. This is a useful value to know, because it gives an idea of the distance at which a bluff body can have an impact on a flow field.

2.3.2 Defining an Array

When studying urban environments, it can be helpful to reduce the randomness of city topology in order to obtain less case-specific results. Idealised roughness arrays are a type of model used to help study cities and other rough surfaces by reducing or removing random variations in the roughness elements. The most commonly used and

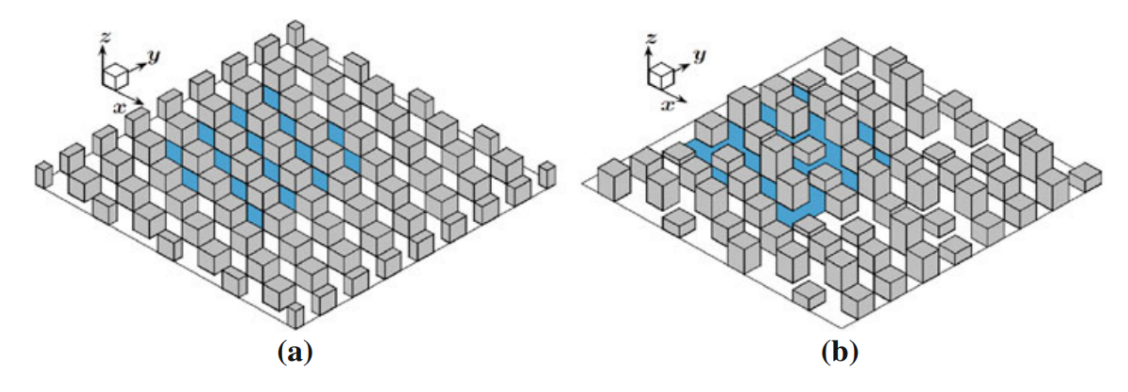


FIGURE 2.4: Regular staggered arrays, with (b) and without (a) height variation (Boppana et al. 2010).

simplest layout is a grid with no offset to rows or columns (Boppana et al. 2010; Goulart et al. 2016), with cubic elements at each nexus, and an element spacing equal to the cube dimensions. While this array is of an overwhelmingly simple design, it is still a non-trivial task to fully define it in terms of physical parameters, as a geometry that is influencing a fluid flow.

Xie et al. (2008) used a pair of staggered arrays, meaning arrays in which elements in the flow direction are not in line, and then differentiates the two of them purely based on element packing density, having values of 6.25% and 25% density. Cheng and Castro (2002) showed however, that these staggered arrays have significantly stronger effects on the flow than aligned arrays, in which roughness elements line up with each other. An example of regular staggered arrays is shown in figure 2.4. These arrays examined by Cheng and Castro (2002) are identical, but are rotated with respect to the flow direction by 90 degrees. This study showed drag increasing by up to 78% at the height of the top of the cube, for the lowest speed tested, however inertial sublayer and roughness sublayer depth did not vary significantly. Measured roughness length approximately doubled, and an increase is expected due to the increased measured drag, but the size of the increase shows just how little effect the elements shielded in the wake of other elements have on the flow. Clearly then flow over an array is extremely sensitive to array geometry, if a simple rotation with all other variables constant can create such a strong effect.

The difference in the two arrays described above can be explained best using the effect known as shielding, in which an array element exists in the wake of a different element. This reduces the total drag effect they have on the flow compared to if they both existed in the flow independently. Aligned arrays have extremely high shielding effects, whereas relatively speaking, staggered arrays have much lower shielding effects, despite having the same frontal planform density (Grimmond and Oke 1999). Vanderwel and Ganapathisubramani (2019) investigated the effect of shielding by using arrays with the same number of elements, but differing frontal solidity, (λ_F). Shielding is a difficult effect to directly quantify, however Vanderwel's method to keep planform density (λ_P) constant, while varying frontal solidity, gives a variable that can be quantified, for the specific wind direction and array being tested. Placidi and

Ganapathisubramani (2015) also investigated the relationship between frontal solidity (λ_F) and drag. In this paper, it was also shown that increasing λ_F caused an increase in drag for a rough surface, but only up to a peak value of $\lambda_F = 0.21$ (at $\lambda_P = 0.27$). It was also shown that increasing λ_P with a constant λ_F reduced the drag of a surface, for the constant value $\lambda_F = 0.15$. These findings indicate the sensitivity of roughness to a skimming flow regime, and show the complexity in predicting the influence roughness will have on a flow.

The effect of height variation in regular arrays is explored by Cheng and Castro (2002), where random height variation is added to a staggered array, with a staggered array of uniform height for comparison. Both arrays use elements of 10 mm per side, with the uniform height array also having 10 mm as the height, to make a standard staggered cube array. The random height array, uses a mean element height of 10 mm to retain comparability to the uniform array. In this paper, it is noted that nearly every physical array parameter is still constant. For example, the element spacing and location, the element shape, and the element length and width, are left the same as the uniform array. A repeating unit was then generated with heights varying between 2.8 mm-17.2 mm. This repeating unit was 80 mm square, with a total of 16 elements, and these repeating units were attached in an 11 by 11 grid. The conclusion of the study was that the random height array has an approximately similar inertial sublayer upper limit, but within that the roughness sublayer is much larger than for the uniform array.

2.3.3 Street Canyons

One of the most consistent characteristics found in both idealised arrays and realistic urban environments are street canyons. Street canyon refers to channels in an urban landscape or regular array. These are physical characteristics but their influence on a flow is dependent on flow direction. In the aligned arrays discussed above, it is possible to find regions of reversed flow trapped in-between the aligned elements, these regions have highly complex aerodynamics as they exist in-between linear street canyons, which are aligned with the flow on each side. Tominaga and Stathopoulos (2011) uses flow visualisation and Computational Fluid Dynamics (CFD) to investigate scalar flux over a uniform, aligned array of rectangular elements. They showed that flow in between elements in an aligned array is dominated by the recirculation effect, with only a thin shearing layer between that and the uninterrupted flow through the canyon in the streamwise direction. The velocity components in both the centre of the recirculation bubble and the streamwise canyon have only very small crosstream components, with large streamwise or vertical components.

A lack of crosstream velocity is consistent with the observed lack of crosstream motion of a scalar tracer noticed by Tominaga and Stathopoulos (2011). The scalar transport phenomena observed in their paper was that the scalar would either flow down the streamwise canyons in large vortices forming off the street boundary layer, or the scalar would become trapped in recirculating vortices between the elements.

The paper by Soulhac et al. (2008) modelled the flow in street canyons at varying angles, relative to the oncoming flow. In the model developed in this paper, at most angles, the streamlines in a street canyon would form a spiral shape down the canyon. With the mass flux down the street being a function of the magnitude of the free-stream wind velocity parallel to the street direction. This model was validated using detailed numerical simulations and found to be accurate. This paper shows that street canyons can channel a flow, and that once a streamline is inside one it is unlikely for it to spontaneously escape.

Some work has also been done studying street canyons within more realistic urban models. It was shown in the experimental work by European Cooperation in Science and Technology (2015) that it is possible for street canyons to channel higher levels of scalar concentrations than in the surrounding flow. However, when computationally simulating the same case, it proved difficult to replicate this result. It was observed that when a scalar was released in a relatively open area, then Large Eddy Simulations (LES) or simplified models performed accurately in matching experimental results. However, when a scalar was released within a street canyon (flow aligned or not), the computational results did not match the experimental results as accurately.

2.3.4 Scalar Source type and sensitivity

It has been reported in various papers that when a scalar is released from a ground source in an ordered cube array, that source location has a significant effect on scalar dispersion (Tominaga and Stathopoulos 2011; Fuka et al. 2018). This makes sense intuitively knowing how little cross stream transport there is in flow over an aligned array. Vertical transport outside the roughness sublayer is limited, and due to this the geometry stays relevant to the scalar dispersion far downstream, making the distance at which a Gaussian distribution can be assumed, very large. Boppana et al. (2010) avoids this problem entirely through using a distributed source, which is a fascinating technique as it most accurately mirrors many of the pollutant sources encountered in the real world, for example cars and building ventilation. Boppana et al. (2010) found that a Gaussian distribution was a reasonable approximation for the shape of the plume from the distributed source.

Fuka et al. (2018) measures the effect of adding a single tall building to a uniform array, both experimentally and computationally. This paper takes combined velocity-concentration measurements, allowing both the advective and turbulent scalar fluxes to be examined. The array with no tall building showed mostly negative vertical advective fluxes, at low heights, but large, positive vertical turbulent fluxes, that resulted in overall vertical species transport. Adding the tall building to this array reduces the total, vertical, turbulent and advective species flux in its immediate vicinity, but increases horizontal transport. The flow field shows that this is in part because scalar in front of the tall building, at a low height, gets caught in a strong down wash and horseshoe vortex pattern. Figure 2.5 shows the turbulent diffusivity of the vertical

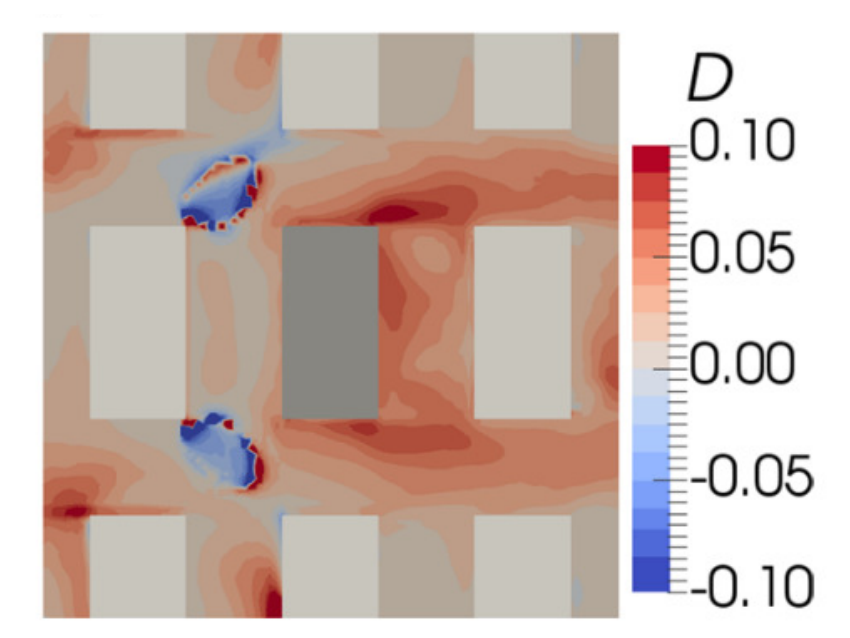


FIGURE 2.5: Vertical turbulent diffusivity around a tall building in a regular array, with turbulent diffusivity (*D*) calculated as $\overline{c'w'\frac{h^2}{Q}}$ (Fuka et al. 2018). In which *Q* is the mass flow rate at the source, *h* is the building height, *c'* is the fluctuating concentration, and w' is the fluctuating vertical velocity component.

component of species flux, this graph has very interesting strongly negative regions at the forward facing corners of the tall building. Measuring this component experimentally and comparing it to this LES result would be extremely interesting. This result is however, with the caveat that this species release was from the ground directly in the down wash of the tall building. A different case with the species release in the street canyon slightly ahead of the tall building and to the side, showed a more similar flow pattern to the uniform array case, aside from an asymmetric deflection away from the wake of the tall building. It was again observed that the species was being trapped in the horseshoe vortex emanating from the tall building.

Scalar release into the wake of the tall building caused the species to become trapped in the near wake of the building, within the recirculation region. This release point showed the least horizontal transport; and by far the most vertical transport, it appears that species entering this taller recirculation zone is strongly vertically transported. However, most species impacting the front of the building is transported horizontally away from this zone, so it mostly stays relatively clear of the species. Heist et al. (2009) shows that in the case that the scalar is released at ground level directly into the recirculation bubble, vertical transport of the scalar is significantly higher than elsewhere in the uniform array.

Fackrell and Robins (1982a) explores the effect of an elevated dye point source compared to a ground level dye release, the findings show that the elevated dye source has a mostly Gaussian profile downstream in the flow. Having the point source within the street canyons, however, makes the dye dispersion in the flow much harder to

predict. The profile of dye downstream from the ground level source can be highly asymmetric, depending in large part on the specific street geometry around the source.

2.3.5 A Note on Urban Comparison

The purpose of these bluff body arrays mentioned previously is to approximate an urban geometry through a reduced order. The study of bluff body arrays themselves has proceeded to a reasonable extent over the past two decades. However, there is a very notable gap in this literature in comparing these arrays to real urban geometries. Some progress was made through adding randomness to certain aspects of the generation of the arrays (Vanderwel and Ganapathisubramani 2019; Cheng and Castro 2002). These studies still, however, struggle to create arrays representative of any urban landscape. There are certain large scale characteristics which have a measured effect on the flow, for example street canyons, that are not recreated in fully random models (Vanderwel and Ganapathisubramani 2019). This shows that pure randomness is not an accurate way to represent urban geometry. Generating artificial urban geometry at will is a difficult task, despite it being done in a relatively consistent way in most cities throughout the world.

2.4 Investigations into Realistic Urban Environments

2.4.1 Velocity Measurements in Real Cities

The airflow around realistic city models has been measured in many cases in the past, however, fully characterising the flow through a city is challenging to do in this way. This is because many studies use point measurements within the urban canopy, and due to the spatial inhomogeneity in this region most conclusions drawn from this data are only locally accurate. In the case studied by Sousa et al. (2018) a method of accurately predicting boundary conditions for a CFD domain, using point measurements of a real case is developed. This is done using synthetic point measurements generated from a RANS model, however it demonstrates the value of real-world, point measurements.

The study by Hertwig et al. (2019) studied the differences between simplified and realistic experimental models, and was able to provide insight into the effects of a realistic urban array surrounding a tall building. It was found that the presence of buildings in the wake of the tall buildings displaced the recirculation zone upwards, and therefore caused an increase in turbulence at the level of the tall building rooftop. Further in the wake it was found that turbulent kinetic energy was being reduced by the presence of smaller buildings. This was caused by the urban canopy distributing energy down to the smaller scales of motion more rapidly.

There are some studies into airflow across cities that use Doppler Lidar anemometers (Liu et al. 2022; Lim et al. 2016). This is a measurement technique that allows for the

acquisition of data along a vector, with a maximum range dictated by the quality of the measurement equipment and environmental factors. Lim et al. (2016) uses a Doppler Lidar anemometer to measure airflow in the vicinity of a tall building, with the purpose of validating against wind tunnel tests. In this case, it was found that this technique measured similar mean velocity values, as were predicted by the scaled wind tunnel tests, but that the turbulence values measured were lower than expected. Nevertheless, this technique shows its value in enabling the collection of larger datasets than are possible with point measurements.

2.4.2 Concentration Measurements in Real Cities

Scalar concentration measurements in real cities are uncommon, in part due to the ethical concerns of releasing scalar tracers in populated areas. Some of the existing studies have either managed to release safe tracers in a limited capacity (Martin et al. 2010); or measured the unintentional release of unsafe pollutants, caused by accidents such as fires (Clements et al. 2024). The paper by Samad et al. (2023) uses a wide variety of real-world measurement techniques to examine the airflow and pollutants around Stuttgart. The large dataset collected in this paper gives insight into the relationship between boundary-layer depth and ground level pollutant concentrations. This was possible through the use of vertically aligned Doppler Lidar measurements, and showed that a shallow boundary layer caused a higher level of pollutants at ground level.

In multiple cases, measurements have been made of pollutant levels at individual points within urban environments (Matthews et al. 2024; Cowell et al. 2024). These can provide insight into the dispersion of these pollutants within limited cases; however, without a large dataset, such as in the case investigated by Samad et al. (2023), it is very difficult to draw generally useful conclusions. The study by Matthews et al. (2024) did, however, draw attention to the fact that pollutants released over a short time frame were retained at street level for multiple days after the release event. While, the investigation by Cowell et al. (2024) was focused on proving the accuracy of the sensors that were developed.

2.4.3 Dispersive Flux Measurements over Realistic Scaled Models

There are relatively few datasets in which dispersive fluxes are measured over realistic scaled models, however those that do exist offer insight into the movement of pollutants in real cities. In the work by Ono and Nozu (2024), dispersion through a large wind tunnel model is examined using hot wire anemometry and fast flame ionisation. The point data from these measurements is used to validate an LES simulation. It was found that across the 241 concentration measurement points, the fraction of predictions within a factor of two of the experimental measurements (FAC2) remained above 0.6 at all points. It was concluded that this demonstrates a good level of agreement. This was because it had previously been suggested by Britter and Hanna (2003), that a FAC2

above 0.3 was an appropriate level of accuracy for urban applications. The data from these experiments by Ono and Nozu (2024) show that the scalar plume was highly intermittent in both the experimental and LES cases, and that this intermittency is particularly high near the source. It is also shown that consistently worse agreement in concentration distributions, between experimental and computational results, is found at a height of 25m (the lowest measured), than at 85m. This demonstrates the challenge and uncertainty involved in simulating scalar dispersion over urban models, either experimentally or computationally, and particularly within the urban canopy.

2.5 Experimental Approaches

2.5.1 Why Experiments are Necessary

Experiments are necessary within the field of wind engineering due to the uncertainty introduced into computational simulations when using a coarse mesh or modelling parameters such as the turbulent flux. Collecting field data is valuable for the verification of simulations, but large datasets can be acquired more easily and repeatably using experimental models. Using experimental models also allows the use of a wider variety of experimental methods, such as optical techniques.

The vast majority of aerodynamic research is carried out on mechanical subjects such as wings, or cars. The length scales involved in these subjects typically vary from centimetres to metres. As such, these subjects can be easily scaled for experimental testing in a wind tunnel, due to them having a size of the same order of magnitude as the test section in most scientific wind tunnels. Generally these subjects are also of a size which is simple enough to mesh for computational simulations, whether this is using Reynolds Averaged Navier Stokes (RANS), or Large Eddy Simulation(LES).

This is in contrast to urban and meteorological studies in which simulation domains can be hundreds or thousands of kilometres in size. Due to time constraints, this means grid resolutions have to be of the scale of kilometres. For the Met Office, the smallest grid resolution used is 1.5km, and the largest is 20km, which is used for global numerical weather predictions (Met Office 2024). These grid sizes leave a significant amount of flow information in the sub-grid scale. In order to find out information about these sub-grid processes either laboratory experiments or real world data acquisition must be carried out.

2.5.2 The Approximation of Atmospheric Boundary Layers in Laboratories

Flow conditioning methods are often used in wind and water tunnels, however typically they are employed to reduce the turbulence intensity of a flow as low as possible. In the paper by Tomas et al. (2017), roughness elements are used as a form of

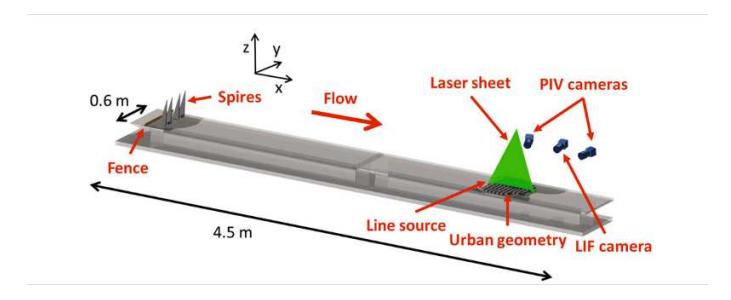


FIGURE 2.6: The experimental setup used to approximate an atmospheric boundary layer by Tomas et al. (2017).

flow conditioning. They are used to increase the turbulence intensity and also condition the incoming flow to match the velocity profile shape of the atmospheric boundary layer. Tomas et al. (2017) used the setup shown in figure 2.6 to examine dispersion over an idealised city model.

The atmospheric boundary layer has a known variance of turbulence against height, and a known velocity scale in the log law region. It is most important that the log law region matches the features of the atmospheric boundary layer, when simulating urban flow, this is because all current urban landscapes exist entirely within the log law region (Tomas et al. 2017).

There are several wind tunnels dedicated primarily to the study of urban flows such as the University of Surrey's Environmental Flow Laboratory wind tunnel, and the University of Eindhoven's Atmospheric Boundary Layer wind tunnel. These wind tunnels aim to reduce the uncertainty of experimental measurements through accurate ABL conditioning. In the case of the Environmental Flow Laboratory wind tunnel the incoming ABL can also be heated to enable the studying of thermal effects and to more accurately recreate a real ABL.

2.5.3 Water Tunnel Experiments

The main advantage of water tunnels over wind tunnels, in experimentally modelling urban flows, is the ease of carrying out PIV measurements, and the possibility of using Planar Laser Induced Fluorescence techniques to track dispersion. However, the use of a more dense fluid to model urban airflow is also beneficial. For a flow to be dynamically similar to a different flow in terms of momentum, the Reynolds numbers of the two flows must also be similar, this looks like:

$$\frac{\rho_1 u_1 L_1}{\mu_1} = \frac{\rho_2 u_2 L_2}{\mu_2},\tag{2.12}$$

in which ρ is the density, u is the flow velocity, L is the length scale, and μ is the dynamic viscosity. Therefore, it can be seen that, with an increase in density (ρ_2), there can be a decrease in size (L_2). Because of this, modelling in water tunnel facilities can be advantageous as it allows for significant reduction in length scale due to the difference

in density between water and air. The increase in density of water, does however mean that typically water tunnel facilities are limited in flow velocity to an order of magnitude lower than that of wind tunnels. This means that the two facility types can both approximate high Reynolds number flows reasonably similarly.

In most dynamic scaling, the similarity relationship given in equation 2.12 has to be observed meticulously, this is because curved surfaces like aerofoils have to have the same separation point no matter how they are scaled, or the scaling will not be truly representative of the full model (Fackrell and Robins 1982b). A lot of city scaling can be more forgiving than this, as nearly all objects investigated are bluff bodies of some description. This means that the assumption of Reynolds independence of a cube that was mentioned in section 2.3.1 Lim et al. (2007), is also valid for the bluff bodies in a city. Therefore, with a Reynolds number above 5000-10000, based on building height, a turbulent flow over an urban landscape can be assumed to be Reynolds number independent (Plate 1999; EPA US 1981).

2.6 The Gap in the Literature

Existing studies into urban boundary layers are limited to either computational studies, which model the finer details of turbulence, or experimental studies, which have the ability to measure the fluctuating velocity components directly. When looking specifically at scalar dispersion and how turbulence impacts this, it becomes necessary to know both the velocity and scalar variation throughout the flow. This adds a level of complexity to creating experimental models, as it is an extremely difficult process to track species concentration of a tracer species in air. This has been carried out by Talluru et al. (2018) through the use of fast flame ionisation to obtain point measurements at different places in a flow. This process was, however, limited to providing point data. Most of the current experimental investigations into urban flows are aimed at evaluating general rules of the urban flow, as opposed to examining a specific section of city in detail (Tomas et al. 2017).

There is a gap in existing literature to measure full fields of dispersion and velocity simultaneously over a realistic city model, with a flow conditioned according to the atmospheric boundary layer. By extension, relationships need to be drawn between the data generated from realistic urban models to that existing for simplified urban models, such as wall mounted cubes and bluff body arrays. This gap exists primarily due to the high difficulty in conducting urban dispersion studies. The measurement of experimental urban dispersion data in water tunnels is done through the use of lasers and specialised cameras to track the release of neutrally buoyant dyes. This is a process requiring a significant amount of uncommon equipment. Even when studied in water tunnels or flumes, only those ones with a particularly long test section are able to condition the flow according to the atmospheric boundary layer. Therefore, there are relatively few research groups worldwide with access to the necessary equipment,

facilities, and expertise to produce the data to fill this gap. The majority of papers investigating urban boundary layers are conducted using either LES data or do not investigate scalar dispersion (Van Buren et al. 2017; Torres et al. 2021). It is a minority of studies that experimentally measure both scalar dispersion and velocity characteristics.

Chapter 3

Methodology

3.1 Details of the Flow Setup

3.1.1 The Water Tunnel Facility

All experiments were conducted in the University of Southampton's recirculating water tunnel at Boldrewood Innovation Campus, shown in figure 3.1. The water tunnel was constructed in 2020 by GUNT Technology Ltd. It has a test section that is 8100 mm long, and 1200 mm wide, with a maximum water depth of 900 mm. The facility can be run at a maximum velocity of 0.75 m/s. The test section has an open surface, and glass walls and floor, which allow for easy optical access.

Due to how recently this facility was constructed, time had to be allowed for commissioning the facility. This involved iterating on the flow conditioning used to reduce the turbulence intensity of the flow in the test section without any models

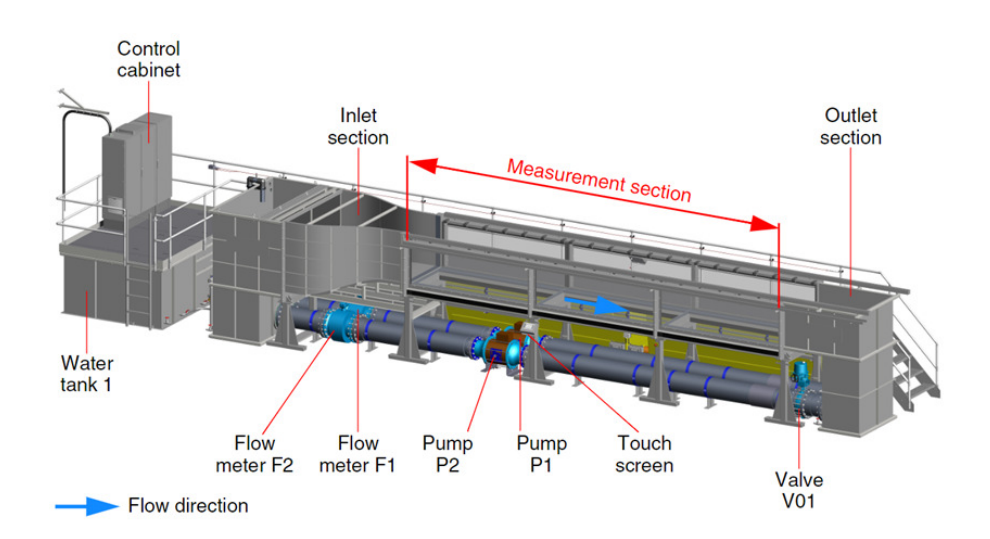


FIGURE 3.1: The Recirculating Water Tunnel at the University of Southampton's Boldrewood Innovation Campus.

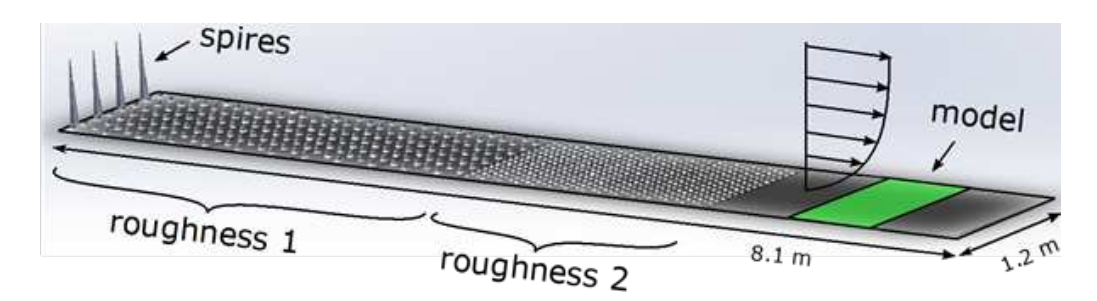


FIGURE 3.2: A plan view of the initial version of the roughness elements that were intended to create an atmospheric boundary layer.

installed, and on developing the roughness used to generate an atmospheric boundary layer.

3.1.2 Atmospheric Boundary Layer

A false floor was constructed out of plastic that lay on top of the glass bottom of the tunnel to allow models and roughness to be attached to the floor of the tunnel. The goal of the iteration on the atmospheric boundary layer false floor was to create a roughness false floor design that would allow scaled urban models to exist within the log law region of the boundary layer. This is so that experimentally simulated cases more realistically match those of real urban environments.

The roughness used in the false floors has three different element sizes, beginning at 30 mm cubes, then 15 mm, then 10 mm. The investigations into these ABL false floors found that the point that the final roughness stopped was creating an internal boundary layer. This was unintended and the next iteration of these false floors removed this by adding roughness to the previously smooth panel upstream of the test section. This brought the smallest size of roughness all the way up to the front of the test section. It was also found that the spires interacted unexpectedly with the free surface of the water tunnel and, with the increase length of small roughness, it was found that they were not necessary to create a sufficient boundary layer depth. Removing them finally created the intended ABL, with a thick log law region. The measurements characterising the ABL profile are presented in chapter 5, figure 5.5, for the first roughness design with spires. The measurements for the second design without spires are included in chapter 6, figure 6.5.

Figure 3.2 shows the original atmospheric boundary layer (ABL) roughness that was designed for these experiments. The work done in chapter 5 was carried out using the earlier version of atmospheric roughness with spires (figure 3.2); whereas the work done in chapter 6 was carried out with the roughness visible in figure 3.3.

The final false floor design was made up of 9 panels that covered the 8.1 meter test section, and are listed in table 3.1. The false floors upstream of the test section were built out of nylon so that roughness elements could be easily attached, while panels 8 and 9

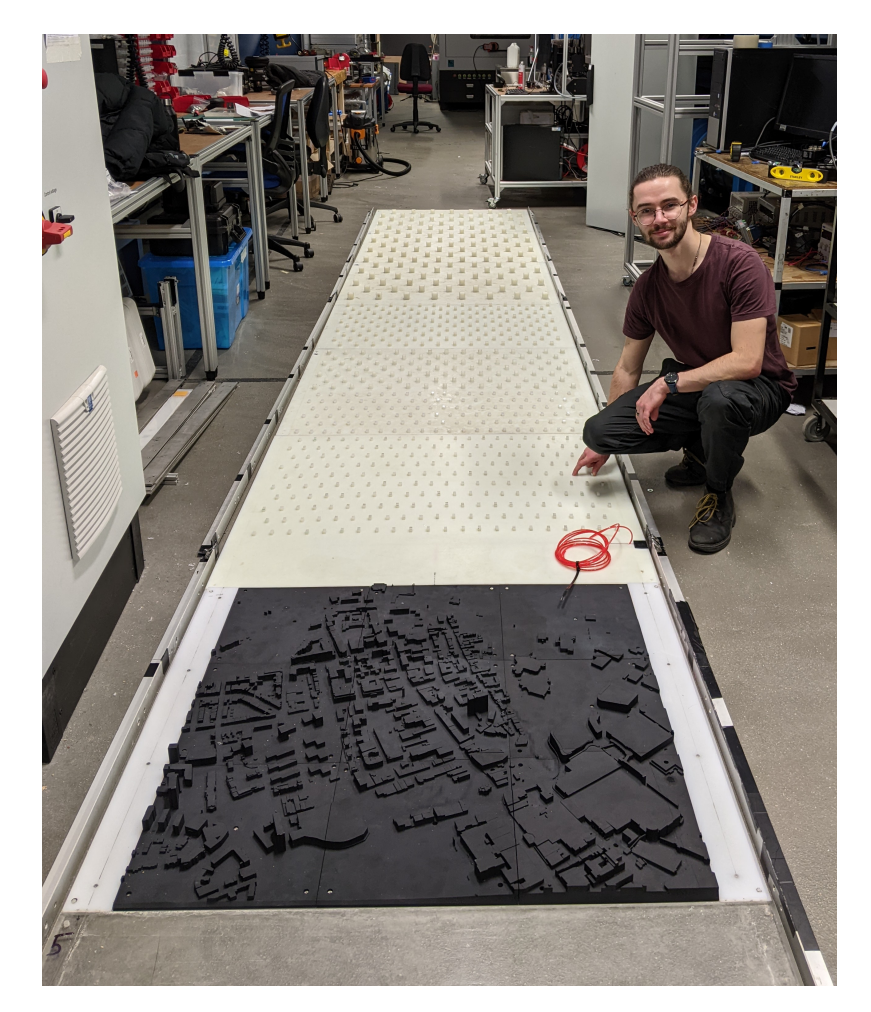


FIGURE 3.3: The atmospheric boundary layer false floors, with test section used in chapter 6, prior to installation in the water tunnel.

were built out of acrylic. The test section varied in material based on the experiment being carried out. All elements were installed into panels using hand tools.

3.2 Measurement Techniques

The measurement of fluid flows can be done in various ways, and the water tunnel is particularly well-suited for optical diagnostics. One of the crucial advantages of full-field optical measurement techniques, rather than point measurements, is that a whole plane of the flow can be examined at once. This allows for a more comprehensive understanding of a previously unknown flow, and is particularly useful when you do not know in advance where the areas of interest in a flow will be.

3.2.1 Particle Image Velocimetry

Particle Image Velocimetry (PIV) is an optical method that allows measurement of the velocity and turbulence of a flow. In order to carry out PIV measurements on a flow, the fluid flow must be seeded with neutrally buoyant tracer particles. The flow must then

Panel	Roughness Type	Panel Length	
1	30 mm cubes, spaced 150 mm apart	750 mm	
	150 mm row spacing		
2	30 mm cubes, spaced 150 mm apart	1000 mm	
	150 mm row spacing		
3	30 mm cubes, spaced 150 mm apart	1000 mm	
	150 mm row spacing		
4	15 mm cubes, spaced 75 mm apart	750 mm	
	75 mm row spacing		
5	Upstream 50% 15 mm cubes, 75 mm spacing,	1000 mm	
	75 mm row spacing		
	Downstream 50% 10 mm cubes, 50 mm spacing,		
	75 mm row spacing		
6	Upstream 80% 10 mm cubes, 50 mm spacing,		
	75 mm row spacing	1000 mm	
	Downstream 20% smooth		
7	Test section	1000 mm	
8	Smooth	1000 mm	
9	Smooth with downslope	600 mm	

TABLE 3.1: Table with details of atmospheric boundary layer roughness, this is the final form of roughness that was used in chapter 6. All panels with roughness are organised in rows with an alternating half spacing offset, and are otherwise evenly dispersed across the panels. Panels 1-7 are visible in figure 3.3.

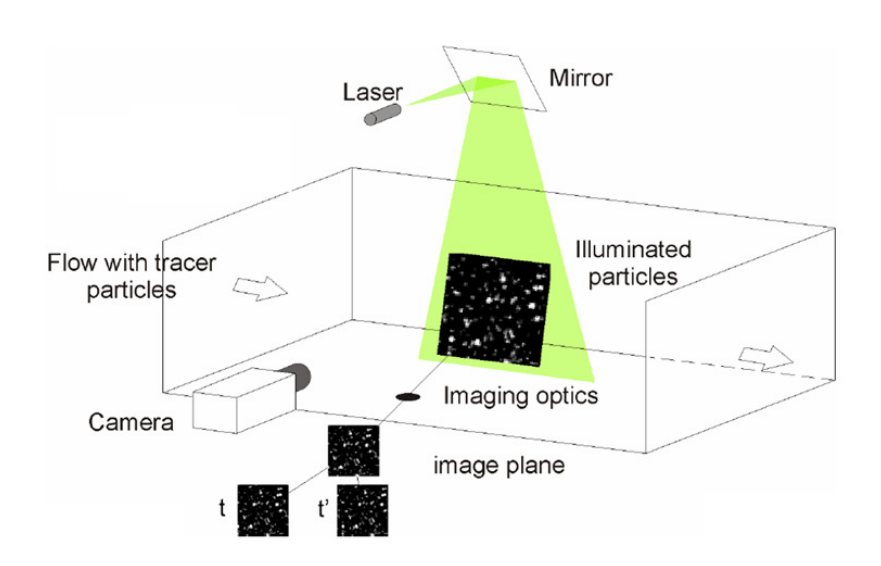


FIGURE 3.4: An example schematic of a PIV setup, (From Von Karman Institute PIV Training 2021.)

be illuminated by a planar laser sheet, and the laser sheet observed by either a specialised PIV camera, or a high speed camera. The camera is then used to capture two images of the flow field, separated by a small time step. An example of what this setup looks like is given in figure 3.4. This image pair is then processed by splitting it down into interrogation windows, with a size determined by the particle seeding density, but often between 16 by 16, and 64 by 64 pixels. The two interrogation windows are then cross-correlated with each other between the two images, so that a mean flow vector can be determined at each window.

Stereo PIV is a technique in which two cameras are aimed at a laser sheet from different angles, and instead of the standard image pair used to calculate velocity vectors, there are now two image pairs per time step (Adrian and Westerweel 2011). The addition of this second camera on the same laser-sheet plane allows for velocity to be known in 3 dimensions, as opposed to the 2-dimensional data provided by traditional planar PIV. This is referred to as a 2 dimensional, 3 component velocity field (2D3C). This is possible using the comparison of velocity measurements from the two image pairs available at each time step.

Detecting systematic errors in PIV results is difficult without a known reference velocity. Most frequently systematic errors are introduced through optical distortions introduced in calibration. In water these can also be caused by the refraction of light through a water surface that is not normal to the PIV camera lens. This can be prevented through the use of a liquid prism and a Scheimpflug adaptor. Measuring the statistical uncertainty in PIV results can be done using a bootstrap method as was done by Lim and Vanderwel (2023). This can give confidence that enough samples have been averaged for a well converged result.

For the PIV experiments carried out in this dissertation, a Litron Nano-PIV, Nd:YAG Pulsed Laser was used, this emits at 532nm from two separate laser heads, and is a class 4 laser. The cameras used for PIV measurements were a pair of LaVision MX 4s which each have a resolution of 4 megapixels.

3.2.2 Basics of Planar Laser Induced Fluorescence

There are two types of PLIF: aqueous PLIF, and gaseous PLIF. Gaseous PLIF is often used in high Mach number flows, for example, to measure unburnt fuel in a supersonic flow (Plate 1999; Higuchi et al. 2019). The vast majority of this review concerns the other form of PLIF, ie. aqueous PLIF, as this is the method which has been used during the course of this dissertation. Aqueous PLIF is a low speed measurement technique which has been developed over the past few decades (Buch and Dahm 1996; Cowen et al. 2001; Vanderwel and Tavoularis 2014; Karasso and Mungal 1997; Crimaldi 2008).

Planar Laser Induced Fluorescence (PLIF), is an optical measurement technique used to measure species concentration in fluid flows. The basic principle of all PLIF measurements is to seed a fluid flow with a species which will fluoresce upon contact

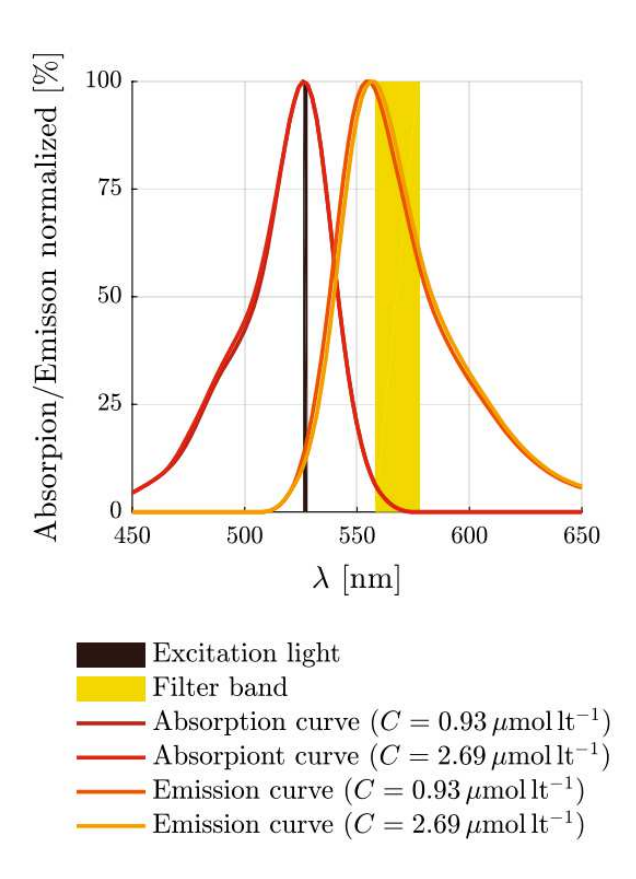


FIGURE 3.5: Emittance and absorbance spectrum of Rhodamine 6G (Baj et al. 2016)

with a laser light, and then shine a laser through the flow to measure the intensity of this fluorescence. A key requirement is that the passive tracer species fluoresces at a different wavelength than it absorbs, which is illustrated in Figure 3.5 for the commonly used dye Rhodamine 6G (Baj et al. 2016). The measuring instrument used is a specialised type of camera which is equipped with a filter to block light from the laser, but not from the fluorescing species. If the PLIF is carried out in a dark environment under these conditions, the result is that it can be assumed that the light intensity detected by the camera at each point is purely that which is emitted by the fluorescing species, with no other contamination. Mapping the intensity of light measured by the camera to a point-by-point species intensity requires the use of an accurate calibration curve. The fluorescent emittance is typically assumed to behave as:

$$E = aIC, (3.1)$$

where E is the intensity of the emitted fluorescent light, a is a calibration constant, C is the dye concentration, and I is the local laser light intensity (Vanderwel and Tavoularis 2014). This equation is only accurate for low concentrations, before the laser begins to be quenched by the dye (Vanderwel and Tavoularis 2014).

Modern advancements in both camera and laser technology are allowing for higher spatial and temporal resolutions, making the technique increasingly powerful. Perhaps more important to PLIF than the frame rate of a camera, however, is it having a high pixel depth, this means that the intensity of light measured by each pixel is stored in

more bits than is standard for most cameras. Most typical digital cameras use an 8 or 12 bit pixel depth, meaning that there are 256 or 4096 light intensity magnitudes respectively. Some of the cameras used for PLIF have 16 bit pixel intensity, which is equivalent to 65536 possible values of light intensity. Consequentially, the uncertainty in PLIF measurements has been decreasing in recent years with improvements in camera technology.

For the PLIF experiments carried out in this dissertation, the same Nano-PIV laser as described in section 3.2.1 was used. The scalar species used was Rhodamine 6G, therefore the test case uses the same laser and scalar as referenced in figure 3.5. The camera used for PLIF measurements was a LaVision S-CMOS which has a 16-bit pixel depth and a 5.5 megapixel resolution.

3.2.3 Combined PIV-PLIF

Aqueous PLIF is predominantly used either for plume visualisation, or for dispersion measurements. Unlike in the case of PIV, it is not viable to disperse the visualising element through the whole flow. This is due to the crucial difference in how the two techniques work, that in PIV each tracking element is uniquely visible. Whereas if dye was uniformly dispersed in PLIF then there would be no useful information to read (Baj et al. 2016). The useful information that can be taken from PLIF is derived from how a concentration gradient moves through the flow. Because of this it is necessary to release the dye for PLIF into the flow during the course of the measurement, whereas in PIV the tracking particles can passively circulate throughout the flow.

Due to the fact that both the PIV and PLIF techniques fundamentally work through a camera observing a laser sheet, it is possible to conduct both measurements simultaneously. This gives a huge amount of information about the flow, with less equipment required than assembling both measurement setups separately. Taking PLIF measurements requires a fluorescent dye to be released into the flow, and conducting PIV measurements requires that tracer particles be mixed through the whole fluid; however, these two forms of tracer do not interfere with each-other. This means both measurements can be taken with the same laser sheet. Simultaneous application of both techniques allows for a high resolution measurement of both the concentration field of the fluorescent dye and of the velocity field of the fluid flow (Cowen et al. 2001).

The main additional equipment required in a coupled PIV-PLIF setup is an additional camera, and this additional camera used to take the PLIF measurements requires a high pixel depth and optical filter for the laser light. The camera used for the PIV measurements does not require an optical filter, and a high resolution and frame rate is more critical than a high pixel depth.

Coupled PIV-PLIF is a technique used and investigated by many groups (Cowen et al. 2001; Tomas et al. 2017; Baj et al. 2016; Sarathi et al. 2012; Vanderwel and Tavoularis 2014). The potential power of this technique is reflected by the large number of papers

attempting to optimise experimental setups. One of the biggest disadvantages of the coupled technique however, is the expense required to assemble a setup still being large relative to most fluid measurement techniques. The paper by Cowen et al. (2001) finds a way to reduce this through using just one camera for both the PLIF and PIV measurements. However, the study shows that to achieve this, two lasers of different wavelengths must be used, and in addition, for time-resolved PLIF results, a camera with both a high pixel depth and a high frame rate is necessary. This one camera setup is also not expandable to include a second camera to conduct stereo PIV as the angle of the camera taking PLIF measurements should be close to perpendicular to the laser sheet, and for stereo PIV the angle between the two cameras must be as close to 90 degrees as possible.

Coupled PIV-PLIF requires careful synchronisation of the multi-camera setup with the laser pulse, but when properly calibrated and timed, it allows the superimposing of more variables than one camera can capture, onto a plane in the freestream. In this way it allows the turbulent species flux of the dye to be calculated across a plane of the flow, and this is a variable that is extremely difficult to directly measure through any other method.

It is possible to take coupled Stereo PIV-PLIF measurements, using three cameras pointed at the same laser sheet. However an aspect of the PLIF technique that is ignored when used in tandem with planar PIV becomes relevant, this is the fact that PLIF species measurements are actually averaged along the thickness of the laser sheet. In planar PIV the laser sheet thickness is aimed to be as narrow as possible at the measurement location, however for stereo PIV the laser sheet needs a more substantial thickness to track particle velocities as they pass from one side to the other. PLIF measurements taken using a thicker laser sheet retain accuracy, as they still correctly represent average species concentration at each point, however they lose resolution. When looking at time averaged fields this is not an issue, however with instantaneous fields, a lack of resolution makes flow structures, and peaks in species concentration less well defined.

3.3 Known issues to be addressed when conducting PLIF

3.3.1 Non-linearity of the dye response

There are various problems that arise and phenomena that must be tracked when conducting PLIF measurements. One problem is possible non-linearity in the dye response. What this means is that the intensity of the light emitted by the dye when exposed to the laser is not directly proportional to the dye concentration. In most cases, it is assumed that the dye response is linear for low enough concentrations. However, beyond a certain cut-off, the dye begins to become saturated. This means that once a large proportion of the dye particles are already excited, increasing the incoming light intensity begins to give diminishing returns in fluorescent output.

Plotting the ratio of input laser light intensity against output fluorescent light intensity gives a calibration curve. In equation 3.1 this is represented as the calibration constant *a*, this equation makes the assumption that the measurement happens within the linear region of this calibration curve. It is common in literature to only use two datapoints to generate a calibration curve and assume this linear relationship is true. This is common mainly due to time constraints and the fact that calibration must be done before each series of measurements (Vanderwel and Tavoularis 2014).

3.3.2 Secondary Fluorescence Effects

Secondary out-of-plane fluorescent absorption in the dye calibration or experiment can lead to further inaccuracies (Vanderwel and Tavoularis 2014). Secondary fluorescence related losses have a less dramatic effect on the light measured by the camera than losses due to saturation do, however, they are present at all light intensities.

Figure 3.5 illustrates how the emittance curve of Rhodamine 6G overlaps with the higher wavelengths of the absorption curve, specifically this is particularly a problem between 540 - 550 nm. The implication of this is that a small amount of the light re-emitted by the fluorescent dye will be absorbed by other dye molecules, exciting them but overall emitting less light that will be measured by the camera. Due to this effect, it is not wholly accurate to assume that equation 3.1 for linear fluorescent emittance is true, even inside the so called "linear region" (Karasso and Mungal 1997).

3.3.3 Attenuation in Calibration

Attenuation happens due to the finite number of photons of light being absorbed by the dye particles as they pass through the solution. This contrasts with the previous problem of non linearity in the dye response happening due to the finite number of non excited dye particles in a solution being reduced through interaction with the photons.

The Beer-Lambert law accounts for any attenuation of light as it passes through a medium and is given by

$$A = e^{\varepsilon r C}, \tag{3.2}$$

where A is absorbance due to attenuation, ε is absorptivity, r is laser path length, and C is concentration (Swinehart 1962).

This equation is of importance in calculating laser attenuation when creating a PLIF calibration. This process will be discussed in detail in section 4.2 as accounting for this correctly is one of the methodology developments discussed in section 4.1.

During experiments, the effect of light attenuation due to dye released from the source can be assumed to be negligible. This is because the fluid dye is released into water, so the effect of molecular diffusion is limited. This means the dye stays in more tightly

packed flow structures, as opposed to dispersing rapidly to a more uniform concentration.

3.3.4 Fluctuations in laser intensity

Laser intensity fluctuation can contribute a significant amount of error to the overall results obtained in PLIF. In general, laser intensity fluctuation is of the order of 2-7% (Bruchhausen et al. 2005). This intensity fluctuation is a lot more significant in the case of pulsed lasers than continuous ones. Unfortunately, however, in PLIF, pulsed lasers are preferable as they are generally capable of higher intensity light for the periods they are firing, and this higher intensity light is useful for increasing the image clarity of the illuminated dye, and reducing losses from attenuation due to the Beer-Lambert law.

Fortunately, energy monitors can be equipped to a laser in order to siphon off a specific portion of the laser energy and measure the relative intensity of this portion. This allows the pulse to pulse relative beam intensity to be corrected for. This circumvents the problem of varying beam intensity as it can directly be accounted for in the equation for fluorescent emittance (eq. 3.1), allowing the dye concentration to be calculated without this error being significant.

3.4 Methodology study into calibration methods and accuracy

A proportion of the work carried out in this dissertation was to carry out a detailed calibration study. There were many reasons for which this needed to be carried out. First and foremost was the need to check that the assumption made by Vanderwel and Tavoularis (2014), that using just two datapoints and then using these to match to a calibration curve, is a valid process. This is dependent on the calibration curve being linear within the limit of concentrations encountered when carrying out experiments. To check this, a calibration curve was generated using 11 datapoints between dye concentrations of 0 mg/L and 0.5 mg/L (shown in figure 3.6). Carrying out these measurements illustrated the necessity of a method to create a calibration curve from fewer datapoints, as collecting the 11 sets of data needed here took 10 hours over two days, without any post processing. Meaning that it is, therefore, entirely impractical to expect to generate a detailed calibration curve from this much data as a preliminary step to running PLIF analysis each day.

The aim of this calibration study was to develop a method to create a linear PLIF calibration for use in the rest of this project. A preliminary step to doing this was verifying the significance of each of the known issues with the PLIF technique. Another goal was testing whether using the Davis 10.2 software package for this purpose would match the accuracy of a purpose-built code. However it was discovered that using the Davis 10.2 software would not allow for as high a level of accuracy, and that it was

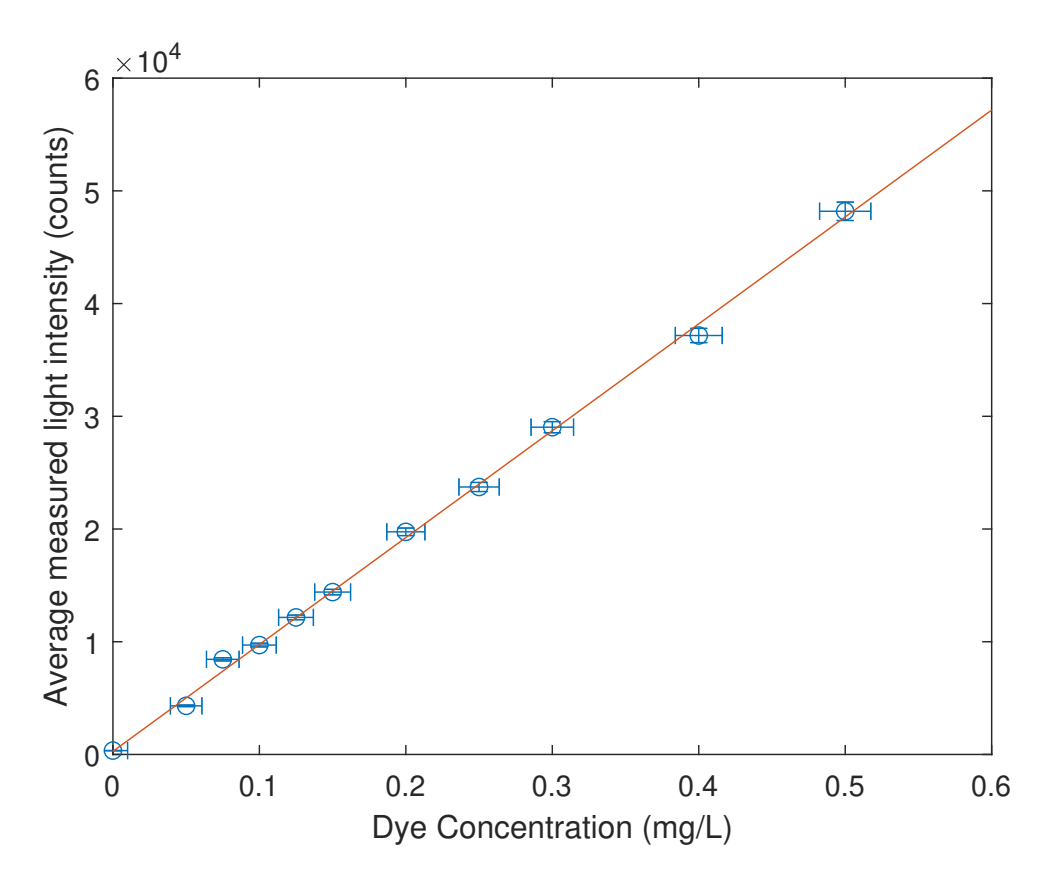


FIGURE 3.6: A graph showing fluorescent light intensity against dye concentration in a study into the PLIF calibration process. Error bars were calculated using the variance in fluorescence across each tank, and the uncertainty in dye concentration.

preferable to develop a purpose built Matlab package. This is because the Davis 10.2 software was built with limitations in the areas it could apply attenuation corrections, and also the function that were used to correct for attenuation were not disclosed or editable by the user. The Matlab package that was developed as an alternative is explained in chapter 4.

The Davis 10.2 software package had the limitation that it could only calibrate using dye tanks smaller than the field of view of the camera. If any part of a calibration tank was located outside the field of view of the PLIF camera then attenuation through that portion could not be accounted for. Due to this limitation two new calibration tanks were produced for this calibration study, and then continually used throughout the rest of this PhD, despite switching to using Matlab code instead of Davis 10.2 after this calibration study. These tanks had a height of 120 mm, a depth of 20 mm, and a width of 150 mm, one of these is shown in figure 3.7. These dimensions were chosen so that the full height could be within the field of view of the PLIF camera for the calibration study. These tanks were built using clear acrylic on the top, bottom, and sides. The front and back panels were glass, this was used to provide the best possible optical access in the orientation the camera would require.

The two dye tanks were filled, cleaned, and emptied repeatedly during the calibration study. After the calibration study they were filled with 0.03mg/l, and 0.05mg/l



FIGURE 3.7: An image of one of the calibration tanks.

solutions of Rhodamine 6G, and sealed robustly so that they could be used for calibration of all future experiments.

The process of mixing the dye concentrations that were used for both filling the calibration tanks, and releasing during experiments, was done using Rhodamine 6G powder. This powder was weighed accurately, using a mass balance, and diluted using the appropriate quantities of distilled water to create a solution at 5 mg/l \pm 1%. This solution was then diluted further into the solutions used in calibration tanks.

The graph shown in figure 3.6 validates the PLIF methodology, when calibrated using Matlab code, by forming a straight line. This implies that the fluorescent emittance from a calibration tank is increasing linearly as the concentration of dye in the calibration tank increases. This validates using this assumption when calibrating PLIF images. This linear relationship was only visible when attenuation was correctly accounted for in the tanks.

3.4.1 Developing improvements to the PLIF methodology

The work carried out in this calibration study did help to develop the code base used during the rest of this PhD. In total it amounted to a large proportion of the work carried out for the PhD. Particularly, nearly the entire first year was spent on this subject, with significant portions of the rest of the time spent on diversions into further methodology improvement.

Due to this large time investment and the sophistication of the code base used in this PhD, it was decided that publishing it for use by the scientific community would be advantageous. A paper was written and submitted for review by the Journal of Open Source Software alongside an accompanying Github package (Rich T 2024). Because of

the publishing standards for both the code in the Github repository and the paper itself, this paper and its accompanying code package has been in review for a significant amount of time now, nevertheless it is hoped that this will soon be published. The Github repository has already been cloned by several members of the scientific community hoping to start using the PLIF technique. The content from the current version of this paper has been included in section 4.1.

Further methodology development of the PLIF technique to improve measurement accuracy is presented in chapter 4.

3.5 Experiments overview

The experimental campaigns carried out as part of this dissertation are listed as follows:

- 1. PLIF calibration study and jet flow validation
- 2. Individual tall building investigation
- 3. Southampton city study

The results of investigation 1 are discussed in section 4.2. The jet flow validation was carried out to prove the accuracy of the PLIF techniques and these results were found to satisfactorily prove this.

The objective of investigation 2 was to quantitatively examine the flow structures around a tall building using the PLIF technique. This objective was set to increase understanding of fluid flow around idealised bluff bodies. Particularly by including concentration measurements as opposed to just velocity, as has been done more frequently in previous measurements into bluff bodies. The results of investigation 2 have been published in the journal Boundary Layer Meteorology (Rich and Vanderwel 2024), and this has been included as chapter 5.

The objective of investigation 3 was to measure full fields of velocity and concentration using simultaneous PIV-PLIF, across a realistic city model. The purpose of this was to produce and analyse this unique dataset, in order to discover new insights into the transport of a scalar plume across this model. Investigation 3 has been the main focus of this PhD and has been written up into a paper that is intended to be submitted to the journal Building and the Environment. This paper has been included in its current state as chapter 6.

Chapter 4

Methodology: Advancement of the Planar Laser Induced Fluorescence Technique

The aim of this chapter is to present advances to the PLIF technique developed during this dissertation and the code that has been written based on them. The new software is presented in 4.1, and validated in 4.2. The structure of section 4.1 follows the form used in papers published in the Journal of Open Source Software. The content of section 4.1 is from a short paper that has been submitted to this journal and which is in review. It is intended as a paper that accompanies and will be included inside a Github software package (Rich T 2024). As such, a lot of its content is listing the functions in the package, and a very brief background on PLIF.

4.1 A Planar Laser Induced Fluorescence Software Package

4.1.1 Summary

Planar laser induced fluorescence (PLIF) is a technique used to quantitatively measure the concentration of a fluorescent species in a flow. This paper and code are specifically designed for aqueous applications in which a fluorescent dye is illuminated by a planar laser sheet. A camera measures the intensity of fluorescence, which this code uses to calculate the concentration of dye. A multiple step calibration is required using a set of specific calibration images. This process calibrates both the geometric (pixel to mm) scale and the transfer function to map the measured fluorescent intensity to the local dye concentration. Biases can be introduced from background dye build-up or laser attenuation. This code package is designed to allow the user to account for these biases using tunable parameters based on experimental measurements and additional calibration images.

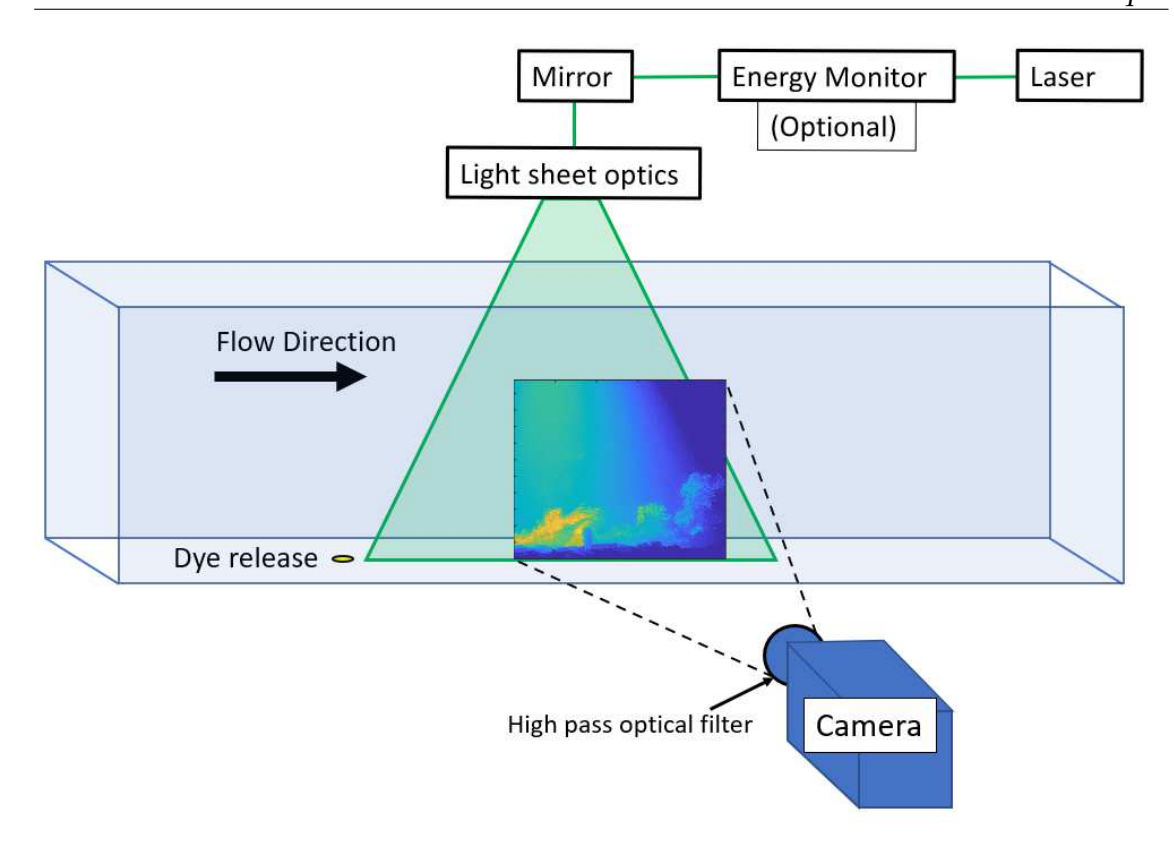


FIGURE 4.1: A diagram of an example PLIF experimental setup.

4.1.2 Statement of Need

The applications of experimental concentration measurements in a fluid flow are extensive. Some examples include urban flows (Karra et al. 2017; Lim et al. 2022), turbulent jets (Milton-McGurk et al. 2020), pollutant dispersion over roughness (Djenidi et al. 2008), and within boundary layers (Tomas et al. 2017). When attempting to map these varied experimental cases it is valuable to be able to measure dispersion across full planes, as opposed to using point measurements. Typically fast flame ionisation detectors (FFID) are considered the gold standard for point measurements (Talluru et al. 2018).

In order to carry out a PLIF investigation it is necessary to have a large amount of specialised equipment (see 4.1), and also to have a complex post processing code along with the expertise to use it. It is, however, possible to run a PLIF investigation without all of the tools recommended to reduce uncertainty. For example a laser energy monitor can be disregarded; uncertainty will rise but PLIF is still possible. The same is true of a specialised PLIF camera with a high pixel depth. This code is designed for use with aqueous PLIF, as this is the type of PLIF that uses calibration tanks. Having a water-based experimental facility can be a significant barrier to entry to carrying out aqueous PLIF. It is hoped that by releasing this software package as an open source tool, lack of post-processing software will be removed as one of these many barriers to entry.

This PLIF calibration package is a set of MATLAB tools that enable the user to process PLIF datasets. Concentration calibration images are images in which a tank of dye of a known concentration is introduced into the experimental setup, in order to record image intensity values that relate to known concentration values. Attention was drawn (Vanderwel and Tavoularis 2014; Crimaldi 2008) to the necessity to correct concentration calibration images, as they themselves can create a bias due to attenuation diminishing the laser intensity as the laser rays pass through the calibration tanks. This bias is not present to as high a degree in the experimental images and so attenuation corrections are focused on the calibration process. If not corrected for then this biases the experiment to be more sensitive to dye near the laser sheet source. This problem was addressed by Baj et al. (2016) in a novel way using the traversal of a narrow tank, however it is possible to account for this problem more simply through the calculation of absorptivity (ε). This software package provides checks along the processing steps that it is working as intended, these are in the form of graphs displaying interim calibration products, with notes of the expected observations. This package is primarily intended for academic research use.

4.1.3 Package Overview

The functions in this package are designed to be run through a main function. In this package, an example of a main function is included (example.m). The functions are designed to generate a calibration matrix and save it to a file. This calibration matrix is an array of multipliers that correspond to each pixel in an image and are later multiplied in. These multipliers represent the gradient between measured intensity and dye concentration at each point in the flow. The background subtraction represents a zero offset for this gradient, and is subtracted before the scale is applied. The *calculate calibration* and *apply calibration* sections of this code are designed to be independently executable.

Figure 4.2 shows the process of a PLIF calibration in diagram form. Example inputs and outputs are taken from an investigation into urban air pollution that was carried out at the University of Southampton. The equation for experimentally measured fluorescent emittance, is:

$$E = aI(C - b), (4.1)$$

in which E is the emittance, a is a calibration constant, I is the light intensity, C is the dye concentration, and b is the background intensity. This equation is slightly different than the fluorescent emittance equation (equation 3.1) in that it accounts for a level of background light (aIb).

This is used in the process described by figure 4.2. Conducting this full pixel by pixel calibration allows the constant (a) and the light intensity (I) to be accounted for, so that the concentration (C) can be quantitatively calculated using the emittance (E). The high pass filter shown in figure 4.1 is necessary in order to eliminate the camera's ability to



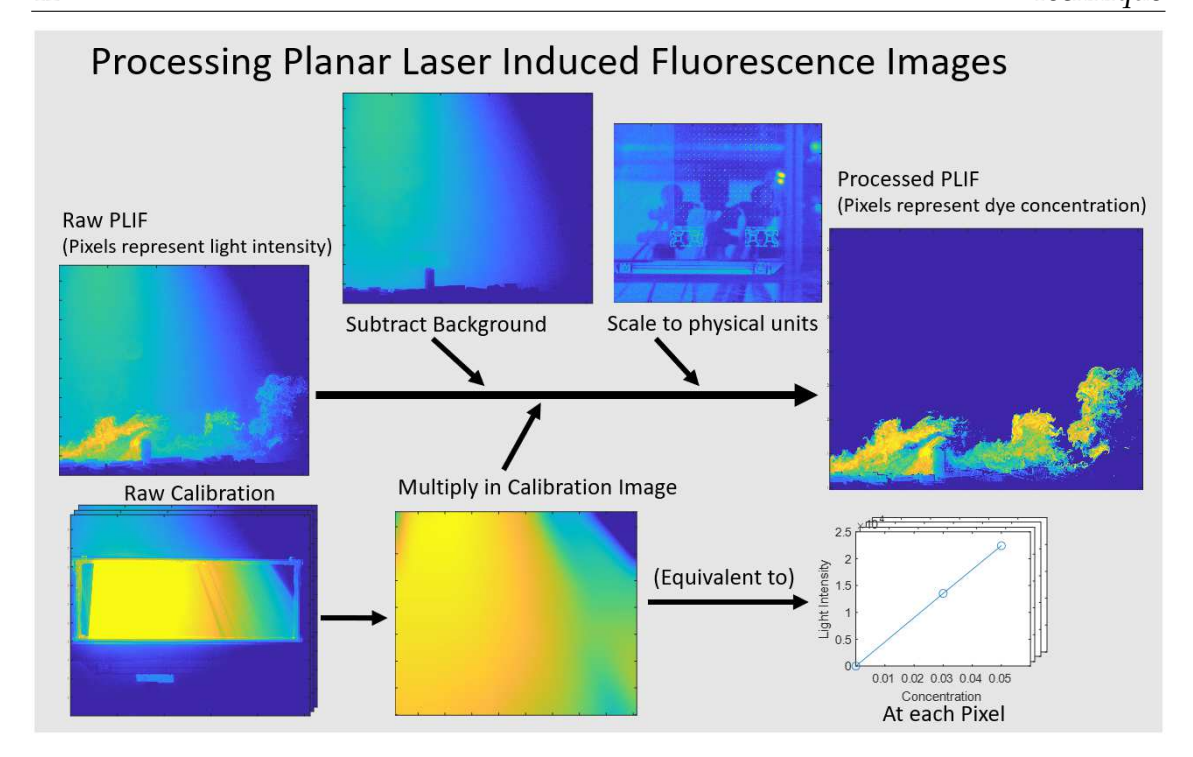


FIGURE 4.2: A diagram of PLIF post processing.

measure intensity at the absorption wavelength of the dye (I) (depicted in figure 3.5). Without taking this step, the assumption that all light measured by the camera is only that which is emitted by the dye (E) is invalid, and instead (E + I) is what would be measured. In the code the first step is the background subtraction (removing b in the equation). The calibration image is then generated from the gradient of the line of pixel intensity against dye concentration; in the equation for fluorescent emittance it is equivalent to a pixel by pixel value of aI. After this step the raw image has been transformed from an array of pixels representing measured fluorescent emittance, to one representing scalar concentration.

In order to calibrate an accurate value of the light intensity (*I*) at each pixel, the attenuation through the calibration tank must be accounted for. This is done using the Beer-Lambert law, given previously in equation 3.2.

In the case of a calibration image the concentration (C) and absorptivity (ε) are constant, and r is constant but has a different value at each pixel. The definition of absorbance (A) between two points separated by a distance r can be defined as:

$$A = I_{x2}/I_{x1}, (4.2)$$

where I_{x1} is light intensity at x_1 , and I_{x2} is light intensity at x_2 .

Equations 3.2 and 4.2 can be rearranged to obtain another equation referring to absorbance in terms of light intensity. These two can be rearranged to obtain an equation in which absorptivity (ε) is the only unknown. This takes the form:

$$I_{x2}/I_{x1} = e^{\varepsilon rC}, (4.3)$$

in which I_{x1} is light intensity at point 1, I_{x2} is light intensity at point 2, ε is absorptivity, r is path length between point 1 and point 2, and C is concentration.

Equation 4.3 can be solved at each pixel of each calibration image, and used in order to create an image which is analogous to each row of pixels being illuminated as if they were the top row closest to the laser. This removes the problem of high attenuation during the calibration process, and gives an accurate estimation of the local light intensity (I). This method is dependent on having an accurate estimate of the absorptivity (ϵ). Methods to calculate the absorptivity ϵ of a solution vary. This software package includes a package of code to iteratively calculate this from the calibration images. This process mostly uses the existing code and is designed to be optional. This would be represented in figure 4.2 by a repeating loop of the bottom row, in which the calibration image is generated. This loop runs until the ratio of light intensities measured from the calibration tanks, match the ratios of dye concentrations within them, and it can be configured to prioritize a specific region of the image for optimization.

4.1.4 Package Functions

Below is a list of all the functions included in the package.

4.1.5 PLIF Calibration functions - Calculate Calibration

- 1. Parent function calib_calculate_coefficients : Parent function that calls other calibration functions.
- 2. Average calib_average_frames : A function to average the sets of images used for each calibration tank position.

Input: 7 sets of calibration images.

Output: 7 averaged calibration images.

3. Merge - calib_merge_frames : A function to merge the 3 tank positions for each dye concentration. The background image does not need merging.

Input: 2 sets of 3 averaged calibration images.

Output: 2 merged calibration Images.

4. Trace Rays - calib_trace_rays: A function requiring user input to calculate the laser origin based on visible laser lines in the calibration images. In this step sections of the image can also be selected to be deleted and interpolated.

Input: Laser streak locations.

Output: Laser Source coordinates.

44

5. Correct Attenuation - calib_correct_attenuation : Application of attenuation correction using molar absorptivity (Epsilon), laser source location, and out of frame tank height.

Input: Molar absorptivity, out of frame tank height, 2 images.

Output: 2 Images.

6. Background Intensity Gradient - calculate_background_intensity_gradient: Uses GetBackgroundIntensity on every experiment image to plot the increase in background concentration between start and end of experiment.

Input: All experimental Images.

Output: Gradient of increase in background intensity.

7. Assess Calibration - calib_attenuation_summary_figures : Prints output figures to check the final inputs to the calibration matrix.

Input: Background calibration image and two pre-processed calibration images.

Output: Graphs to check validity of previous calibration steps.

8. Output Calibration - calib_make_final_frame : Creates calibration curve for each pixel in image and exports as matrix.

Input: Background calibration image and two pre-processed calibration images.

Output: Final calibration matrix.

PLIF Processing Function - Apply Calibration

1. apply_calibration_coefficients: Applies calibration matrix to experimental images.

Input: Experimental images, Calibration matrix.

Output: Processed PLIF images.

4.1.7 Epsilon Optimisation Function (Optional)

1. Epsilon Iteration - epsilon_correct_attenuation: Uses bisection method to optimise absorptivity value for calibration images.

Input: Laser source coordinates, averaged and merged calibration images.

Output: Optimal Epsilon value for this specific set of images.

File Accessing Sub-functions

1. get_scale_origin: Uses an image of the calibration plate to apply a user defined origin to all images.

Input: Calibration Image, User input.

Output: Image Origin in x and y.

2. get_plif_image: Reads image file, converts from select formats to numerical arrays.

Input: Path to image.

Output: Image as numerical array.

3. get_laser_origin: Uses user defined ray tracing to calculate origin of the laser sheet.

Input: Calibration Images, User input.

Output: Laser Origin in x and y.

4. get_dye_conc_filenames: Creates list of file names for calibration concentrations.

Input: Concentrations of dye in calibration tanks.

Output: List of calibration image file names.

5. get_default_unset_parameters: Uses default values from experiments carried out at Southampton as unset values.

Input: n/a

Output: Unset parameters.

get_background_intensity: Uses a selection of the freestream of the flow with no scalar to estimate the intensity of the background, relative to the original before the experiment began.

Input: Experiment Image, Freestream location.

Output: Relative background intensity.

4.1.9 Acknowledgements and Author Contribution Statement

The contributions of Dr Edward Parkinson, Dr Desmond Lim, and Professor Christina Vanderwel to this code package are acknowledged. Dr Parkinson for his reformatting of this code into a modular form with more consistency across functions. Dr Lim for his work on the previous code base that this expanded version was built from. Professor Vanderwel helped with editing the manuscript associated with this code.

4.2 Assessing the accuracy of the Planar Laser Induced Fluorescence technique using a Mass Balance experimental case

The following are the results of a methodology study into the PLIF technique and a validation experiment.

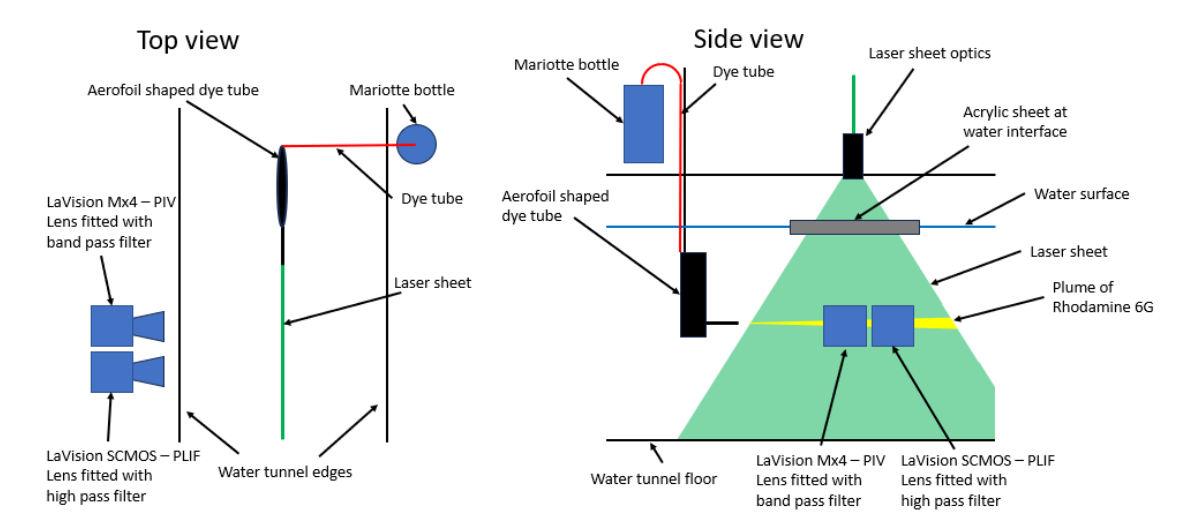


FIGURE 4.3: A diagram showing a top and side view of the experimental setup used to measure the Rhodamine 6G jet.

4.2.1 Introduction

In this section the results of a study into the PLIF technique are presented. This investigation took the form of a mass balance study in which PLIF data was used to calculate the mass flow rate of a jet, and this was compared to the mass flow rate measured using a flow meter at the inlet of the jet.

While calculating the mass flow rate of the jet, attenuation in the calibration tank had to be taken into account. This was done using the novel method developed to calculate the absorptivity of the dye solution that has been used during this dissertation. The calculated results of the mass flow rate were compared with that of a flow meter, and with the calculated value without this attenuation correction.

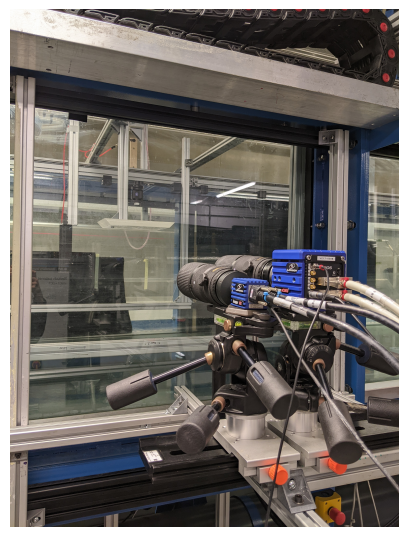
In a PLIF calibration, attenuation correction refers to a correction for the light that is being blocked along each ray path as it travels through a calibration tank (an example of which is shown in figure 3.7). This is necessary as, in an experimental case, the calibration tank will not be there, and therefore the light intensity will not be diminishing as much along each ray. The attenuation correction effectively brightens the counts measured in the pixels of a calibration tank that are far from the laser source, in proportion to the absorptivity of the Rhodamine 6G solution. The attenuation happens according to the Beer-Lambert law (equation 3.2).

4.2.2 Methodology

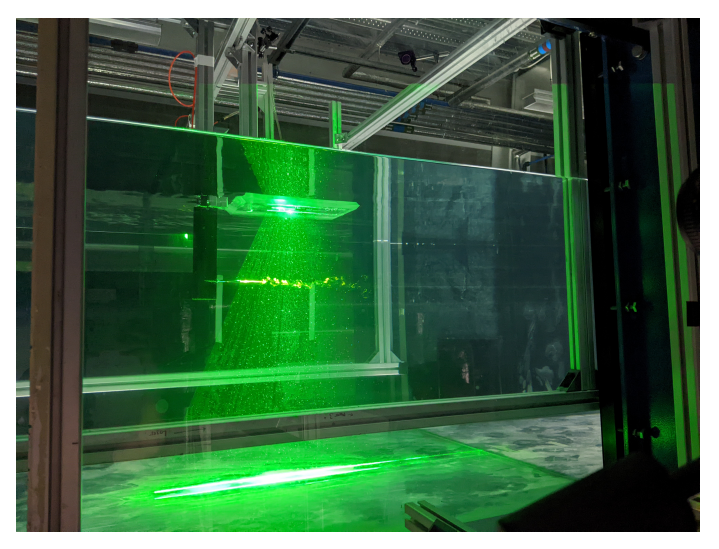
An experiment was carried out in which a jet of Rhodamine 6G was released into the University of Southampton's recirculating water tunnel. A diagram of the experimental setup is shown in figure 4.3. For the purposes of this study the water tunnel was set to the lowest possible velocity of 0.025m/s. This was so that it would prevent dye build-up in the measurement area but the relative velocity of the jet would still be high. Jet

velocity was kept constant at a speed of 0.29m/s using a Mariotte bottle positioned above the water tunnel.

Measurements were carried out using a side by side arrangement of a LaVision MX-4 PIV camera equipped with a band pass filter and a LaVision S-CMOS PLIF camera equipped with a high pass filter. These cameras both had 200 mm lenses focused on a shared field of view 6 cm wide and 5 cm high. A field of view this small was chosen to maximise the resolution with which the width of the plume was resolved. This field of view was illuminated with an Nd:YAG pulsed laser to enable acquisition of simultaneous PIV-PLIF data.



(A) An image of the MX-4 and S-CMOS cameras aimed at the test section.



(B) An image showing the dye plume under the laser sheet. This image was taken during setup, during actual image acquisition the background lights in the lab were turned off.

FIGURE 4.4: Photos showing the experimental setup used during this investigation.

The jet was injected into the flow through a 3D printed, aerofoil shaped, tube that descended through the water into the free-stream of the flow (visible in figure 4.4). The 3D printed tube had a copper pipe fastened to the end to elongate the tube behind the aerofoil and provide a more precisely machined outlet, this pipe had an internal diameter of 2.5 mm. A laser sheet was aligned carefully with the centre-line of this dye tube. Multiple measurements were taken with the laser sheet location moved slightly in the cross-stream direction. The laser sheet location that gave the highest mean concentration and velocity values was the location that was used in the final experiment. This was done as a test to make certain that measurements were being taken on the centreline of the jet. Particular care was taken with this step as it was recognised that a small deviation from the centreline would have resulted in a large inaccuracy in results. It was estimated that the centreline location was accurate to within ± 1 mm, the uncertainty caused by this has been investigated in section 4.2.4.

In these experiments the jet outlet is taken as the origin and distances are normalised by the internal diameter of the outlet (D = 2.5 mm). In all analysis, x refers to the downstream direction, y refers to the cross-stream direction, and z refers to the vertical direction.

PIV images were processed in Davis 10.2 and then post-processed in custom Matlab code. PLIF images were processed using the code package described in chapter 4.1. A comparison would have been run using Davis 10.2 to process the PLIF images, however, due to the small field of view of the PLIF camera this was not possible. This is because Davis 10.2 can only use calibration tanks smaller than the field of view of the PLIF camera. All PIV vector fields were processed using 48 pixel by 48 pixel windows, with a 50% overlap. The resolution in PIV vectors was one vector every 0.18 mm. Whereas, the PLIF resolution was 0.02 mm. Data was acquired at a rate of 12.5 Hz and 2000 frames were captured. With this data acquisition rate and the flow rate of the jet the snapshots were deemed to be statistically independent. This is because the mean jet velocity caused a displacement of 2D between each frame acquisition, and the largest length-scales in the flow were of a comparable size.

4.2.3 Explanation of PLIF Calibration Process

Calibrating a PLIF experiment is carried out pixel by pixel across the field of view of a PLIF camera. Fundamentally this is a process that equates light measured by a camera (measured in counts) to a concentration of fluorescent dye in a flow (typically measured in mg/l. The code used to process PLIF images for this experiment was the same as that described in section 4.1. The basic workings of this code were described when it was introduced, however the process shall be explained here in further detail.

The process that happens at each pixel of these PLIF images begins with image preprocessing. The preprocessing is carried out for both the background calibration images, and the uniform tank calibration images. Chronologically this begins with first applying an energy monitor correction for the pulse to pulse laser strength. Next the multiples of images at each concentration are averaged down to one single image for the background and one for each tank concentration. Streaks in each dye tank are used to identify the location of the laser sheet source.

Using the known dimensions and location of the calibration tank, and the direction of each laser streak relative to them, it is possible to assign a value r to each pixel. This value is the distance that each laser streak has passed through the calibration tank to reach that pixel. This value is then used in equation 3.2 to calculate the local attenuation. This local attenuation value is then added to each pixel's light intensity, so that a calibration image equivalent to a case with no attenuation within the tank can be generated. This attenuation corrected calibration image allows for a more accurate calculation of the local light intensity at each pixel during experiments, due to the fact that the calibration tanks will not be present in the field of view during experiments. This code includes an optional package that can be used in order to know the most accurate value of ε to use in equation 3.2. An explanation of this process is given with the results in section 4.2.5.

The two corrected tank images then have anything outside the limits of the tanks removed, and are extrapolated to fill the full field of view. This extrapolation is done radially from the laser source located in the previous step.

For clarity this explanation will refer to a pixel not an image when describing this process from this point on. So when referring to the background intensity value this means the intensity of a pixel in the background image. Which pixel is not important, as long as it is in the same location as the other pixel intensity values, for example they might all be at 1200:1200 within the output arrays of the S-CMOS camera.

It is now necessary to transform the dye-tank pixel intensities into a function, by which the light intensity of the pixel measured in the experimental image can be calibrated. It might be assumed that there are three dye concentration values at which the fluorescent light intensity is known. It is, however, not usually accurate to assume that the background dye concentration is exactly zero. However, if the assumption is made that only fluorescing light is measured by the PLIF camera, then a further logical assumption is that with no dye present, the measured light intensity will be exactly zero. The implication of this is that to calculate a gradient on a graph of light intensity against concentration, this should be done between the two tank intensity values and zero, instead of between the two tank intensity values and the background value. The assumption that with no dye present, the measured light intensity will be zero, was tested using fresh water illuminated by the laser. It was found that the counts measured by the camera (equipped with a high-pass filter) did not rise noticeably above the sensor noise level.

Technically only two points of light intensity and concentration values are necessary to calculate the gradient of this line. In this case the three possible gradients are all calculated and averaged. These gradients are calculated using the simple formula:

$$m_{cal} = \frac{c_{cal2} - c_{cal1}}{i_{cal2} - i_{cal1}},\tag{4.4}$$

in which m_{cal} is the calibration gradient (equivalent to aI in equation 4.1), i_{cal} is the calibration light intensity, and c_{cal} is the known concentration value, with 1 and 2 representing the two concentrations chosen. This gives a final mean PLIF calibration gradient m_{cal} which is ready to apply to experimental images.

The steps up to this point have had the goal of generating the m_{cal} value so that it may be used to calibrate the experimental images. During the calibration of PLIF experimental images, the background light intensity must be subtracted. When using a recirculating flow facility this becomes more complex than simply subtracting an image of the freestream before the experiments have begun. The technique that was developed in this code was to define an area of each experimental image as the flow freestream, this area being the same on all images and somewhere that no dye entered. This area was then averaged to give a background light intensity value. When these values were plotted against image number, there was a noticeable upwards trend across the duration

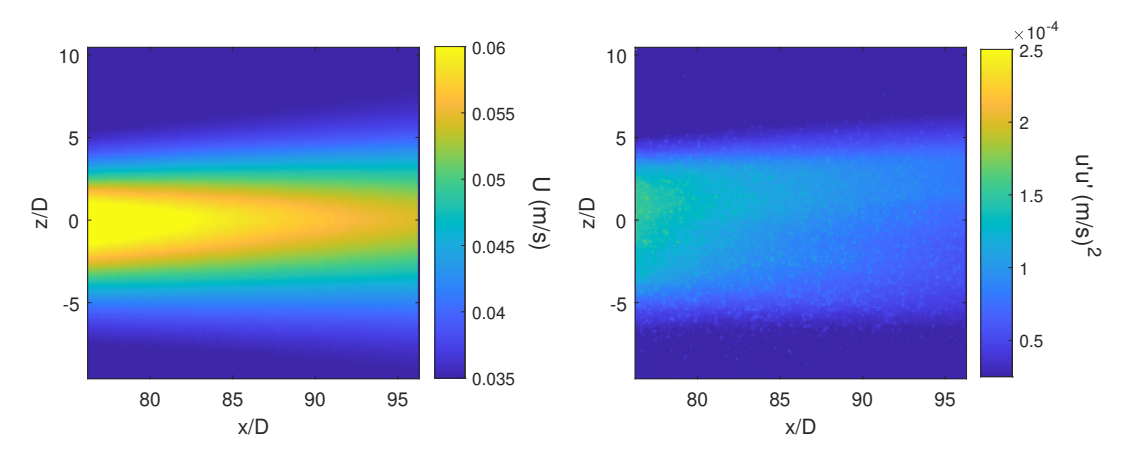


FIGURE 4.5: (a) The mean streamwise velocity, and (b) the streamwise velocity variance. These were averaged from 2000 PIV images.

of an experiment. Fitting a straight line to these values gives a numerical value for the increase in background light intensity.

The line fit to background light intensity can then be normalised using the light intensity value for the background image. This typically gives a gradient starting at 1 and growing towards a maximum value between 1.03 and 1.10 over the course of an experiment. The background to be subtracted from experiment images is multiplied by a correction factor that linearly scales from 1 to the maximum value while processing through from the first to last experimental images. This gives a final scaled background intensity referred to as b_{ij} due to the fact that it varies as a function of image number.

Calibrating the experimental image is again done pixel by pixel. It is important that the experimental intensity (e_i) first has the background intensity (b_i) subtracted. It can then be multiplied by the calibration gradient (m_{cal}) . At this point the pixel discussed has been successfully calibrated, and has been converted into units of concentration. This process must now be iterated through every pixel in the field of view, and every experimental image in the data-set.

4.2.4 Results

The relative velocity of the jet with the water at the outlet, and the internal diameter of the outlet gave a jet Reynolds number (R_{jet}) of 560. The flow rate of the injected dye was $84cm^3/min\pm2.4\%$. This is the flow rate of the Rhodamine 6G dye solution into the flow, this solution had a source concentration of $0.5mg/l\pm4.5\%$. Using these values in the equation

$$\dot{m}_{Rhodamine} = QC_s, \tag{4.5}$$

the mass flow rate of Rhodamine in the jet was calculated to be $1.40*10^{-6}g/s$ with an uncertainty of $\pm 11.59\%$. This number and uncertainty represents the value as calculated by the flow meter.

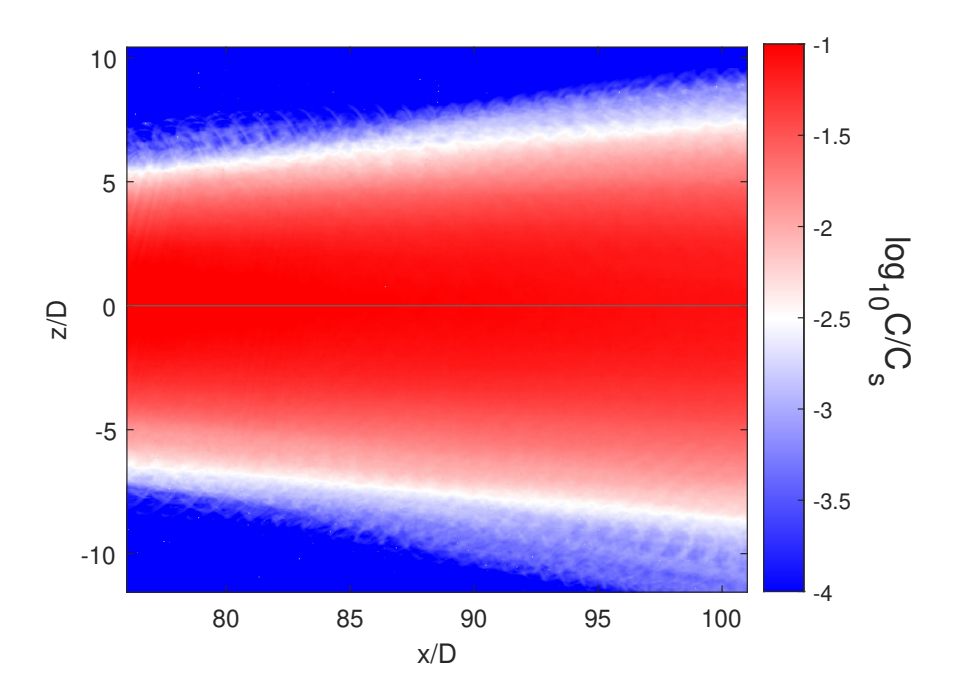


FIGURE 4.6: The mean concentration field across the jet, calibrated with an attenuation correction. The centreline of the jet is indicated by the black line.

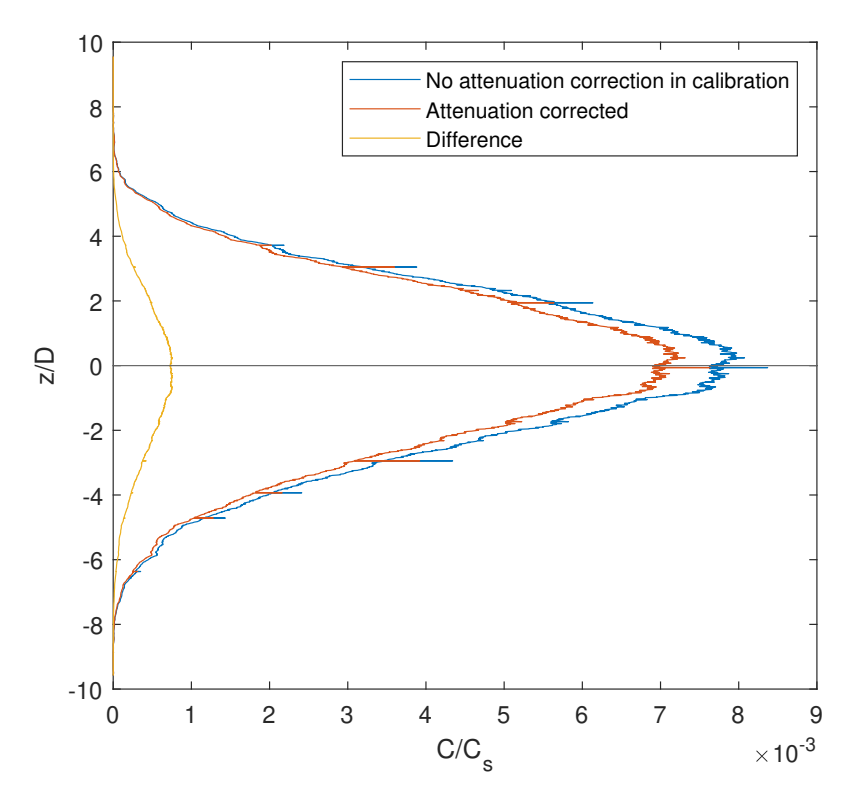


FIGURE 4.7: A comparison of profiles of the mean dye concentration. Calibrated both with and without an attenuation correction. These profiles were extracted at x/D = 80.

Velocity statistics of the jet can be observed in figures 4.5(a) and 4.5(b). Figure 4.5(a) shows the mean of the streamwise velocity values that were used to calculate the local mass flow rates. The mean concentration of the Rhodamine jet is displayed in figure 4.6. This figure shows a strong peak in concentration around the centre-line of the flow, as was expected. Figure 4.7 shows the difference in mean concentrations when they are calculated both with and without an attenuation correction. Mass flow rate values were calculated at each time step, from the instantaneous concentration and velocity fields, these were then ensemble averaged. The mean mass flow rate values were then spatially averaged along the length of the field of view to give a mean jet profile. The total mass flow rates through these profiles was found to be spatially consistent up to a maximum deviation of 5.1% from the mean value. This was radially integrated using the equation:

$$\dot{m}_{Rhodamine} = \int_0^{8D} \int_0^{2\pi} UCr \, d\theta \, dr, \tag{4.6}$$

and a total mass flow rate, as measured by PLIF, was calculated. Equation 4.6 makes the assumption that this jet is radially symmetric. Integration was between r=0 and r=8D, as at this radial distance scalar concentrations were not measurably higher than background levels. This is visible in figure 4.7.

Using equations 4.5 and 4.6, it can then be written that:

$$QC_s = \int_0^{8D} \int_0^{2\pi} UCr \, d\theta \, dr. \tag{4.7}$$

In which the assumption is made that the mass flow rate measured using PLIF (right) is equal to the mass flow rate calculated using the flow meter (left).

The mass flow rate calculated using PLIF results in equation 4.6 is $1.46*10^{-6}g/s$. This calculation is 4.1% higher than the value of $1.40*10^{-6}g/s$ calculated using the flow meter, and within the error bars of $\pm 11.59\%$. This makes the above assumption (equation 4.7) true and validates the accuracy of the PLIF technique.

The uncertainty in the location of the laser sheet was previously stated to be ± 1 mm. The uncertainty in the mass flow rate due to this was retroactively calculated. This was done by taking the corrected mass flow rate curve in figure 4.7 and extrapolating it into a three dimensional Gaussian profile. A slice of this plume was then extracted 1 mm away from the centre, and this the mass flow rate values in this slice were then used in equation 4.6 to obtain the theoretical calculated flow rate with the laser sheet misaligned by 1 mm. In this case the flow rate was calculated to be 1.7% lower. This means that in the actual case, this cause of uncertainty could mean that the measured mass flow rate was up to 1.7% lower than the value on the true centreline.

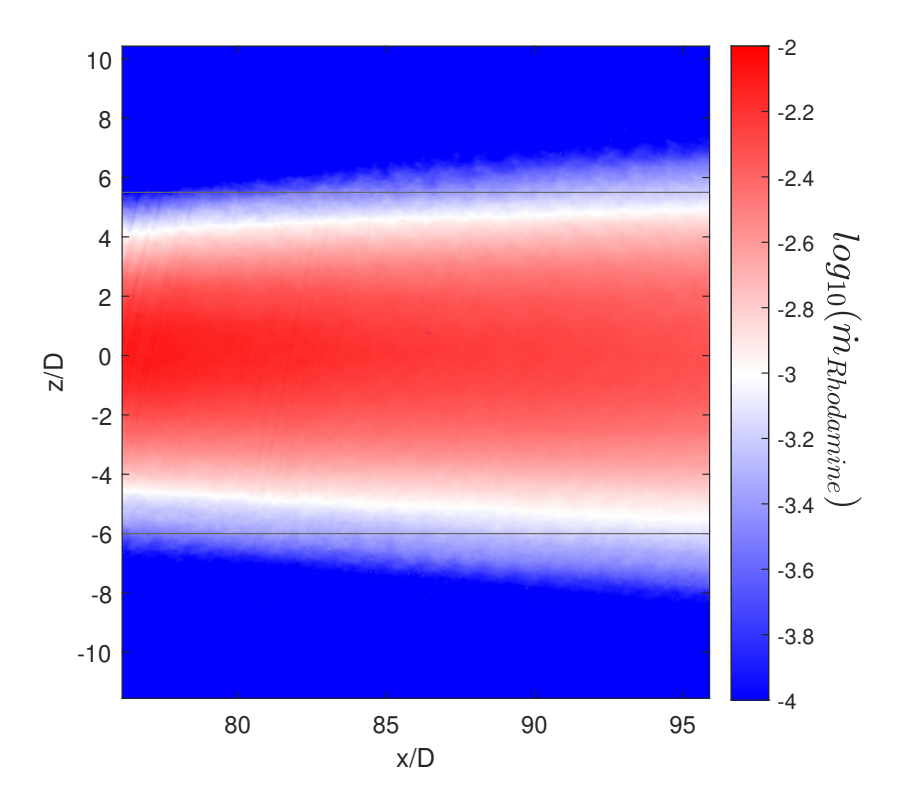


FIGURE 4.8: A full field of the mean mass flow rate calculated across the jet. The area used to calculate the absorptivity (ϵ) necessary for the attenuation correction used in figure 4.9, is shown bordered by the black lines.

Attenuation Correction 4.2.5

In the calibration that was used to acquire the results presented above, the absorptivity value of the Rhodamine solution was calculated to be 21 counts per unit concentration per meter. Without using an attenuation correction, the over-prediction goes up from 4.1% to 15.38%. This is outside the error bars of the flow meter calculation so, with no attenuation correction, the calculated flow rate could be conclusively called incorrect.

The ϵ value used in the attenuation correction which was necessary for the accuracy of the final version was calculated by plotting the mean counts measured in a calibration tank against its dye concentration, and correcting for attenuation using a variety of ϵ values. The linearity of the relationship between mean light intensity and dye concentration was then quantified. Figure 4.9 shows this relationship when using the final epsilon value calculated with this method. This process requires carrying out the attenuation correction step of the calibration process repeatedly. The mean counts value used in this process was taken only from the central section within the measurement area, in order to increase the accuracy of the ϵ calculation, this area is shown in figure 4.8 $(z/D \le \pm 6)$. A numerical routine was written in Matlab to repeatedly iterate through calibrations with different ϵ values to find the optimal one.

This is a newly developed method of calculating epsilon and has proven valuable as the epsilon value of an experiment often varies significantly. Its validity has also been

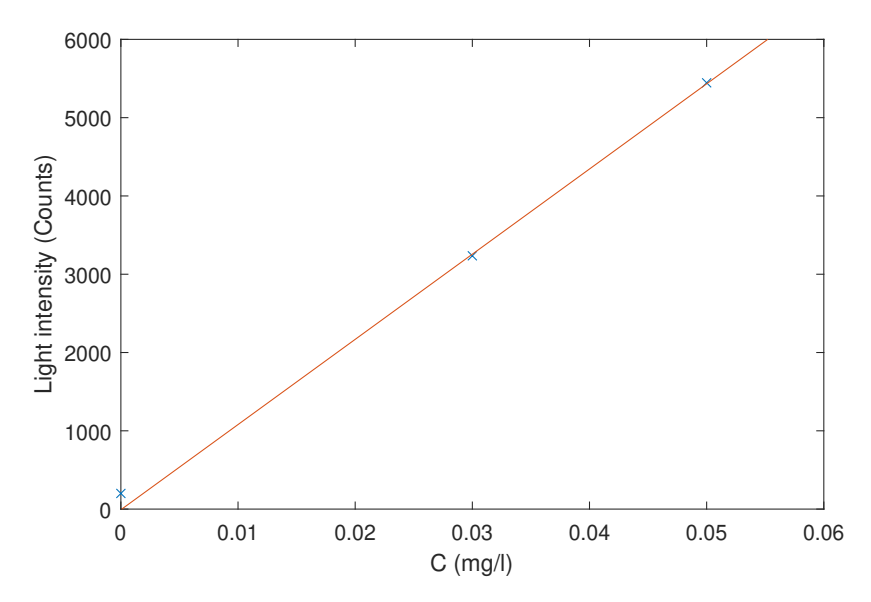


FIGURE 4.9: Light intensity measured in the calibration tanks against the concentration of the tanks, when corrected for attenuation. The linear fit is between the points at C = 0.03, C = 0.05, and the origin. The background value at C = 0.00 is included for reference

shown in that the estimated epsilon value allowed an accurate flow rate assessment.

4.2.6 Conclusion

This study has proven the accuracy of the PLIF technique in this case with an accurate attenuation correction. In this case, the PLIF measurements were used to calculate the flow rate of a jet to within the uncertainty it was measured using a flow meter. This was only possible when using an accurately calculated ϵ value for the Rhodamine solution. In the case with no attenuation correction ($\epsilon=0$) the calculated flow rate was outside the uncertainty range of the flow meter.

Chapter 5

Pollutant Dispersion Around a Single Tall Building

In this chapter the paper "Pollutant Dispersion Around a Single Tall Building" is included in full. This paper was published in Boundary-Layer Meteorology in June 2024, volume 190, article number 34. DOI:10.1007/s10546-024-00874-w (Rich and Vanderwel 2024).

An experiment was carried out using a scale model of a tall building, with the goal of investigating the role of individual buildings in the dispersion of air pollution. Pollutant dispersion around an isolated building with a height-to-length aspect ratio of 1.4 is investigated using simultaneous particle image velocimetry and planar laser induced fluorescence. Dye is released from a ground-level point source five building heights upstream of the tall building. It was found that in this case the scalar plume was dispersed laterally strongly by the building, but only slightly vertically. It is hypothesized that this is due to 94% of the plume impinging below the stagnation point on the front of the building and being drawn into the horseshoe vortex. We expect this fraction would be lower in a case in which the building is in an array of smaller buildings, and that this would lead to more vertical dispersion.

5.1 Introduction

Urban air pollution is becoming an important global problem as the proportion of the world's population living in urban environments increases. Currently this proportion is at 55% and this figure is predicted to rise to 68% by 2050 (United Nations Department of Economic and Social Affairs 2018). There is now a better understanding of how the negative health effects of living with air pollution can be severe (Dziubanek et al. 2017). The World Health Organisation estimates that in 2019, 6.7 million premature deaths were caused by air pollution and of these 4.2 million were caused by outdoor air

pollution. As a growing proportion of the world's population resides in cities and is exposed to this pollution, the importance of predicting it correctly has been emphasized.

Understanding urban airflow and how air pollution is transported is necessary for both weather forecasting and air quality forecasting. In the UK, two of the main providers of these data types respectively are the Met Office and the Department of Environment, Food, and Rural Affairs. The Met Office uses High Performance Computer (HPC) powered computational models so that they are able to output daily forecasts of weather and air quality (Met Office 2022; Bermous and Steinle 2015). The Department of Environment, Food, and Rural Affairs uses a variety of models to predict pollution, some running on HPC and some more simple ones that can be run on personal computers (Williams et al. 2011). It has also recently become necessary for new building developments within London to conduct studies into the influence they will have on the local urban micro-climate (City of London 2022).

The scalar transport equation must be solved in order to predict air pollution dispersion and this equation is given by

$$\frac{\partial C}{\partial t} + U_j \frac{\partial C}{\partial x_j} = \frac{\partial}{\partial x_j} \left(\gamma \frac{\partial C}{\partial x_j} - \overline{c' u_j'} \right). \tag{5.1}$$

Here, the C term refers to the time-averaged concentration of a flow, and the U_j term refers to the time-averaged flow velocity in the j direction. In a simulation this requires modelling of the turbulent flux term which is given by $-\overline{c'u'_j}$ in equation 5.1, due to this term being comprised of fluctuating components (Pope 2001; Arya et al. 1999). This is true for either Reynolds averaged Navier Stokes or large eddy simulations; however, in direct numerical simulations or experimental studies, this term is accurately simulated. In contrast, the advective scalar dispersion $(U_j \frac{\partial C}{\partial x_j})$ are fully resolved in all of these simulation types.

Experiments show that within an urban boundary layer this turbulent flux is often at least one order of magnitude lower than the advective flux (Talluru et al. 2018). However the direction of this flux does not necessarily agree with that of the advective flux. A previous study by our team at the University of Southampton (Lim et al. 2022) found that for a particular scalar release the turbulent flux was significant to vertical transport, but only over the rooftop shear layer of one building in the path of the plume. The gap in understanding in this previous study is how inhomogenous low level buildings contributed to this particular case.

The objective of this work is to use experiments to measure a scalar release around an isolated building in a more comprehensive manner than just center-line measurements. By comparing our findings with those of Lim et al. (2022), we aim to reveal the role of upstream buildings or lack thereof. We also quantitatively present both the turbulent and scalar fluxes in multiple cross-sections of the flow.

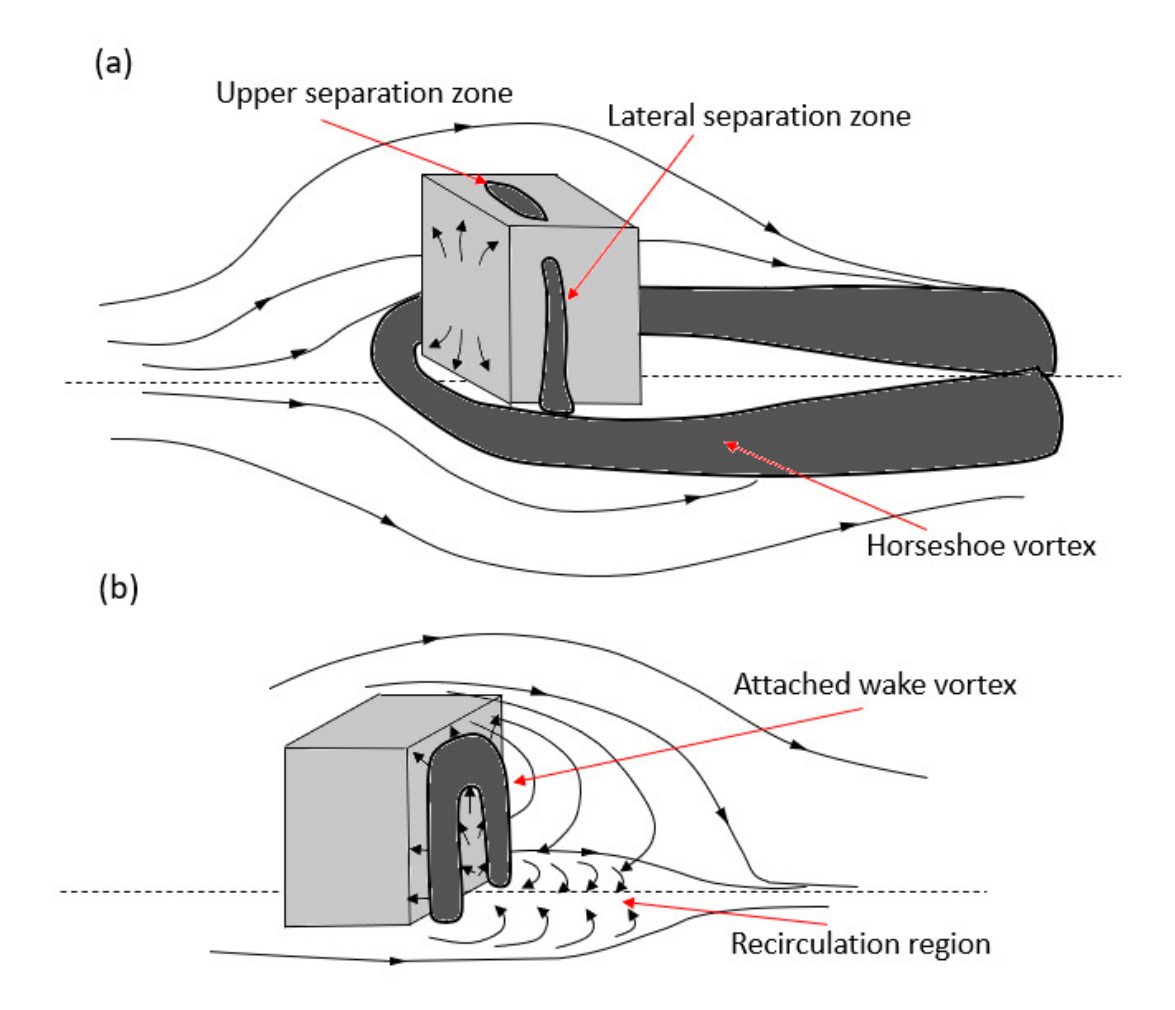


FIGURE 5.1: (a) The flow structures around the front, top, and side faces of a bluff body attached to a wall. (b) The flow structures in the wake of the same bluff body. Both figures (a) and (b) are inspired by the work of Martinuzzi and Tropea (1993).

5.2 Literature Review

Understanding flow features around buildings can be approached through the study of simplified structures, with the most simple of all being the flow around a cube. The characteristics of a fluid flow over a single cube have been previously studied (Martinuzzi and Tropea 1993; Xie et al. 2008; Hearst et al. 2016). In the diagram shown in figure 5.1a, a horseshoe vortex forms below the stagnation point ahead of the cube. The large attached vortex in the wake of the cube is shown in figure 5.1b. These two vortices are particularly significant for bluff bodies with a relatively low height-to-length aspect ratio like cubes. The small vortices visible in figure 5.1a on the top and side of the cube are also common to most bluff bodies and indicate flow separation. Castro and Robins (1977) observed that the reattachment of flow behind these vortices depends on the turbulence intensity of the flow and the ratio of boundary layer depth to cube height. Castro and Robins (1977) also found that in the wake of a wall mounted cube, the mean stream-wise velocity profile past the cube varied by only a few percent from the freestream at a downstream distance of 4.5H, and variation was below experimental

uncertainty levels of their hot-wire measurements by 8.5H. This is not to say that the flow was back to entirely free-stream conditions, turbulent statistics take longer to reform to background levels than mean flow does. In this case by Castro and Robins, reversed flow was observed to extend just slightly more than one cube height downstream.

The Commonwealth Advisory Aeronautical Research Council (CAARC) tall building model is another standardised bluff body used for investigations with a higher aspect ratio than a cube (Elshaer et al. 2016). The CAARC building's height-to-length aspect ratio is equal to 6 when aligned with its wider face to the flow. The CAARC building creates the same pattern of vortices and detached flow as a cube, however, in this higher aspect ratio case certain vortices are expanded or contracted. Braun and Awruch (2009) shows the lateral vortices shedding from the cube sides are elongated vertically in proportion to the building height. It is also shown that the vertical recirculation region detaching from the top-back edge only propagates halfway down the height of the building in this case, and extends less than one building height downstream.

Both high and low aspect ratio bluff bodies share the flow structures presented in figures 5.1a, and 5.1b. In the case of high aspect ratio buildings like the CAARC building, the lateral and cross stream sections of the rear detached vortices stretch the full height of the building (Zhao et al. 2022). The horseshoe vortex and the vertical recirculation in the rear are also proportionally weaker (Hu and Morgans 2022). In contrast to this for low aspect ratio bluff bodies such as cubes, all vortices are present but the horseshoe and vertical recalculation sections are more relevant to the flow (Castro and Robins 1977). While the influence of aspect ratio on the flow structure around the building is fairly well understood, its impact on scalar dispersion has been less thoroughly studied.

Several studies also consider a single tall building surrounded by low lying urban environment. It has been shown that the presence of one building like this can be significant to both the velocity and scalar concentration fields. Fuka et al. (2018) measured the effect of adding a single tall building with a height-to-length aspect ratio of 3 to a uniform array of low buildings, both experimentally and computationally. They took combined velocity-concentration measurements, allowing both the advective and turbulent scalar fluxes to be examined. They found that the tall building created an area in its vicinity with lower vertical transport, both advective and turbulent, but with higher lateral transport. In contrast, the low buildings by themselves created mostly negative vertical advective fluxes, at low heights, but large, positive vertical turbulent fluxes, that resulted in overall upwards vertical species transport. The flow field shows that this is in part because species in front of the tall building, at a low height, gets caught in the strong down-wash and horseshoe vortex pattern. Fuka et al also suggested a high sensitivity to the scalar source location, which is in agreement with the findings of Fackrell and Robins (1982a).

The changes in dispersion measured by Fuka et al. (2018) when changing the scalar source position can be interpreted through the flow structures into which the scalar is

being released. Fuka et al. (2018) investigated a case with the species release in the street canyon slightly ahead of the tall building and to the side, and showed a similar flow pattern to the uniform array case, aside from an asymmetric deflection away from the wake of the tall building. This appears to reveal the species being trapped in the horseshoe vortex emanating from the tall building. In a different case in which scalar was released into the wake of the tall building directly, the species became trapped in the near wake of the building within the recirculation region. This release point showed the least horizontal transport, and by far the most vertical transport. It appears that species entering this taller recirculation zone is strongly vertically transported by the rooftop shear layer; however, most species impacting the front of the building is transported horizontally away from this zone, so it mostly stays relatively clear of the species. Heist et al. (2009) shows that in the case that the scalar is released at ground level directly into the recirculation bubble, vertical transport of the scalar is significantly higher than elsewhere in the uniform array, agreeing with the latter study by Fuka et al.

In a more recent study, Lim et al. (2022) studied dispersion around a tall building with a height-to-length aspect ratio of 1.4 situated in a realistic neighbourhood of low-rise buildings using experiments and computational simulations. They found that a significant proportion of the scalar was transported above the building and spread vertically by the detached shear layer at the top of the rear vortex. They also measured the relative significance of the advective and turbulent fluxes and identified a strong correlation between the turbulent stresses and the vertical scalar transport in the upper region of the wake. This contrasts the findings of Fuka et al. (2018) and could be a result of the different surrounding building geometries and building aspect ratio in both cases.

Air-flow in urban environments often has a Reynolds number in the order of magnitude of hundreds of thousands or millions. Experimental investigations into these subjects are limited by facility size to Reynolds numbers of the order of 10,000. Fortunately it has been proven that bluff bodies become Reynolds number independent at a Reynolds number of roughly 10,000-20,000 (Castro and Robins 1977; Plate 1999). This is due to the sharp edges of bluff bodies creating fixed separation points, which are relatively insensitive to viscous effects. Therefore in an urban case in which buildings are modelled as bluff bodies, the flow structures present around these bluff bodies are insensitive to flow velocity above this region of Reynolds numbers.

The objective of this work is to investigate scalar dispersion around an isolated tall building using novel experimental techniques that provide full maps of both the turbulent and advective fluxes, and to use this data to draw conclusions about the interaction between the scalar and the flow structures. The value of this lies in the variation shown by previous studies in how a scalar is transported through the regions in which these flow structures are expected. By calculating both fluxes, a clearer picture of the components of scalar transport can be created. In addition, the building aspect ratio of 1.4 was chosen so that comparison could be made with the study by Lim et al. (2022), so that the effect of a surrounding low lying urban environment to this tall building could be investigated through its absence.

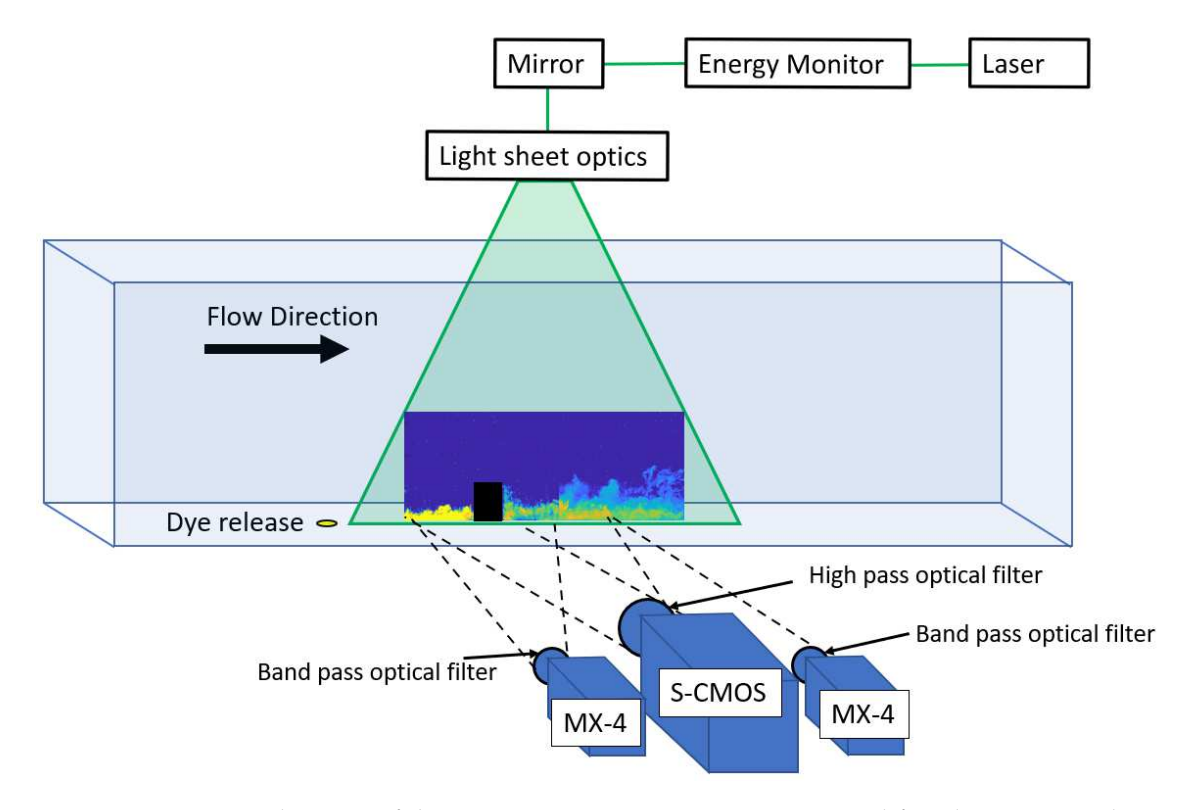


FIGURE 5.2: A diagram of the streamwise measurement setup used for planar PIV and PLIF. This three camera setup allows measurement of an area 4H tall by 7H wide (120mm by 210mm).

5.3 Methodology

This investigation was carried out in the recirculating water tunnel at the University of Southampton. This facility has a total test section length of 8 metres, width of 1.2 metres, and maximum depth of 1 metre. For all measurements the water depth was constant at 0.5 metres and the velocity was 0.55m/s. The building itself was modelled on a particularly tall building in the city section used by Lim et al. (2022), which was based on a neighborhood in Beijing. Lim et al studied this at a scale of 1:2400. It was approximated as a single square cylinder with a height of H = 30 mm and length of L = 21.4 mm, resulting in an aspect ratio of H/L = 1.4. This places it physically in between the CAARC building (Braun and Awruch 2009; Elshaer et al. 2016) with an aspect ratio of 6 and a cube with an aspect ratio of 1. The experimental Reynolds number based on the building height and the constant free-stream speed of 0.55m/s was 16, 424. This is high enough that flow around this building can be assumed to be Reynolds independent (Plate 1999; Lim et al. 2007).

Dye was released upstream of the building a distance of $x_F = 5H = 150$ mm from the front of the building, which is equal to a distance of $x_B = 5.71H = 171.4$ mm from the back of the building. This was sufficient for the plume to have dispersed a moderate amount in the boundary layer prior to impacting the building and has the additional effect of moving the interaction between the plume and the building outside the near-source region (Lim and Vanderwel 2023). Dye was used as it is a passive scalar in

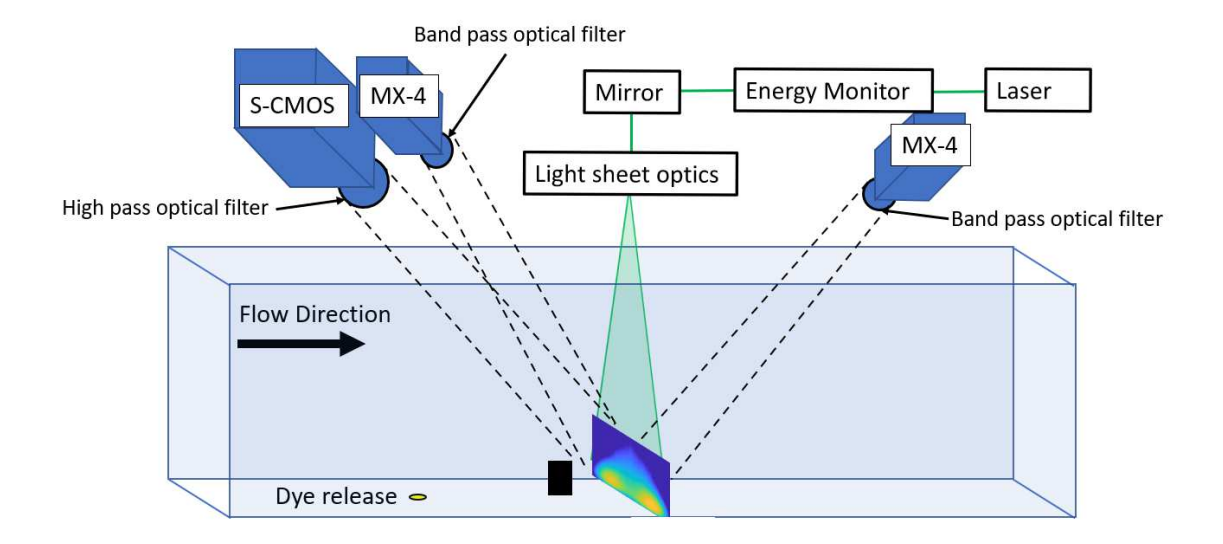


FIGURE 5.3: A diagram of the cross-stream measurement setup used for stereo PIV and PLIF. This setup allows measurement of an area 7H tall by 5H wide (210mm by 150mm).

water, and therefore it was used as a proxy for air pollution. The dye release was at a rate of $10 \, cm^3 / min$ from a point source and at a 45 degree angle to the flow. This dye injection was found to not have a measurable effect on the local flow velocity. An isokinetic ground level point source was used to reduce any influence that source characteristics might have on the experiment, as previous literature has shown that experiments on scalar plumes are highly sensitive to source conditions (Fuka et al. 2018).

Measurements were taken using coupled 2D particle image velocimetry (PIV) - planar laser induced fluorescence (PLIF) along the centre plane of the flow in the streamwise direction. The field of view extended four building heights upstream of the building and 14 building heights downstream. This required recording using a pair of side by side Lavision MX-4 cameras for PIV, along with a Lavision S-CMOS camera for PLIF. The Lavision S-CMOS was chosen for PLIF due to its 16 bit pixel depth. A calibration plate was used to align each of the cameras and we estimate any errors due to misalignment of the coordinate systems would be less than 0.1 mm. This three-camera setup was used in three different locations to create three datasets captured at different times. A diagram of the three-camera experimental setup is shown in figure 5.2.

The dye used in this study was Rhodamine 6G, which has a Schmidt number $Sc = v/D = 2500 \pm 300$ where v is the kinematic viscosity and D is the mass diffusivity (Vanderwel and Tavoularis 2014). This means that momentum diffusion is much faster than scalar diffusion. Rhodamine 6G is fluorescent and absorbs light at a wavelength of 525nm and reemits at 554nm. A Litron ND:YAG Nano pulsed laser was used as the illumination for both PIV and PLIF, which emitted at a wavelength of 532nm and an average pulse energy of 400mJ. Equipping the S-CMOS used for PLIF with a long-pass filter at 540nm filters out all laser light and allows through only remitted fluorescent light. The MX-4 cameras were equipped with band pass filters that allowed the 532nm



FIGURE 5.4: A photo taken inside the University of Southampton's recirculating water tunnel while fully drained. This photo is taken from the test section looking upstream, it shows the upstream roughness and spires used to generate an incoming atmospheric boundary layer.

laser-light through, which allowed them to measure particle displacement within the fluorescing dye plume.

Coupled Stereo PIV - PLIF measurements were also taken in cross-stream slices downstream of the building in six planes, each separated by two building heights. The first of these was 2H downstream of the back of the tall building and 7.71H downstream of the dye source. The experimental setup for this is shown in figure 5.3. For all measurements, data was collected at 10 Hz for 200 seconds, giving 2000 total PIV image pairs and PLIF images. Convention in this paper is to take the origin as the dye release unless stated otherwise, and to take downstream direction as x, cross-stream as y, and vertical as z.

A bootstrap method was used on the first and second order statistics of both the PIV and PLIF datasets using five points within the plume. For PIV it was found that the standard error in the mean streamwise velocity was 1%, and the standard error in the $\overline{u'u'}$ variance of the fluctuating velocity was 2%. For PLIF, it was found that the standard error in mean concentration was 1%, and the standard error in the variance ($\overline{c'c'}$) was 5%. This provides confidence that 2000 samples was sufficient for converged statistics.

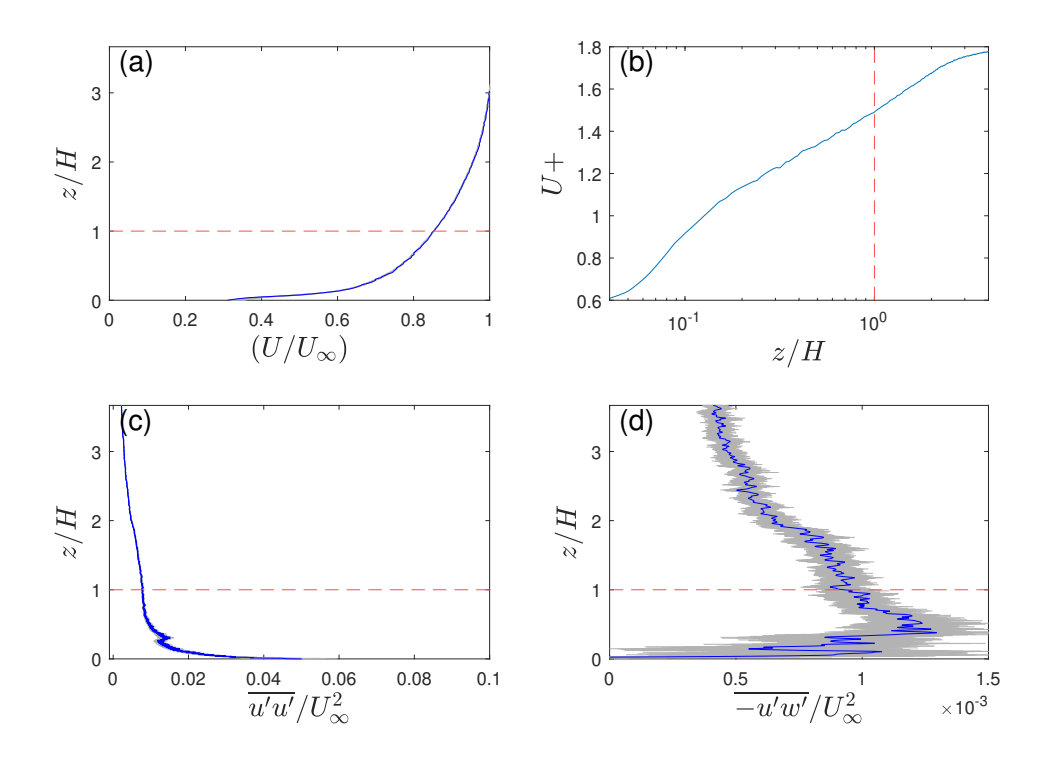


FIGURE 5.5: (a) The incoming streamwise flow velocity U/U_{∞} . (b) The incoming streamwise flow velocity normalised by the friction velocity (U^+) , plot on a semilog scale so that the log law region of the boundary layer can be observed. (c) The profile of the variance of the streamwise velocity $\overline{u'u'}/U_{\infty}^2$ of the incoming flow. (d) The profile of the Reynolds stress $\overline{-u'w'}/U_{\infty}^2$ of the incoming flow. On all plots the building height H is defined with a red dotted line. On plots (a), (c), and (d) error bars of one standard deviation are displayed in grey representing the uncertainty in the region of the incoming flow that was averaged in the streamwise direction.

In turbulent flows it becomes necessary to take measurements with a range of dye concentrations in order to maintain a good signal to noise ratio. The measured local concentrations are normalised by the source concentration. This is valid if the locally measured concentration is within the linear response regime (ie. $< 0.6 \, \text{mg/L}$). The source concentration was chosen to obtain the maximum concentration in the field of view, which did not overexpose the camera. In some cases where the species concentration varies by more than an order of magnitude within one field of view, such as near the source, multiple measurements with varying source concentrations were stitched together. The dye source concentrations used in this study varied from 1 mg/L to 60 mg/L.

Urban environments currently always exist within an atmospheric boundary layer. Therefore in order to experimentally model an urban environment with any accuracy, an atmospheric boundary layer must also be modelled. This can be done through the use of uniform roughness elements and larger spire structures (Tomas et al. 2017). In this experiment, the atmospheric boundary layer was modelled using the flow conditioning shown in figure 5.4. This roughness is comprised of spires followed by descending sizes of roughness elements, from $2cm^2$ to $1cm^2$ then to $0.5cm^2$.

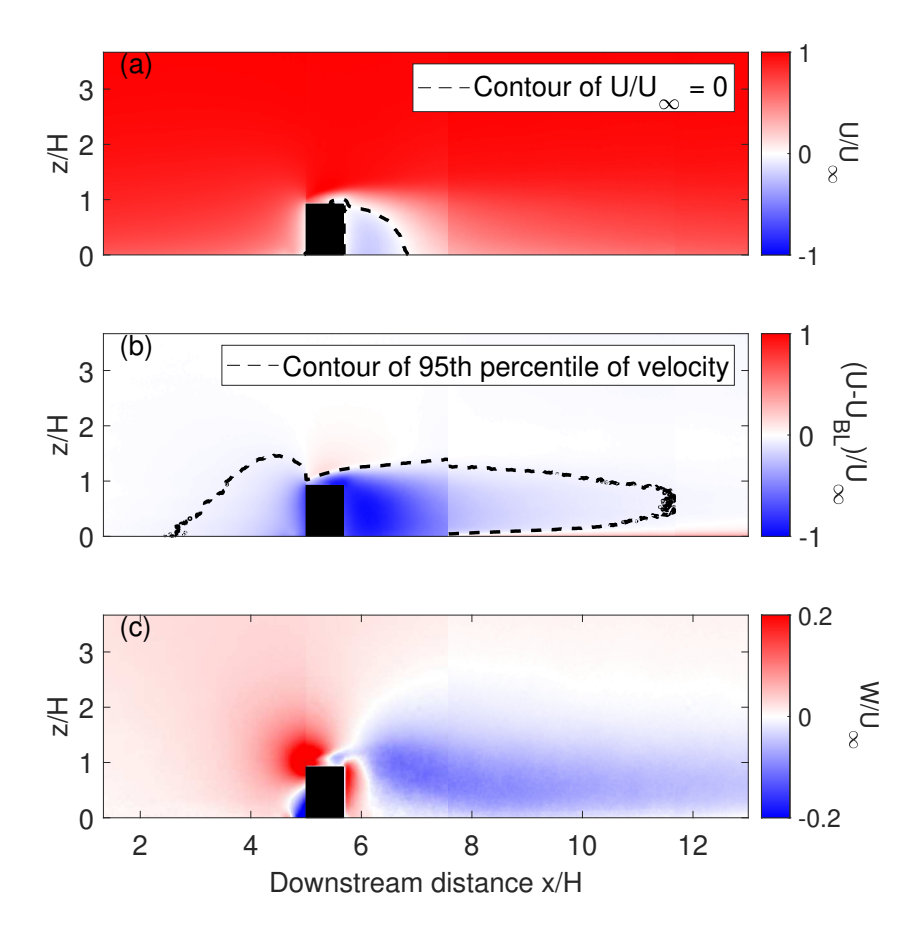


FIGURE 5.6: (a) The extent of the recirculation region in the wake of the tall building, defined as a contour of zero streamwise velocity. Contour is on a plot of normalised streamwise velocity (U/U_{∞}). (b) The velocity deficit ($U-U_{BL}$)/ U_{∞} in the wake of the tall building. The extent of this region is defined as a contour of $U=0.95*U_{BL}$. (c) The normalised vertical velocity (W/U_{∞}) in the vicinity of the tall building.

The boundary layer formed for this experiment had a depth at the test section of 103mm and varied less than 2% within the field of view. Details of the freestream flow characteristics are shown in figure 5.5. With the building height of 30mm this boundary layer depth is sufficient to keep the building height within the log-law region of the boundary layer. The log law region is visible in figure 5.5b which presents the velocity profile scaled by wall units. This is significant as this is true for a realistic city case. Using the peak of the Reynolds shear stress to calculate the friction velocity gives a value of $(0.019 \pm 0.001)ms^{-1}$, and a friction Reynolds number $Re_{\tau} = 1500$.

5.4. Results 65

5.4 Results

5.4.1 Centre-plane measurements

5.4.1.1 Mean Velocity Fields

Figure 5.6 shows PIV mean field characteristics from the planar PIV dataset along the center-line of the building. Figure 5.6a shows the mean streamwise velocity $\frac{U}{U_{\infty}}$, close to the tall building. A decrease in velocity in the vicinity of the building is apparent, with this effect continuing much further downstream than upstream. In this figure, the recirculation region is defined by a contour of $\frac{U}{U_{\infty}} = 0$. This can be seen in the immediate wake attached to the back of the building. The wake recirculation is mostly contained to within 1H of the trailing edge of the building and has entirely disappeared by 1.4H.

The velocity deficit created by the building is defined as the difference in the local mean flow velocity compared with that measured in the absence of the building, ie. $U - U_{BL}$, where U_{BL} (boundary-layer) is the U value at that point in the boundary layer without the building present. The extent of the region with significant velocity deficit is defined as the contour of $U = 0.95U_{BL}$. Figure 5.6b shows the extent of the velocity deficit left by the tall building. It extends 7.3H downstream of the building, or 221 mm. This is consistent with the findings of Castro and Robins (1977) studies of flow around a wall mounted cube.

Figure 5.6c is a plot of the mean vertical velocity W/U_{∞} . The general pattern shows mostly positive values ahead of the building and mostly negative values in its wake. The flow impinging on the front of the building has a vertical stagnation point on this leading face. Below this point, the mean flow is travelling in the y direction around either side of the building. The large down-wash region in the wake is at a low magnitude but only diminishes in strength slowly and continues into the far-field.

In the case of the CAARC building the recirculation region at ground level extends less than 0.4H downstream of the building (Zhao et al. 2022), this length is far lower than the value observed in figure 5.6. This bluff body flow around the isolated building can be likened more easily to the studies of isolated cubes, as done by Castro and Robins (1977), than to studies on the CAARC building (Braun and Awruch 2009; Zhao et al. 2022).

5.4.1.2 Turbulence Statistics

Figure 5.7 shows the $\overline{u'w'}$ Reynolds stress component, which is important in the generation of turbulent kinetic energy. This component gives a clear picture of a strong rooftop shear layer, very similar to the one observed by Lim et al. (2022). This $\overline{u'w'}$ shear layer is almost entirely negative, apart from at the leading edge, implying the anti-correlation of the two fluctuating components as expected in a turbulent shear flow. This layer does not significantly spread much further upwards from its starting height

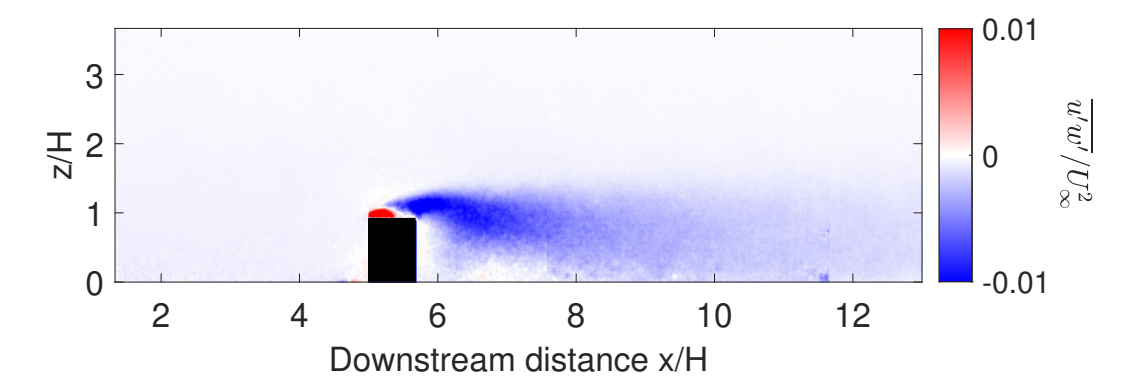


FIGURE 5.7: The $\overline{u'w'}$ Reynolds Stress component around the tall building.

above the building, and instead it spreads downwards into the wake behind the building. The recirculation region in the close wake has relatively low Reynolds stress relative to the velocity deficit region.

5.4.1.3 Species Mean and Variance

An example of the instantaneous concentration field is given in figure 5.8a, which exhibits the high intermittency shown by this plume. This contributes to the low mean concentration values measured far downstream of the building, these are shown in figure 5.8b. The intensity of the dye visible in the instantaneous field is also much higher than the mean values measured. In figure 5.8b, it is also visible that the edge of the plume is driven upwards by the presence of the tall building and continues to expand vertically in the wake of the building.

Figure 5.8c shows the variance of the concentration in the wake of the tall building. This graph follows the shape of the mean concentration in figure 5.8 b. This was also observed in measurements of an unbounded plume in shear flow by Vanderwel and Tavoularis (2014).

The reducing noise in the background of figure 5.8b and c can be attributed to the increasing dye source concentration. Source concentration was increased from 5mg/l for the measurements around the building to 60mg/l for downstream. Noise in PLIF measurements often takes the form of laser streaks that are artifacts of the concentration calibration process (Baj et al. 2016).

5.4.1.4 Scalar Flux Measurements

Figure 5.9 shows the vertical turbulent and advective fluxes across the centerplane of the flow in the vicinity of the tall building. These fluxes are defined as $\overline{c'w'}$, and CW respectively, in which c is the scalar concentration and w is the vertical velocity

5.4. Results 67

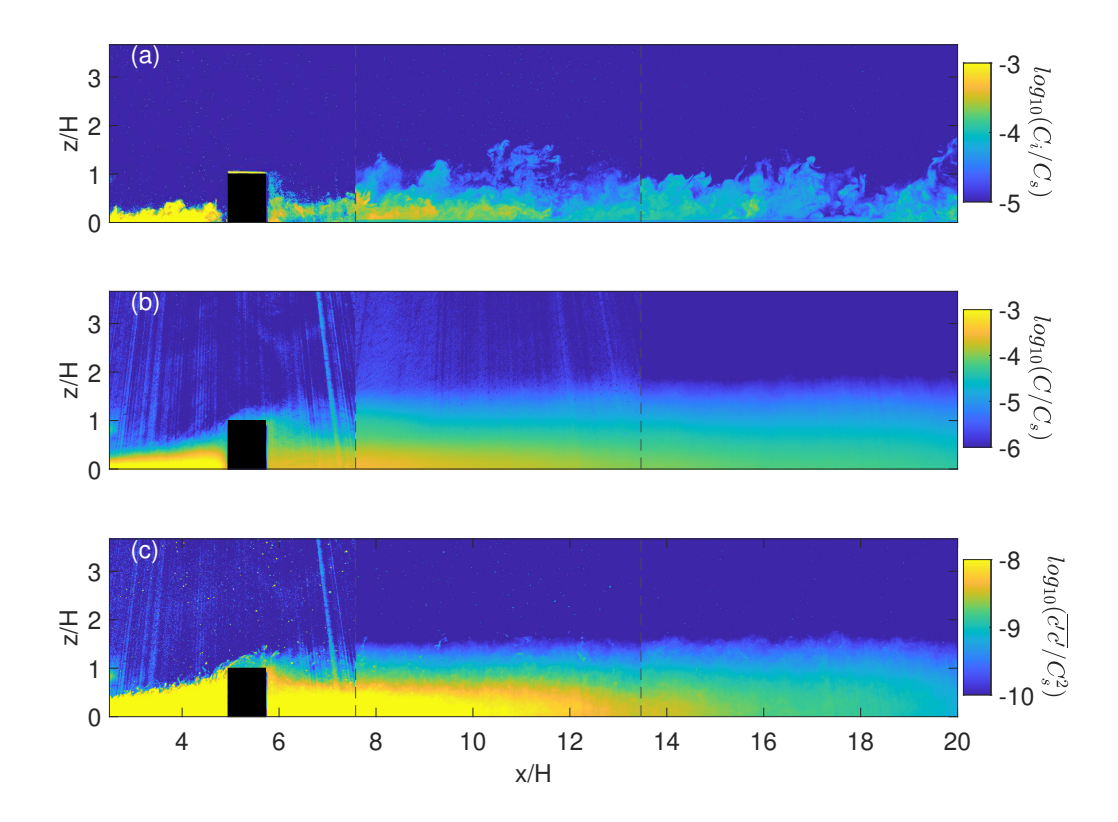


FIGURE 5.8: (a) Three instantaneous slices of species concentration near the tall building on a log_{10} scale, normalised by the source concentration; the three slices were taken at different times and were later stitched together. (b) The mean species concentration around the tall building on a log_{10} scale, normalised by the source concentration. (c) The species variance, also normalised by source concentration and shown on a log_{10} scale. In all three figures dotted lines represent the lines along which different datasets have been stitched together.

component. As scalar concentration values are necessarily positive, the sign of the advective flux field purely corresponds to whether the mean vertical velocity at that point is upwards or downwards. Both turbulent and advective fluxes are extremely low or absent over the top of the tall building, relative to the plume in front of the building. Both scalar fluxes then increase again further in the wake. This is visually exaggerated in figures 5.9a and b, due to the second field of view starting and the signal to noise ratio dramatically improving. The turbulent flux is almost entirely positive, aside from a few points before the tall building, indicating the average effect of turbulence is almost always causing an upwards dispersion of the species, even when the overall flow direction is downwards.

The two figures 5.9a and b are displayed on the same colormap and show values of a similar order of magnitude. In almost all locations, the magnitude of the advective flux is slightly greater than the turbulent flux. These results are similar in magnitude and sign to those measured by Lim et al. (2022), the main difference being that the turbulent flux was found to be slightly higher in this isolated building case.

Due to Reynolds analogy, we might expect that locations of high Reynolds stress (ie. turbulent transport of momentum) will also be areas of high vertical turbulent scalar

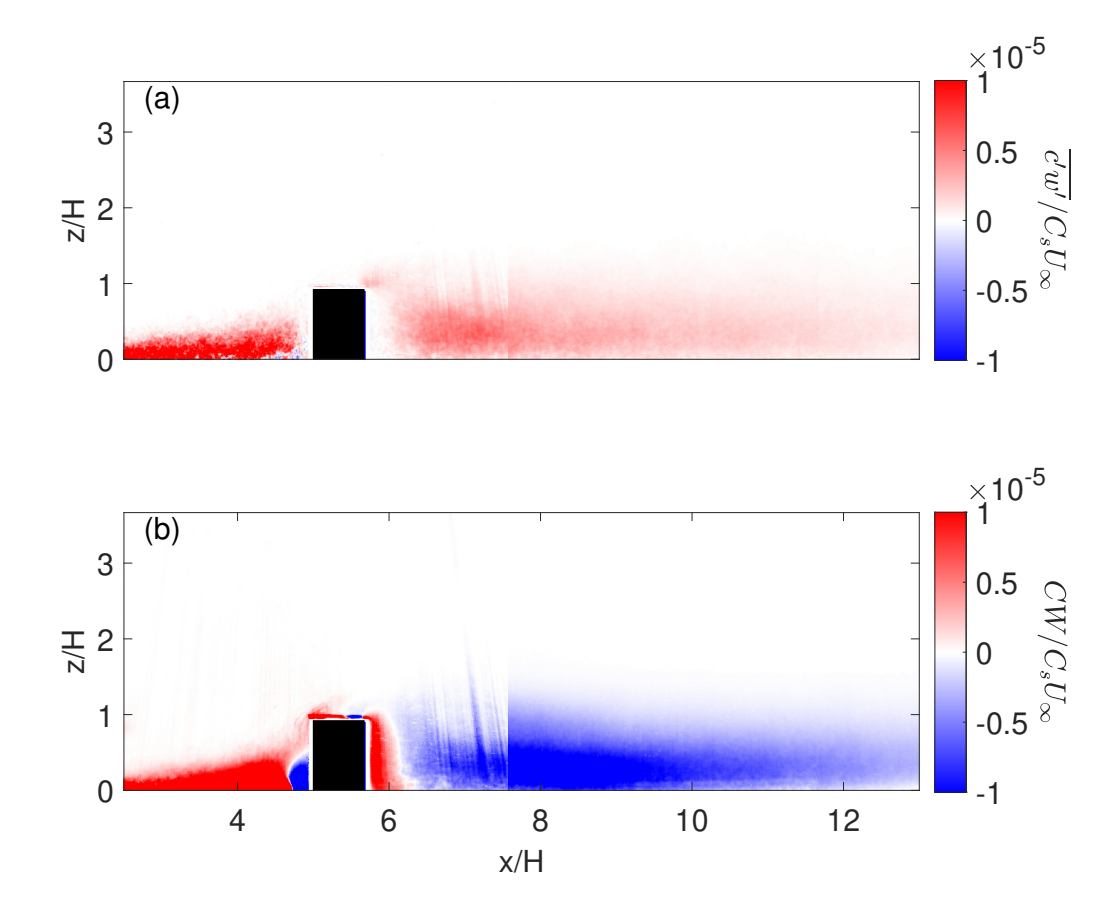


FIGURE 5.9: (a) The vertical turbulent flux field $(\overline{c'w'}/C_sU_\infty)$. (b) The vertical advective flux field (CW/C_sU_∞) .

flux (ie. turbulent transport of scalar) (Vanderwel and Tavoularis 2016). However, figure 5.7 shows a high Reynolds stress region above the top of the tall building which does not correlate to a high turbulent scalar flux in the same place in figure 5.9a. This lack of correlation must be due to very little scalar reaching this region. In figure 5.8b it can be seen that the mean concentration above the tall building has dropped multiple orders of magnitude relative to the scalar concentration near the ground, both ahead of and behind the building.

The lack of a region of high turbulent scalar flux above the building in figure 5.9a does not agree with the findings of Lim et al. (2022), which is interesting as both studies use the same building model. Instead Lim et al. (2022) found that while the mean scalar concentration was lower near the ground, it spread significantly above building height. The two differences between these studies are the absence of surrounding buildings in the case presented in this paper, and the distance from the scalar source to the tall building, which is 4H in the case presented by Lim et al. (2022) and 5H in this case. Lim et al. (2022) shows the scalar plume impinging higher on the tall building than it does in figure 5.8b. This implies that the scalar plume grows faster in the case with surrounding buildings to create low level turbulence despite the lower distance between the building and the plume source. The case presented in this paper only shows the plume reaching the height of the rooftop shear layer when the plume has already passed the building,

5.4. Results 69

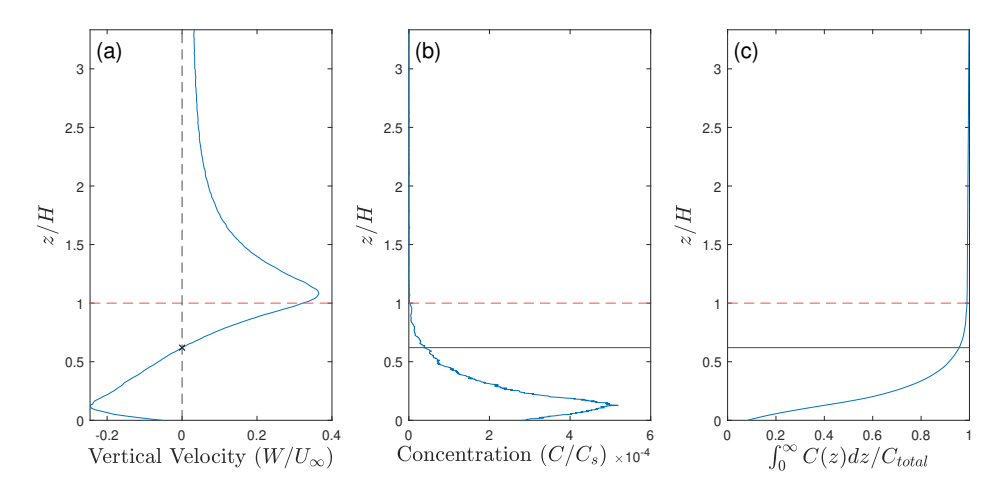


FIGURE 5.10: (a) The mean vertical velocity W (m/s) at the closest PIV measurement to the front of the tall building (x/H = 4.98), showing the stagnation point (marked with an X) across this leading face is at z/H = 0.62. (b) The concentration profile at the same x location as this PIV measurement, normalised by source concentration. (c) The cumulative total of the concentration profile shown in (b), normalised by the sum of this profile.

whereas in the case studied by Lim et al. (2022) the upper edge of it reaches this level before the building.

Figure 5.10a is a profile of vertical velocity taken immediately ahead of the tall building with the stagnation point and height of the building highlighted. This figure shows that ahead of the tall building vertical velocity is negative up until 62% of the height of the tall building. Integrating the concentration profile shown in figure 5.10b up to this stagnation point and dividing by the total concentration in this profile shows just 6% of the total dye when summed vertically, passes above the stagnation point, with 94% passing below. This process has been illustrated using figure 5.10c. As the advective flux direction always follows that of the mean velocity, and the turbulent flux is generally smaller than the advective flux, the mechanisms transporting dye upwards from this point are minimal. Figure 5.9 particularly shows that the leading face of the tall building has a very low level of turbulent flux. This means that all scalar impacting below the stagnation point has very little possibility of passing above the building. It needs to already be above this level by the time it reaches the building. This lack of transport to the shear layer can possibly explain the lack of presence of any influence from the shear layer in figure 5.9a.

5.4.2 Cross-stream measurements

5.4.2.1 Mean Velocity

Figure 5.11a shows the variation in streamwise (U) velocity across the span as measured with the cross-stream stereo PIV. The velocity profiles were extracted at z/H = 0.5. These profiles show the velocity deficit in the wake of the tall building diminishing with

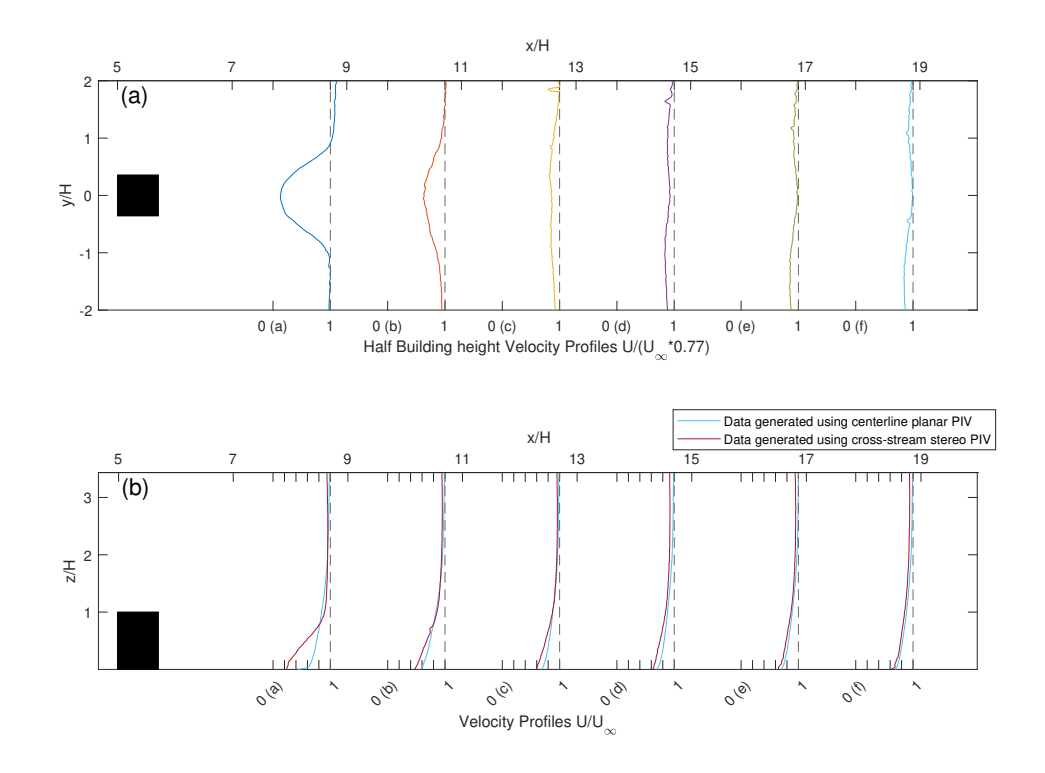


FIGURE 5.11: (a) Cross-stream slices of mean streamwise velocity normalised by the local freestream velocity, this being $0.77*U_{\infty}$, as calculated using data shown in figure 5.5. (b) A comparison of the stereo and planar PIV results at each downstream distance in which stereo data was aquired. Data from planar PIV is shown in light blue, data from stereo PIV is shown in dark red.

both downstream and cross-stream distance, and agree with figure 5.6. There is a small asymmetry visible in figure 5.11a and this could be caused by either a small laser sheet misalignment or a small building misalignment with the flow. We can define the distance behind the building as $x - x_B$. This figure shows that beyond $x - x_B = 8H$ (x = 13.71H from source) the flow cross section does not continue to change in a noticeable way.

Figure 5.11b compares vertical profiles of the streamwise velocity at the same points from both the streamwise 2D PIV and the Stereo-PIV measurements. The measurements agree well with the exception of those obtained at 2H downstream of the tall building $(x - x_B = 2H \text{ or } x = 7.71H)$. At this distance, the stereo data shows the most significant change in boundary layer shape from an undisturbed boundary layer. The location is not surprising as this is in a region which is extremely strongly impacted by the velocity deficit. This discrepancy is mostly below z/H = 0.5, at the $x - x_B = 2H$ measurement, and it is therefore possible that at this height the laser sheet is introducing uncertainty through reflections off the nearby tall building. This uncertainty being greater is due to the Stereo-PIV experimental setup having the cameras aligned with the out of plane tall building, as shown in figure 5.3. Aside from this measurement the two data sets agree well about the diminishing of the velocity deficit.

5.4. Results 71

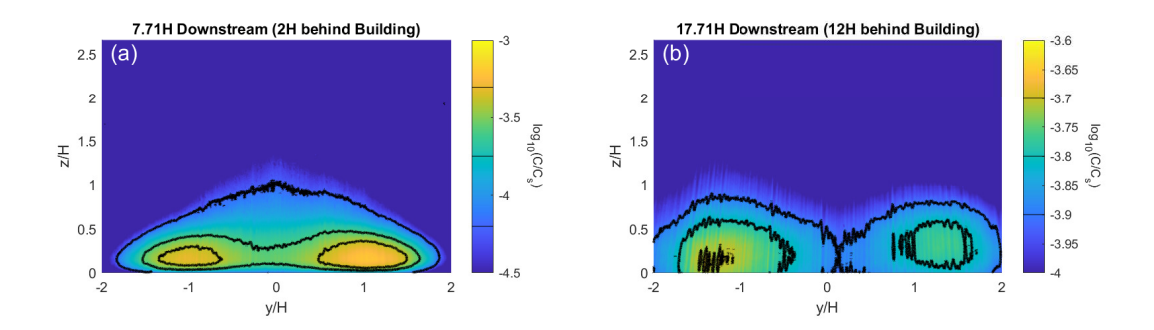


FIGURE 5.12: Species concentration downstream of the tall building on a log_{10} scale, normalised by source concentration. The values of contour lines are displayed on the colour bars of each figure. Downstream distances shown in (a) and (b) are equal to $x - x_B = 2H$ and $x - x_B = 12H$. Only these two slices were shown for the sake of clarity, the other four are positioned in-between these two and do not reveal anything different to the relationship visible in these two. The two figures are not shown on the same colour map due to the intensity in scalar measured varying significantly between the two planes.

5.4.2.2 Cross-stream concentration measurements

The cross-stream PLIF measurements shown in figure 5.12 show cross-sections of the mean dye concentration at $x - x_B = 2H$ and $x - x_B = 12H$ as the dye plume propagates downstream from the tall building. This figure reveals that the shape of the dye plume has a double peak shape in the wake of the building. The strongest concentration of dye is detected near the ground, but offset to either side of the building. This effect is then less pronounced downstream at $x - x_B = 12H$, however it is still visible. This implies very limited spanwise motion of the species in the far wake. This limited spanwise motion agrees with the measurements of Fuka et al. (2018) when the scalar release is aligned with the front of a tall building.

Figure 5.12 shows that the highest areas of species concentration are outside the center plane of the flow, once the plume has propagated downstream of the tall building. Most of the species remains trapped close to the floor on either side of the building and then begins to disperse more evenly much further downstream. Comparing this with the understood mechanisms of bluff body aerodynamics (Castro and Robins 1977), it seems that the species is trapped in the horseshoe vortex formed from the base of the bluff body. This horseshoe vortex and bluff body flow structures have been depicted in figure 5.1. The dual-peak plume shape visible in figure 5.12 has not decayed fully as far as $x - x_B = 12H$ downstream of the tall building, implying that an assumption of Gaussian scalar distribution is not accurate until at least beyond this point. Despite the dual plume shape still being visible, it is less distinct at $x - x_B = 12H$. It is presumed that far enough away from the tall building the plume would fully recombine for Gaussian plume theory to be valid.

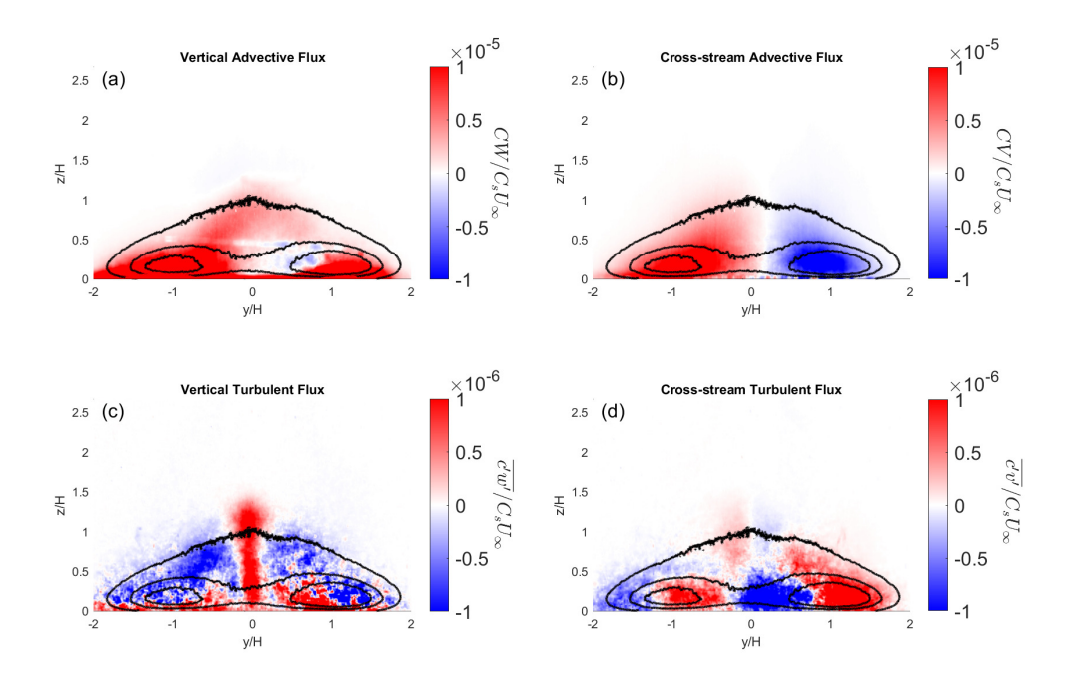


FIGURE 5.13: (a) The Vertical Advective flux field (CW/C_sU_∞) . (b) The Horizontal Advective flux field (CV/C_sU_∞) . (c) The Vertical Turbulent flux field $(\overline{c'w'}/C_sU_\infty)$. (d) The Horizontal Turbulent flux field $(\overline{c'v'}/C_sU_\infty)$. All plots are taken from $x-x_B=2H$ downstream of the tall building, or x=7.71 downstream of the dye source. All have contours of mean concentration superimposed for clarity, the values of these contours are visible in figure 5.12a.

5.4.2.3 Turbulent and Advective Structures

The vertical advective flux field shown in figure 5.13a shows an upwards motion of the dye throughout most of this slice of the wake of the tall building. This is only present in this slice at $x - x_B = 2H$ and further downstream of the tall building, this flux becomes consistently negative on the center-line. This slice does not agree with the data displayed in figure 5.9b but all other advective fields do agree. The positive vertical advective regions offset from the center in figure 5.13d show a high magnitude and appear to be significant to the development of the plume shape. Figure 5.13b reveals an overall converging motion of the plume towards the center-line. The region with strong advective flux stays relatively close to the tunnel floor and with the greatest height at which advective flux is measured being on the center-line. However this region barely rises above the building height.

The vertical turbulent flux shown in figure 5.13c agrees with figure 5.9a. However it also reveals that this positive turbulent flux in the wake of the building is localised to the center-line of the flow and not a generally applicable rule to the whole wake. In fact, it is shown that for this wake, the opposite is true and turbulent flux is negative in most places. The center-line vertical transport does not just agree in sign with the planar results, it also agrees accurately in magnitude, which is gratifying given the difficulties in calculating turbulent fluxes from stereo PIV data. Fuka et al. (2018) observed a

5.4. Results 73

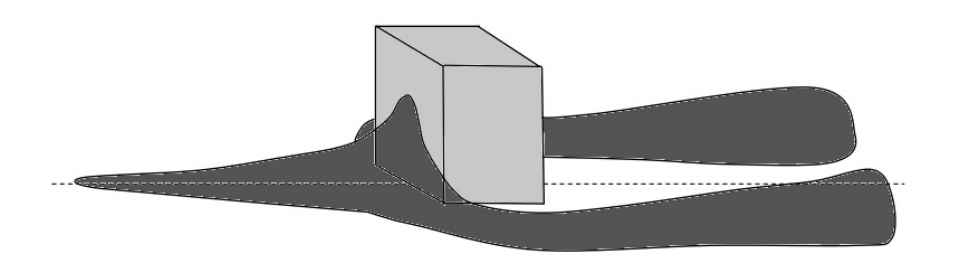


FIGURE 5.14: A diagram of the regions of highest dye concentration, based on the data from both experimental setups. This is intended as a qualitative figure to show the observed effect that the plume is impinging below the building stagnation, and then being trapped in the horseshoe vortex.

consistently positive vertical turbulent flux, which is in contrast to the changing signs revealed in figure 5.13b.

The horizontal turbulent fluxes given in figure 5.13d reveal structures alternating in sign that align closely with the overlaid isocontours of mean concentration. These structures show turbulent horizontal fluxes with signs pointing away from the two points of highest mean concentration. These structures do not extend above 0.5H.

5.4.3 Discussion

The hypothesised 3D shape of the highest concentration area of the dye plume is shown in figure 5.14. The downward velocity measured in figure 5.6 represents the extent to which the high concentration area of the species plume extends vertically on the front face of the tall building. It is visible in figures 5.9a and b that both the advective and turbulent vertical scalar fluxes are very low above the tall building, despite the high Reynolds stress being measured in figure 5.7. The low species concentration in the immediate wake is supported by the measurements of Fuka et al. (2018) who observed little cross-stream scalar transport between the horseshoe vortex and the recirculation region of a tall building.

It is presumed that the centerline region is that which is affected by the rooftop shear layer and detached flow at the top of the back of the building. This is based on an extrapolation of the established bluff body flow structures depicted in figure 5.1. However in this experimental case, this region has had a less significant influence on dispersive behavior than in some previous studies (Lim et al. 2022). The diagram given in figure 5.14 essentially reflects a transition from a ground-source plume to the leading edge horseshoe vortex shape trailing behind a bluff body. This diagram differs heavily

to the diagram showing all flow structures (figure 5.1) as only the horseshoe vortex was proven to be relevant to dispersion in this particular case. The scalar species becoming trapped in the horseshoe vortex was also measured by Fuka et al. (2018); however, in that case the scalar was released directly into the front of the horseshoe vortex. With how low lying the scalar plume was shown to be in figure 5.8b, it is not surprising that this paper measured a similar pattern of low vertical transport to Fuka et al. (2018).

We can speculate how concentration transport would vary for buildings of different aspect ratios by considering the roles of the horseshoe vortex and the stagnation point. Figure 5.14 is based on the measurements around a square-cylinder with aspect ratio 1.4 that were done in this study. In the case of a higher aspect ratio building such as the CAARC building, we would expect that less of the scalar will be trapped in the horseshoe vortex due to it being a relatively smaller flow structure. Instead the lateral separation zone (see figure 5.1) would become larger and transport more of the scalar. In the case of a lower aspect ratio structure like a cube, the horseshoe vortex would become stronger again and would be expected to trap an even higher proportion of the dye.

For both speculated examples above the assumption is made that the scalar plume impinges at a similar height relative to the stagnation point. This is because if the plume impinges above the stagnation point then much more of the scalar will enter the recirculation region or wake vortex instead of the horseshoe vortex. The impingement height of the scalar would depend on the position and elevation of the source and how much it has spread before reaching the building. We have also learned that the surrounding geometry also influences the distribution of the concentration reaching the building.

5.5 Conclusions

The flow structures around a single tall building have been examined using the PIV and PLIF techniques in both streamwise and cross-stream slices. Data has been analysed and compared with existing literature as validation. Vertical scalar fluxes were calculated on the centre plane to compare the components of vertical scalar dispersion. It was found that along the centerplane of the wake, the advective flux stayed negative into the far field, whereas the turbulent flux was smaller but positive, shown in figures 5.9 and 5.13.

3D analysis of the scalar plume around this building showed a distinct dual peak shape, with a trough along the centerplane of the flow, visible in figure 5.12. This shape was still measurable at the furthest cross stream measurements, 12H downstream of the tall building.

Comparison with scalar flux measurements by Lim et al. (2022) show that while rooftop shear layer turbulent flux dominated dispersion in that case, it contributed close to nothing in the case studied in this paper. This is hypothesised to be because, without the surrounding buildings creating near wall turbulence, the scalar was not transported into

5.5. Conclusions 75

the rooftop shear layer. We showed that overwhelmingly the turbulent flux has an upwards direction. Therefore it can be implied that the lower level of turbulent flux before the building contributes towards the lower plume height when it reaches building. This low plume height then causes the majority of the scalar to become trapped in the horseshoe vortex forming around the base of the tall building.

In summary, the centre plane alone was not sufficient to explain the plume's interactions with flow structures in the wake of the tall building. It is important when studying these structures experimentally to also measure at an offset from the center-plane. Similarly advective fluxes are insufficient to fully explain the plume dispersion. We showed (figure 5.9) that turbulent fluxes are of the same order of magnitude as advective fluxes, and that (figure 5.13) the turbulent fluxes switch direction in more localised patterns than the advective fluxes do. If turbulent fluxes are being modelled in computational simulation then it is important that these inhomogenities are captured accurately.

Chapter 6

Scale-model Experiments of Turbulent Dispersion over a Realistic Urban Environment

This chapter presents the Southampton city study which was the primary focus of this PhD. This paper is intended for submission to Building and Environment once a collaborator has provided LES data for comparison. This chapter follows the structure of a journal article which has been included, except for its introduction section. This omission is to avoid repetition of earlier content in this thesis.

As stated in chapter 2, there have been very few studies in which quantitative measurements of the turbulent scalar flux terms have been acquired over an urban environment. Out of these studies none have acquired full fields of data and also incorporated a realistic atmospheric boundary layer. This chapter builds upon the work of chapter 5 by studying the transport of a scalar plume in the context of a realistic city, as opposed to in an isolated case. As such, chapter 5 is a useful comparison to understand the effect of the realistic model. This study was carried out with the aim to fill the gap in understanding of dispersive fluxes in realistic cities. In this chapter, analysis is also carried out to asses the validity of the Gaussian plume model in predicting the measured plume. This has been carried out due to the current widespread use of Gaussian plume-based models.

This investigation aims to experimentally measure the turbulent processes involved in scalar transport in an urban flow. To model urban air pollution dispersion accurately, it is necessary to have an in-depth understanding of these turbulent process. Experimentally measuring these processes requires simultaneous measurements of both the instantaneous concentration and velocity. This investigation provides this data. This realistic case study focuses on the city of Southampton, which is a medium sized port city in the South of England. A 1 km² section of Southampton's city centre was 3D printed at a scale of 1000:1. A ground level point source was introduced upstream to simulate port emissions. Planar laser induced fluorescence (PLIF) and particle image

velocimetry (PIV) were used to acquire full fields of simultaneous concentration and velocity data. These fields were used to calculate the turbulent and advective fluxes above the model. In addition to turbulent transport, this dataset was also used to analyse characteristics of the scalar plume emitted from the point source.

6.1 Literature Review

6.1.1 Experimental Urban Cases

Measuring the concentration of a scalar in a fluid flow is possible in several different ways, but the methods available have various advantages and disadvantages. In wind tunnels, the most common methods are to use a fast flame ionisation detector (FFID) (Carpentieri et al. 2012) or photo-ionisation detector (PID) (Talluru et al. 2018). Both of these methods use a probe to obtain high frequency data at a single point. In water tunnel experiments, it is possible to use the planar laser induced fluorescence (PLIF) technique. This is an optical technique that uses a camera to non-intrusively measure the fluorescent response of a dye under a laser sheet, and calibrate this dye response to known concentration values.

Very few experiments have measured both scalar concentration and velocity over a realistic city model, meaning there are very few existing datasets on this subject. More experimental studies have been carried out on idealised urban roughness or fully random roughness (Fuka et al. 2018) due to the more generalisable nature of it. Idealised roughness can provide useful insight and even be somewhat realistic in particularly ordered cities, such as Barcelona. However; in most cases, real cities are built with a significant amount of structural inhomogeneity. This results in certain neighbourhood scale structures existing, such as long street canyons, but often with little alignment from one street canyon to the next.

The experiments that have been carried out on realistic city models are mostly done in wind tunnels (Ono and Nozu 2024; European Cooperation in Science and Technology 2015). The datasets gathered in these facilities are mostly limited to point measurements and can struggle when used to attempt to resolve fluxes around the highly heterogeneous roughness that is found in realistic cities. Field work has been carried out extensively, but is also largely limited to point measurements. However, recently there has been some use of Lidar systems to measure full profiles of field data in urban environments (Samad et al. 2023). A more detailed literature review on field work has been given in chapter 2

It was shown by Xie et al. (2008) that increasing the variation in the height of roughness elements in an urban like array increases the effective friction coefficient. It was also shown by Vanderwel and Ganapathisubramani (2019) that randomising the position of roughness elements increases the friction coefficient when compared with a regular

array aligned to the flow in street canyons. In a fully realistic city model there will be both variation in height (Xie et al. 2008), and variation in alignment to the flow direction (Vanderwel and Ganapathisubramani 2019). Both variations will depend on the specific city and wind direction, however it is safe to assume that a realistic city will influence a flow differently to an idealised array. Additionally, the conclusions of Xie et al. (2008) and Vanderwel and Ganapathisubramani (2019) would imply that the realistic city will have a higher velocity deficit than a similar regular array would, affecting the local flow.

In urban arrays, scalar plumes are highly sensitive to source location Fuka et al. (2018). However, in nearly all cases they form a Gaussian distribution following the mean flow direction (Carpentieri et al. 2004). It was shown by Marucci and Carpentieri (2020) that an idealised array misaligned with a flow can cause a plume to deviate in angle from the mean flow direction. In this case the plume still followed the shape of a Gaussian distribution. There are some cases in which a single large building has caused a plume to spread in a non Gaussian way for a significant distance (Fuka et al. 2018; Rich and Vanderwel 2024). However, it is a minority of cases in which a plume does not spread in a Gaussian shape; this characteristic seems to be relatively robust to flow conditions.

The current state of the art technique in modelling pollutant dispersion is the Gaussian plume model. This model is the basis of the ADMS software package (Cambridge Environmental Research Consultants 2023), the ALOHA software package (U.S. National Oceanic and Atmospheric Administration 2013), the TSCREEN software package (U.S. Environmental Protection Agency 2021), and is how dispersion is modelled within the Aeromod simulation software (U.S. Environmental Protection Agency 2004). Out of these packages, ALOHA and ADMS are typically used as fast response models, while AEROMOD is a meteorological simulation software, and TSCREEN is a simplified air quality forecasting tool often run within AEROMOD. These packages tailor the parameters of the Gaussian plume model to predict the most accurate rate of growth; however, in all of them, pollutants grow according to the shape of a Gaussian curve both vertically and horizontally, neglecting the local effects caused by heterogenous terrain.

Taking measurements over a realistic city model will give valuable data for one specific case but will not give a generalisable solution for the behaviour of a realistic city. However, understanding the relationship between the studied idealised cases and general realistic cases will require first the measurement of the idealised cases; for which there is a significant amount of existing literature (Carpentieri et al. 2004; Fuka et al. 2018; Xie et al. 2008; Boppana et al. 2010; Vanderwel and Ganapathisubramani 2019). Secondly realistic cases must be studied with a high fidelity of measurement so that conclusions about the similarities and assumptions made with idealised cases can be drawn. This study aims to fulfil this second step by providing high fidelity data and the analysis required to make it useful to the scientific community.

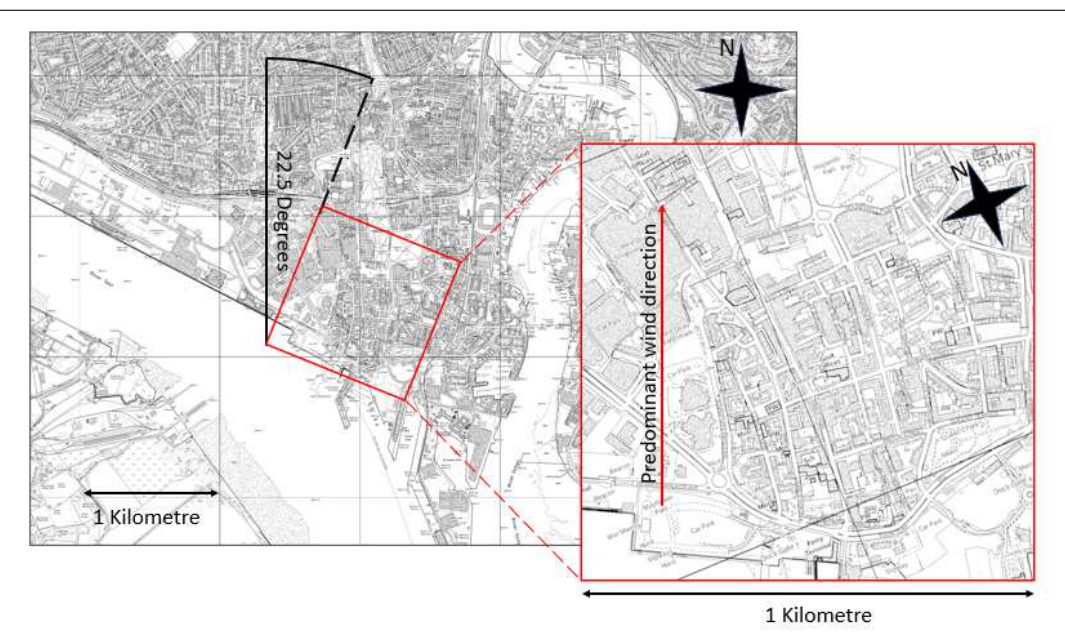


FIGURE 6.1: A map of the centre of Southampton with a zoom in on the experimental area under investigation. The predominant wind direction is marked and this was used as the flow direction when the model was in the water tunnel. This figure was generated using ordnance survey data.

6.2 Methodology

A model was created to represent $1 \, km^2$ of Southampton's city centre with a full to model scale of 1000:1. In this model, both terrain elevation and building height are represented, and the flow direction corresponds to the predominant wind direction of an onshore south-south-westerly wind (Ming De Gan et al. 2023). The section of the city chosen for measurements was selected to represent a pollutant release at the city port. This allowed the upstream edge of the model to be at sea level and not cause a step height change for the incoming flow. The experimental area and flow direction are shown in figure 6.1. This model was created using ordnance survey data.

Experimental measurements were made in the University of Southampton's Recirculating Water Tunnel (see figures 6.2 and 6.3). The city model is submerged in the water tunnel during the experimental campaign. The incoming flow was conditioned to have a boundary layer depth of approximately 300 mm and a free-stream flow velocity of $0.6 \, \text{m/s}$, with a water depth of $0.65 \, \text{m}$. Using the maximum building height of $55 \, \text{mm}$ as the length-scale, and the free-stream flow velocity, the Reynolds number was 27,000. Using the mean building height across the central section of the model, of $20 \, \text{mm}$, gives a Reynolds number of 12,000. All lengths in this paper have been made dimensionless using the characteristic building height of $H = 20 \, \text{mm}$. Conditioning of the incoming flow was carried out through the use of regularly spaced roughness elements of varying sizes, visible in figure 6.2.

In order to experimentally simulate an onshore pollutant plume from the docks, a scalar source was introduced 50 mm upstream of the model. The scalar used was Rhodamine 6G fluorescent dye, which was illuminated using a Nd-YAG laser with an emission



FIGURE 6.2: An image of the experimental setup. In this image, the upstream roughness elements are visible, followed by the 3D printed city model.

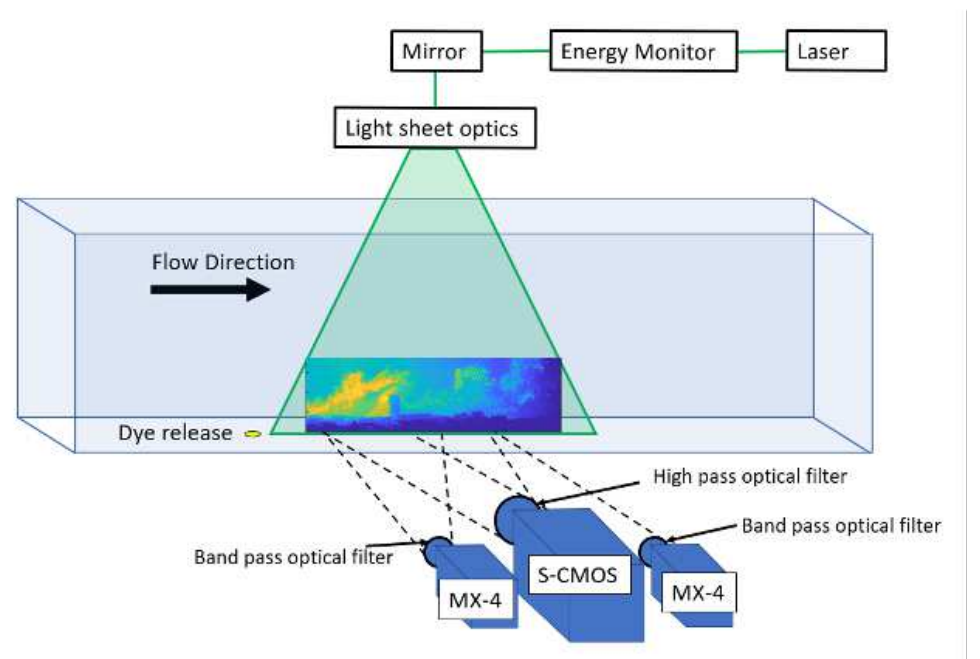


FIGURE 6.3: A diagram of the experimental setup used during acquisition of streamwise planar PIV-PLIF. An example un-calibrated PLIF image is shown under the laser sheet.

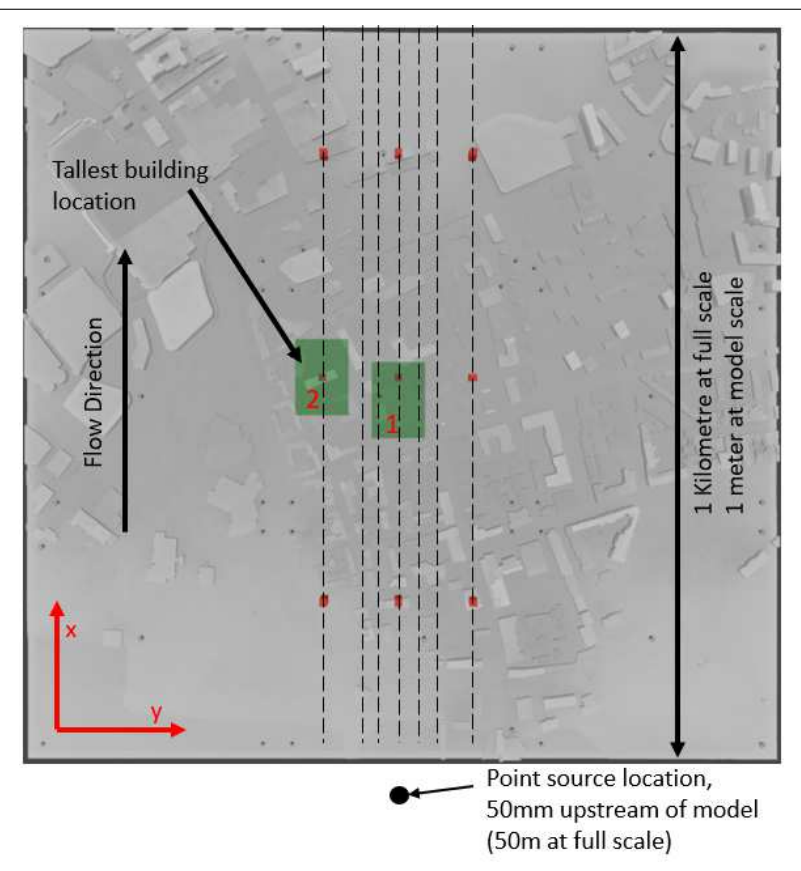


FIGURE 6.4: The 3D model that was used to generate the experimental 3D print. Dashed lines indicate the planes of the stream-wise vertical measurements. Green areas indicate the field of view of the wall-parallel measurements. Locations that the vertical profiles in figure 6.6 were extracted are represented as nine red dots. The relative location of the scalar point source has been indicated outside the model. This 3D model was produced using Ordnance Survey data.

wavelength of 532 nm. This scalar was introduced with a low enough velocity that it did not measurably affect the velocity field, and was introduced at ground level through the use of a non-intrusive tube underneath the experimental setup.

This experimental setup was used so that both PIV and PLIF data could be acquired simultaneously with the one laser sheet to measure maps of flow velocity and concentration. PLIF data was post processed using custom Matlab code (Rich T 2024), while PIV data was processed using LaVision's Davis 10.2 software and then further post processed in Matlab. PIV particles were passively seeded throughout the entire flow, at a density that allowed PIV vectors to be calculated using 32 by 32 pixel interrogation windows, with a 50% overlap. This interrogation window size gave a minimum resolution of 1 vector per 1.4 mm, at the most zoomed out measurement location. The corresponding PLIF data was acquired at a minimum resolution of 1 data-point per 0.15 mm. PLIF data was measured with a 16 bit pixel depth.

Image acquisition was carried out with a pair of LaVision MX-4 cameras for PIV, and a LaVision S-CMOS for PLIF. For all PIV and PLIF datsets 2000 PLIF images and 2000 PIV image pairs with each MX-4, were acquired for averaging. This was done at an

6.2. Methodology 83

acquisition rate of 12.5 Hz. All camera fields of view were stitched together in post-processing.

Out of the full 1000 mm model width, data was taken in the central 200 mm. This limit was chosen using visual observations into the extent of the dye plume either side of the centre line prior to experiments. For the most part, this region is a dense area of mid-sized buildings in Southampton's old city. The streets in this area form long canyons aligned North-South or East-West, which is slightly misaligned with the mean flow direction across the model, or the predominant wind direction (see figure 6.1). One of the taller buildings in central Southampton is included on the border of this region and is of a disproportionate size to the rest of the buildings. This building is visible in figure 6.4 below area 2.

In total, 14 measurements in the stream-wise vertical plane at 7 spanwise distances were captured, as well as two wall-normal orientations presented in figure 6.4. This many planes were required to resolve the shape of the plume in detail in this central 200 mm area. This further highlights the effectiveness of using PIV-PLIF to capture full fields of data. The convention used in this paper is to define downstream distance as x, cross-stream distance as y, and vertical distance as z. The scalar release location (50 mm upstream of the start of the model) is chosen as the origin.

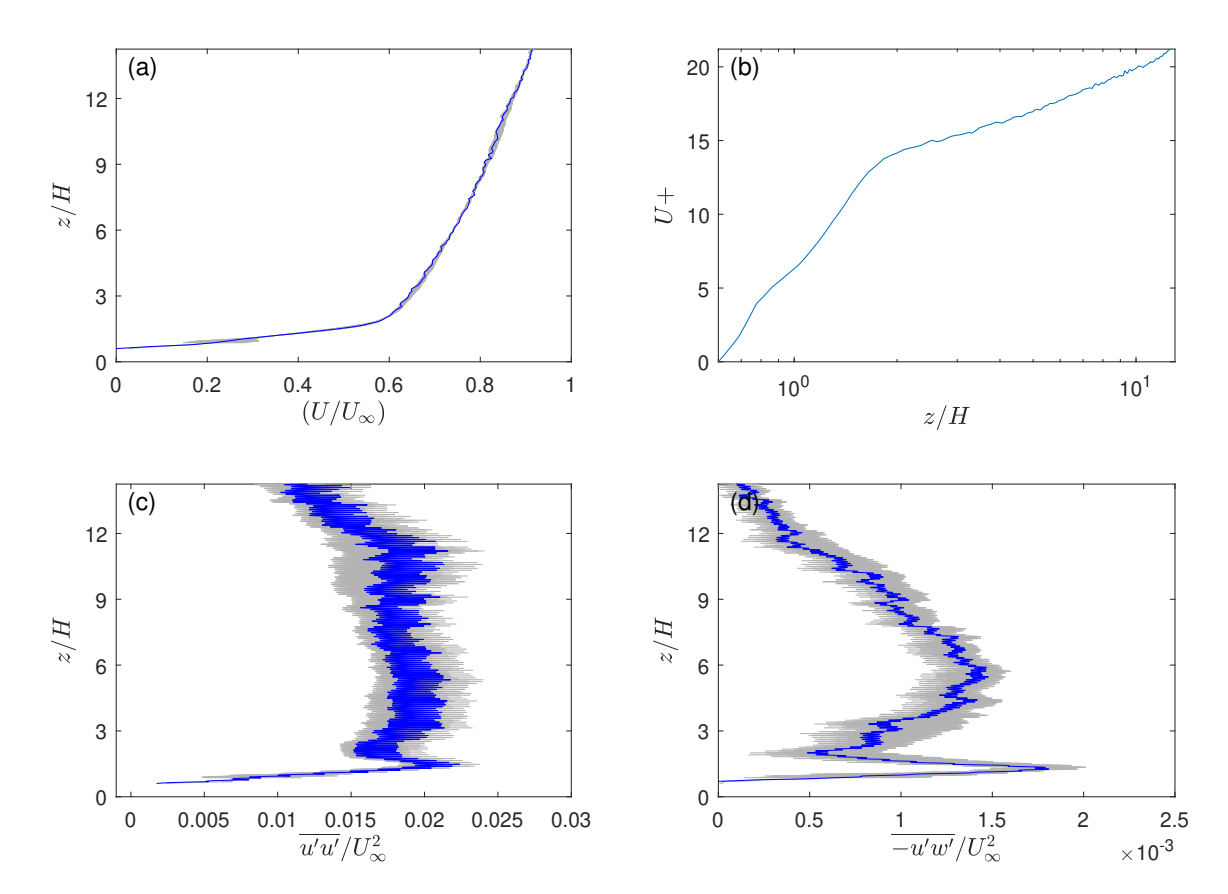


FIGURE 6.5: (a) The incoming streamwise flow velocity U/U_{∞} . (b) The incoming streamwise flow velocity normalised by the friction velocity (U^+) , plot on a semi-log scale so that the log law region of the boundary layer can be observed. (c) The profile of the variance of the streamwise velocity $\overline{u'u'}/U_{\infty}^2$ of the incoming flow. (d) The profile of the Reynolds stress $\overline{-u'w'}/U_{\infty}^2$ of the incoming flow. On plots (a), (c), and (d) error bars of one standard deviation are displayed in grey representing the uncertainty in the region of the incoming flow that was averaged in the streamwise direction.

6.3 Results

6.3.1 Characterisation of the Flow

All experiments in this study were carried out with a bulk flow velocity of $0.6 \, \text{m/s}$ and a water depth of $0.65 \, \text{m}$. Due to how deep the boundary layer is relative to the flow depth the measured free-stream velocity is $0.65 \, \text{m/s}$, and this is used as U_{∞} . Under these conditions the roughness elements thickened the boundary layer to 300 mm deep, and gave a turbulence intensity of 4%. Figure 6.5a shows this boundary layer growing towards 99% of U_{∞} , which is where the limit of the boundary layer is defined. The log law region of this boundary layer is shown in figure 6.5b and is 200 mm deep (10H). This is deep enough that the entire urban model exists within this region, as it would for a real urban case. Calculating the friction velocity using the peak of the shear stress gives a value of $0.042 \, \text{m/s}$.

Vertical profiles of velocity have been extracted from the planar PIV results at the locations marked with red dots on figure 6.4. These have been plotted on figure 6.6.

6.3. Results 85

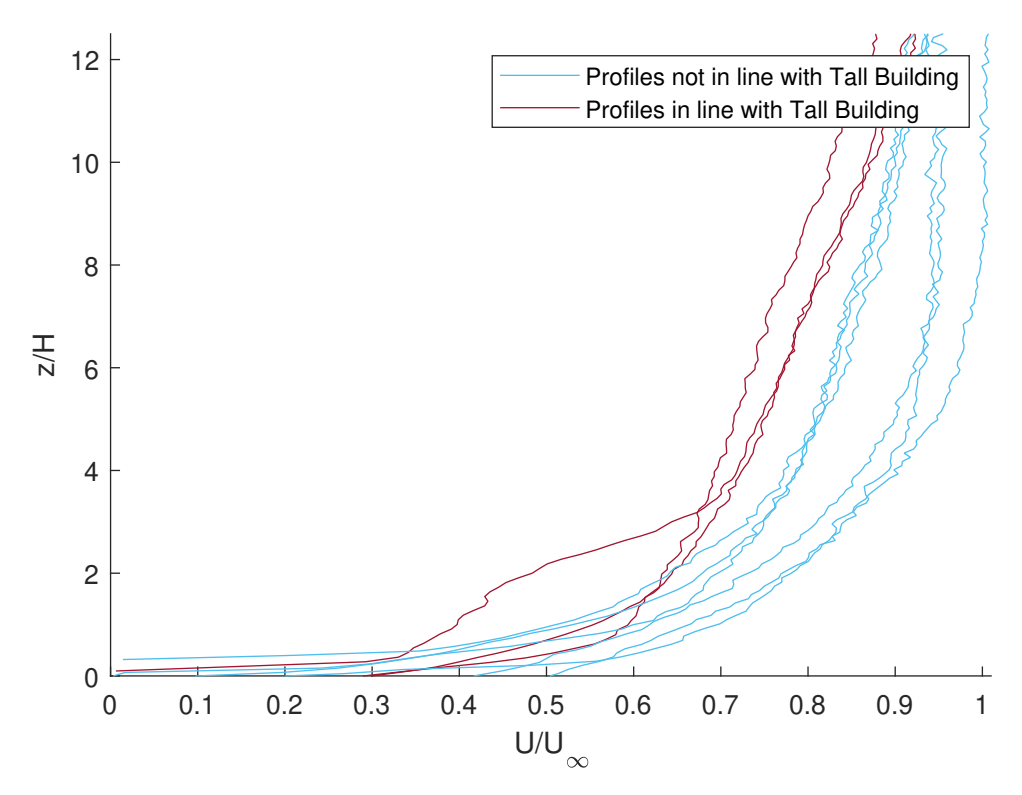


FIGURE 6.6: Vertical profiles of the streamwise velocity U/U_{∞} , extracted at locations shown in figure 6.4. The profiles in line with the tall building are shown in dark red, all others are shown in light blue. These are the left column of red dots on figure 6.4.

These profiles show show substantial variation up to roughly z/H = 12. This corresponds to the extent of the roughness sublayer in the city. The depth appears much higher than the value of 2-5H suggested by literature (Barlow and Coceal 2009). This appears to be at least in part due to the velocity profiles in line with the tall building appearing to be more significantly slowed than those not in line with it. If H is instead defined as the tallest building height in the array then H would be equal to 55 mm. Using this H_{max} value the roughness sublayer would instead be $4.3*H_{max}$ deep. Which is within the suggested 2H-5H range. This implies that the roughness sublayer is sensitive to the maximum building height even if there is just this one tall building present. This is in agreement with the study by Makedonas et al. (2021), who found that in some circumstances H_{max} was a more appropriate scaling to calculate the roughness sublayer depth.

It can be seen in figure 6.6 that the profiles in line with the tall building deviate further than the others from a typical boundary layer profile. Deviations in the velocity profile are expected in this case of a realistic city model due to randomness in local building geometries. However, the data in line with the tall building in the streamwise direction has an above average level of deviation. Mean streamwise velocity maps are shown in figures 6.7(a) and 6.7(b) for the (y/H=0) (centreline) and (y/H=-5) slice, respectively. These figures also show the same difference in street level velocity noticed in figure 6.6, particularly in the wake downstream of the tall building.

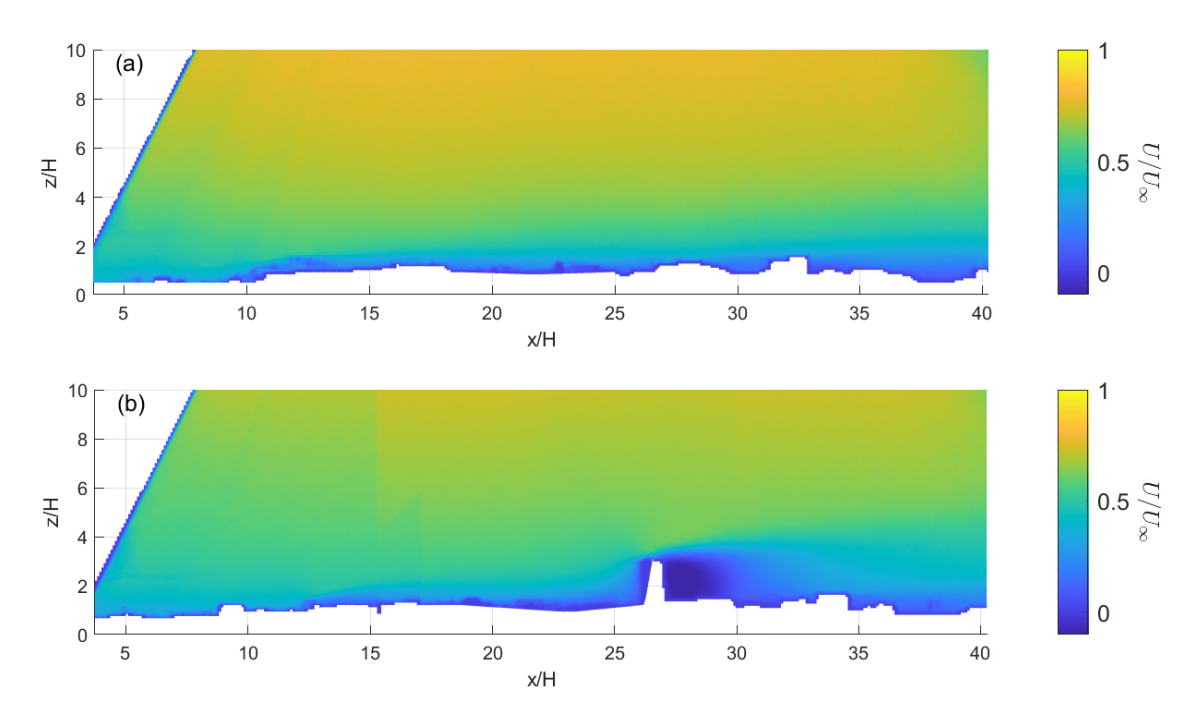


FIGURE 6.7: Mean streamwise velocity fields above the city model normalised by U_{∞} , (a) shows data on the centerline and (b) shows data at (y/H = -5).

6.3.2 Characteristics of the Plume

Figure 6.8 shows results from the concentration field measured at y/H = -5. In figure 6.8a, it can be observed that the instantaneous results are very sparse and intermittent relative to the mean results, however, they are at a much higher intensity than the mean or variance. The mean field shown in figure 6.8b shows a typical plume shape. In both this figure and the variance in figure 6.8c, the effect of the same tall building mentioned in figure 6.6 is again visible. In figures 6.8b and 6.8c, the tall building reduces the mean and variance of the concentration in its immediate wake.

The growth of the plume vertically was calculated as the half-height at half-max of the mean concentration field. This was done for all seven streamwise concentration slices and has been plotted on a log-log scale in figure 6.9. These growth curves converge well and the line fits to them have a mean exponent of 0.68 which is a little higher than the expected value of 0.5 for an unobstructed Gaussian plume (Castro and Vanderwel 2021). There are fluctuations present in the graph as is expected due to the buildings present in the model; however they do not obscure the overall trend, and the gradients of the lines are consistent.

The lateral growth of the plume was explored in two ways, first using a method well established in literature, and then a less established method for use with experimental results. The results of these two methods are compared and used together to generate a more comprehensive map of the plume shape. In the first method, horizontal profiles of the concentration field at z/H=3 were extracted from the planar data. These were then both interpolated and extrapolated as a Gaussian profile with a vertical offset, into a

6.3. Results 87

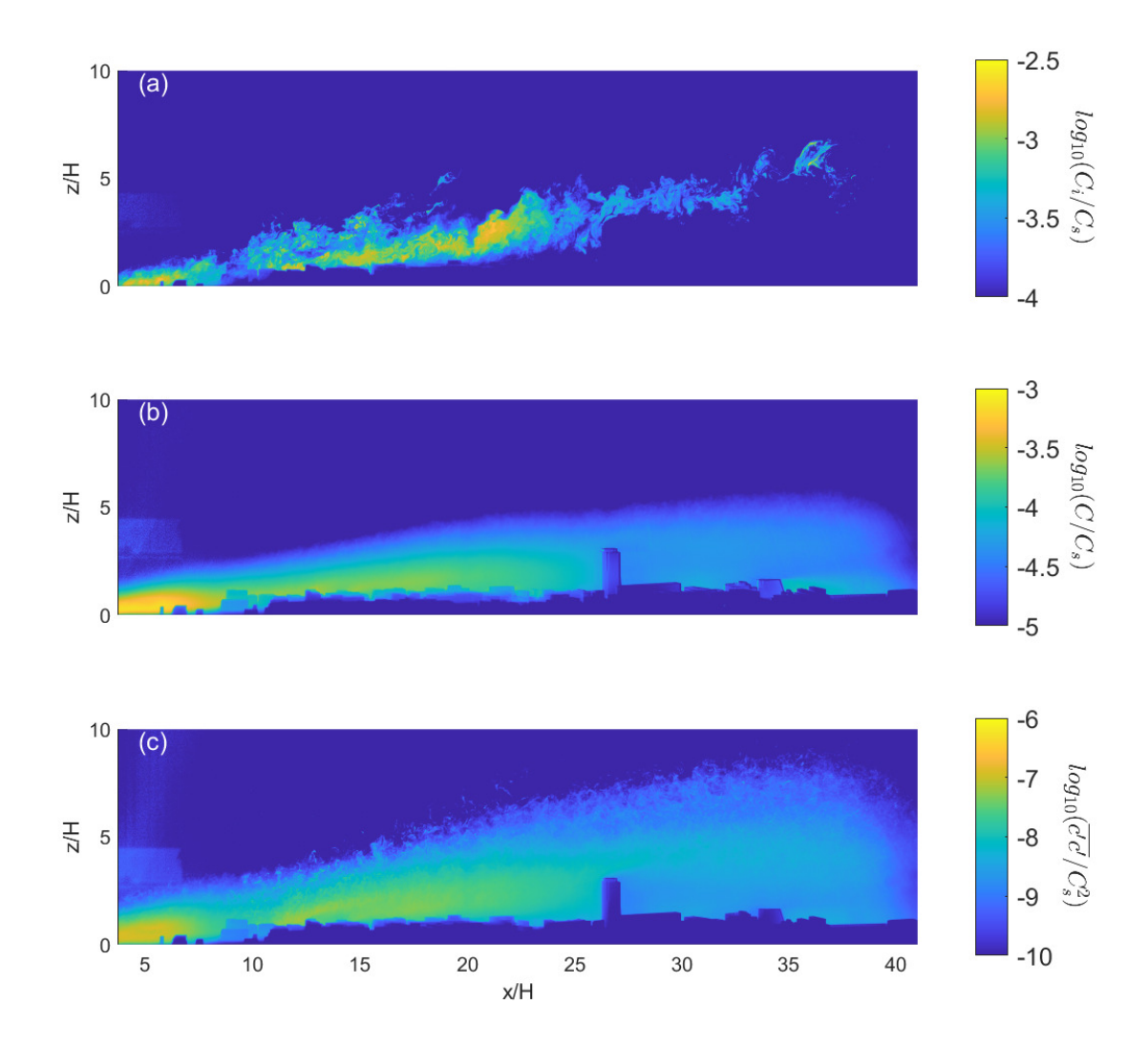


FIGURE 6.8: Examples of the planar concentration results used to define the scalar plume taken from the planar slice at y/H=-5, all shown on log scales for clarity. (a) An example of the instantaneous results. (b) The mean concentration field along this slice. (c) The concentration variance field. These fields were all calculated using two stitched fields of view taken at different times which were normalised by their source release concentration C_s .

concentration profile at the height z/H = 3. This was done through curve fitting to equation:

$$C(y) = ae^{-\frac{(y-b)^2}{2c^2}} + d,$$
 (6.1)

in which a, b, c, and d are tunable coefficients. Equation 6.1 was fit at 500 separate downstream locations. Due to this curve fitting in the y direction there is horizontal banding visible in figure 6.10 (a). Examples of this curve fitting are shown in figure 6.10 (b). Fitting these curves to a reasonable degree of accuracy required the use of Matlab code that iterated down the curves in the positive x/H direction. The closest fit results were found when the start-point estimates of a,b,c, and d were the final results of the previous (upstream) curve, and also the upper and lower fitting limit were written as a function of x/H.

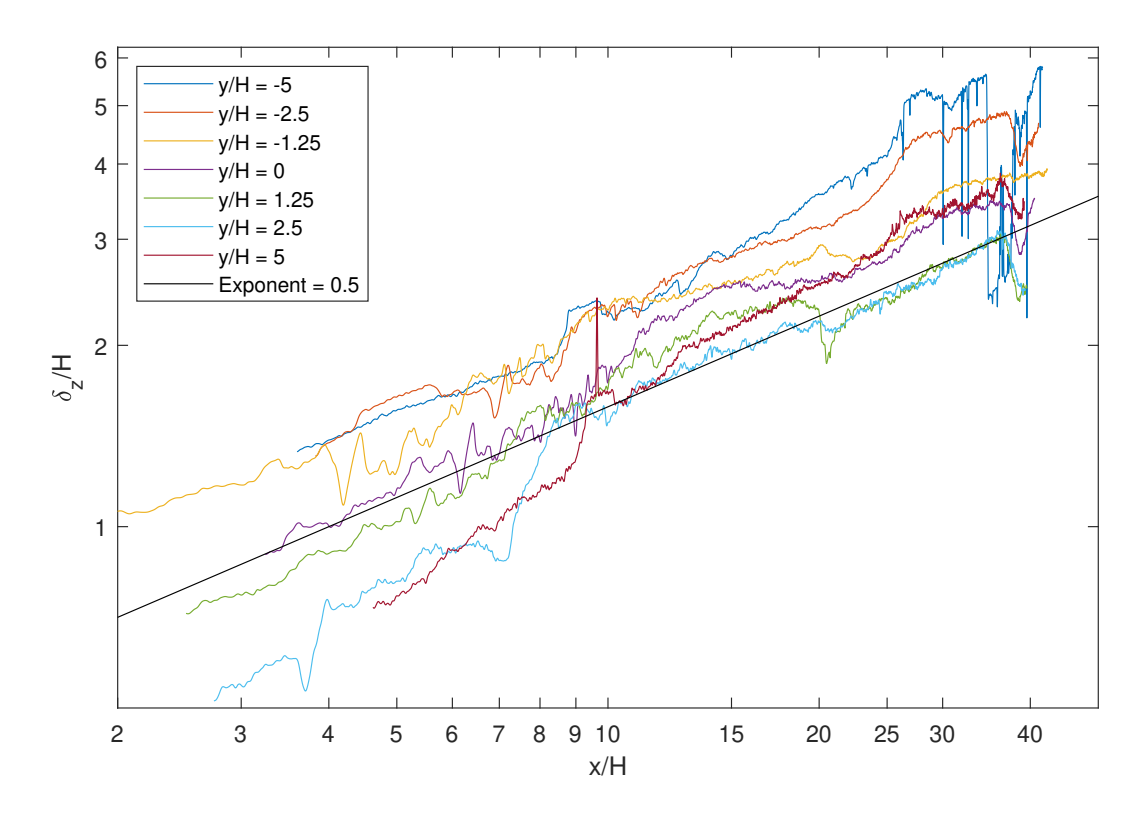


FIGURE 6.9: A figure showing the vertical growth of the scalar plume. This was calculated using the local half height at half max and plot against the downstream distance (x/H). Both axis are on a log scale and each line represents a different cross stream location. This is with the exception of the final line in the legend, which is a reference value for the exponent of 0.5.

An isocontour of the flow was generated using a cross-section of the planar mean slices (example shown in 6.8b) and this is shown in figure 6.10 (a). This isocontour shows the plume having a deflection from the mean flow direction and towards the negative y direction. Using the plume peak location to define direction gives a deflection of 4.5 degrees away from the mean flow direction. The direction of the plume deflection is towards that of the mean street canyon orientation in the central region of the city, which was pointed out on figure 6.1.

Secondly, the same analysis of plume deflection was attempted through the use of an isosurface of a fixed concentration value to define the plume shape. This process is shown in figure 6.10 c, in which the height at which plume concentration reached 0.002% of the source concentration is plotted for each downstream location. Then a Gaussian fit is carried out across these points using the equation

$$Z_{0.002\%}(y) = ae^{-\frac{(y-b)^2}{2c^2}}. (6.2)$$

The only difference between this equation and equation 6.1 is the lack of vertical offset in this case. This is because the value chosen for the isosurface limit is higher than the background noise meaning that, outside the plume limits, the isosurface height will be zero. These curves were then extrapolated to create a full isosurface of $Z_{0.002\%}/H$ at

6.3. Results

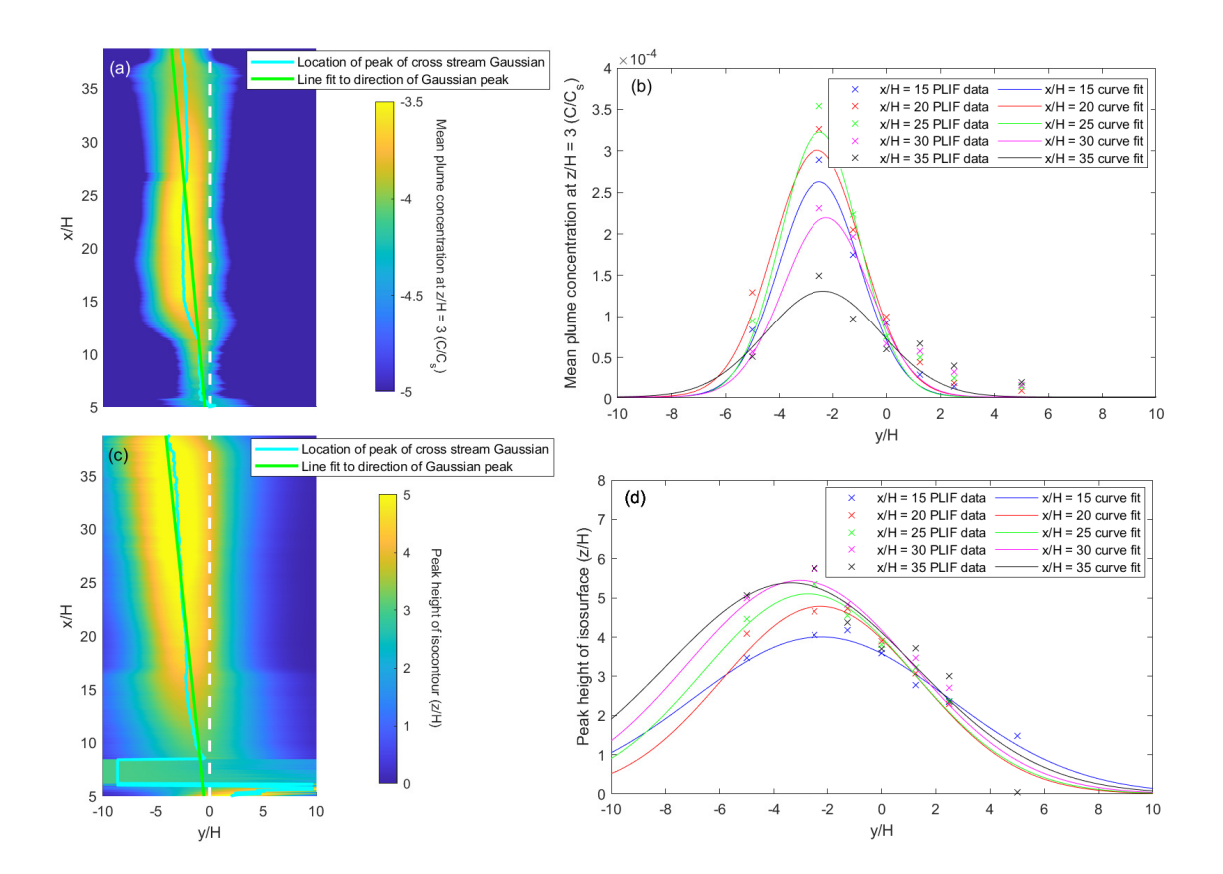


FIGURE 6.10: (a) A map of the plume width defined using an isocontour of mean concentration calculated from profiles of the planar concentration slices as shown in figure 6.8b. These profiles were taken at z/H=3 and extrapolated spanwise as a Gaussian profile with a zero offset, example profiles are shown in (b). The displacement of the centre of the mean plume is shown in blue. The best-fit line in green shows the centre follows a mean direction of 4.5 degrees to the left of the mean flow direction. (c) A map of the upper limit of the plume as defined as the isosurface of 0.002 percent of the source concentration. The displacement of the centre of the mean plume is shown in blue. The best-fit line in green shows the centre follows a mean direction of 5.1 degrees to the left of the mean flow direction. (d) Examples of the data used to calculate the cross-stream profiles of plume height. This data was extrapolated using a Gaussian fit.

which $C/C_s = 0.00002$, shown in figure 6.10 (c). This surface appears to have a far smoother profile than that calculated using the mean concentration values (figure 6.10 (a)). This is likely due to the data used in forming this isosurface being representative of the outer plume limits instead of the inner plume, and as such avoiding some of the fluctuations associated with individual buildings. Fitting a line to the peaks of the cross-stream profiles, in the same way as was done previously, shows a deflection of 5.1 degrees in the -y direction. This number is very similar to that calculated from 6.10 (a) and provides some validation for the comparability of the two techniques that were used.

The concentration field at y/H = -5 (shown in figure 6.8b) shows an area of unexpectedly high concentration for its downstream distance at x/H = 35. This section has been magnified in figure 6.11 (a). Referring this field back to the reference model

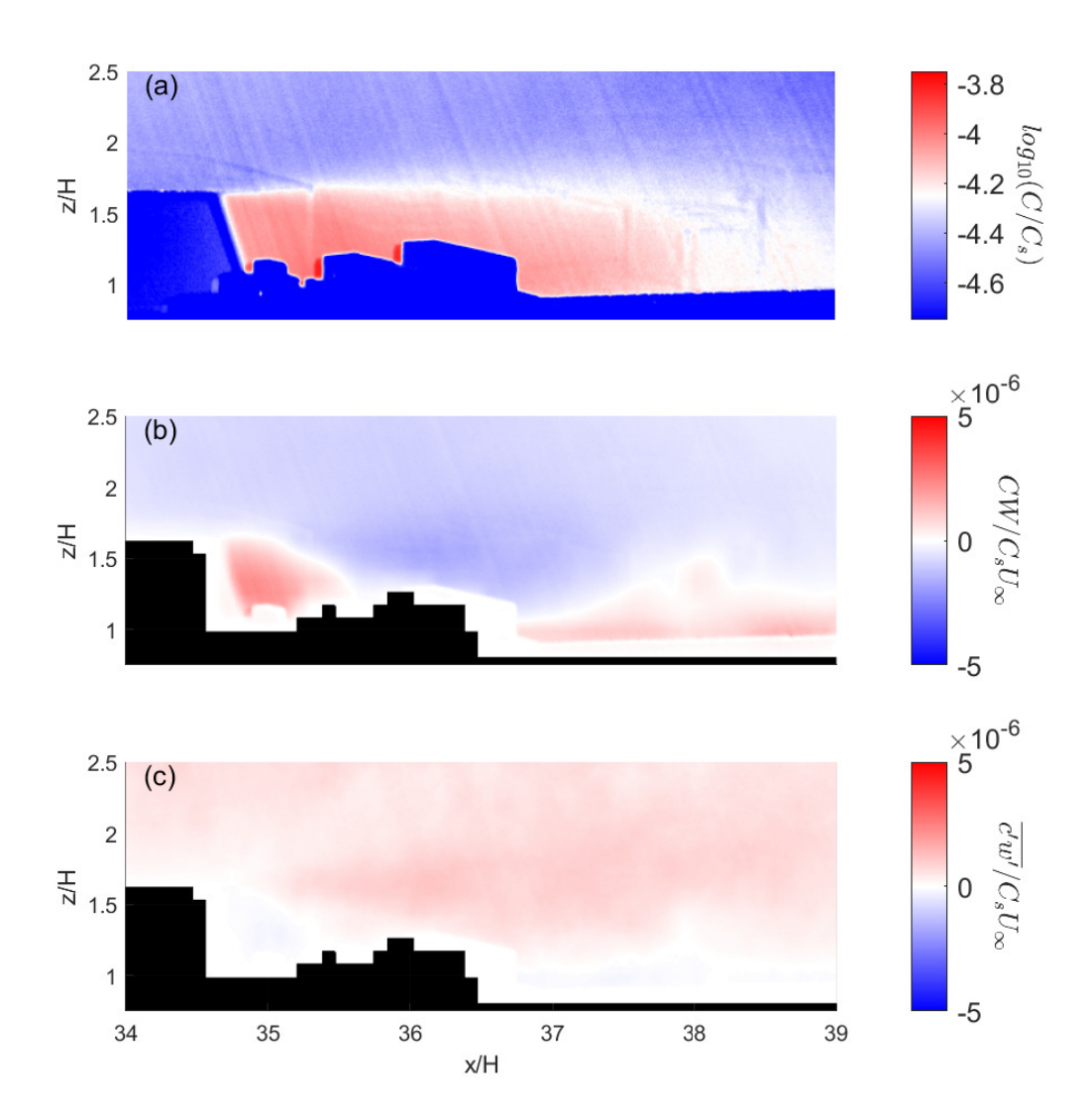


FIGURE 6.11: A zoomed section of the planar slice taken at y/H = -5, shown fully in figure 6.8. (a) Mean concentration on a log_{10} scale. (b) The vertical advective flux CW. (c) The vertical turbulent flux $\overline{c'w'}$. The area zoomed in on in this figure is at a location that a measurement plane intersects with one of the longest street canyons in the model.

reveals that this section, which looks like a building's wake, is instead a region in which a large street-canyon crosses the measurement plane. Figure 6.11 (b) and 6.11 (c) show that despite the high local concentration found in figure 6.11 (a), both the advective and turbulent vertical fluxes, which are the mechanisms of vertical transport, are not at as high a value as expected. This implies that the majority of the scalar in this street canyon is not being transported vertically and is instead being channelled down the canyon.

This provides a possible answer to the question of why the plume appears to be deflecting in figures 6.10 (a) and 6.10 (c), as most street canyons in the city model are pointing in the negative y direction. It is this direction that the plume is also deflecting. The mean street canyon orientation is at an angle of 18 degrees to the left of the centreline, whereas plume deflection is calculated as between 4.5 and 5.1 degrees.

6.3. Results 91

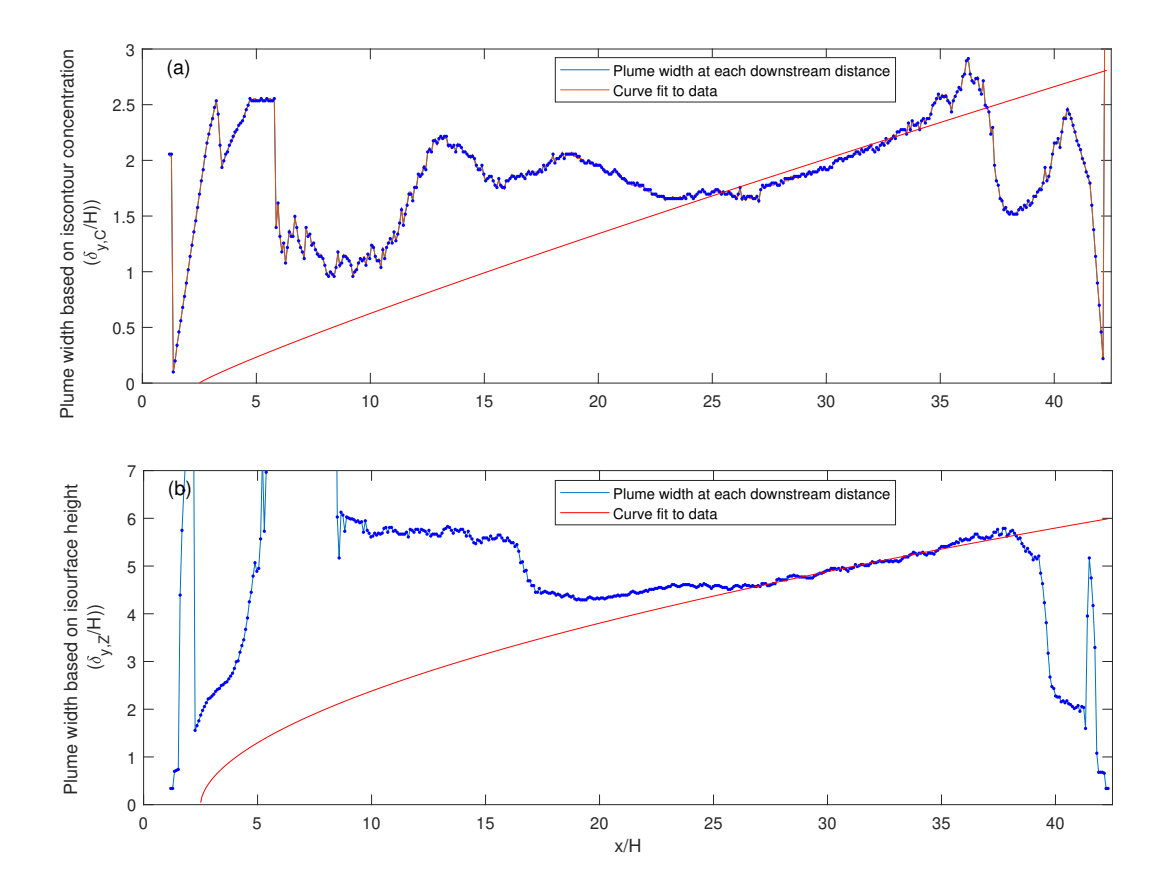


FIGURE 6.12: (a) Plume half width against increasing downstream distance from the scalar source, this is defined using the half-max. This curve follows equation 6.3 where c=0.90 and is only fit to data beyond x/H=20. (b) Plume half width against increasing downstream distance from the scalar source, this is defined using the half-height of the isosurface. This curve follows equation 6.3 where c=0.55 and is only fit to data beyond x/H=20.

Figure 6.12 (a) shows a fit of a power law to the growth of the width of the plume as calculated from the data in figure 6.10 (a), against x/H. This width has been defined as the half-width at half-max of the curves shown in figure 6.10 (b) The equation used to plot the width growth curve is given by

$$Z_{0.002\%}(x) = a(x - 2.5)^{c}, \tag{6.3}$$

with coefficients calculated to be a=0.11, and c=0.90. The form of this growth curve follows that used by Lim and Vanderwel (2023), in which an offset was added to the x value to aid in curve fitting . This curve has only been fit to the downstream data far from the plume source. This was done as it is not valid to fit a Gaussian curve to the near source region of a plume (Lim and Vanderwel 2023), and also because the tall building present at y/H=-5 influences the plume width up until mid way down the field of view. This Gaussian curve has an exponent of 0.9 in the downstream region, which is much higher than the expected value of c=0.50 (Castro and Vanderwel 2021). This curve fit is not as precise as would be hoped, but this is assumed to be due to the

variability generated by individual building effects being very significant.

Due to the isosurface shown in figure 6.10 (c) having a smoother profile than that in figure 6.10 (a), plotting the growth of the half-height at half-max of the isosurface curves shown in figure 6.10 (d) was also attempted. Equation 6.3 was again used and this has been plotted against x/H in figure 6.12 (b). In this case the coefficients were calculated as a = 0.78, and c = 0.55. This curve shows a more convincing fit than that calculated in figure 6.12 (a); however this method is less conventional in existing literature. This is in part due to the fact that calculating an isosurface requires high resolution quantitative data in three dimensions, and this is more often found in computational studies (Fuka et al. 2018). Nevertheless in this case it allowed for cutting through much of the background noise in comparison to the conventional method of using a mean concentration isocontour (figure 6.12 (a)). The plume growth indicated by c = 0.55 also agrees more with what would be expected of a Gaussian plume in an urban environment than the value of c = 0.90 given by figure 6.12 (a). Both figures 6.12 (a), and 6.12 (b) were plotted on linear-linear axis, unlike figure 6.9 which was plot on a log-log axis. This was done to increase the clarity of these figures, as they both had higher variability than figure 6.9.

6.3.3 The Components of Flux

The vertical advective flux is defined as CW, in which C and W are the mean concentration and vertical velocity components, respectively. The vertical turbulent flux is defined as $\overline{c'w'}$, in which c' and w' are the fluctuating concentration and vertical velocity components, respectively. Figure 6.13 shows the vertical advective and turbulent fluxes on the centreline and at y/H=-5. Figures 6.13 (a), 6.13 (b), 6.13 (c), and 6.13 (d) show the centreline plane. In these figures, it can be observed that the direction of the vertical advective flux varies while the direction of the vertical turbulent flux stays constant. It is also observable that the maximum magnitude of the advective flux is larger than that of the turbulent flux, but that their orders of magnitude remain comparable. Figures 6.13 (e), 6.13 (f), 6.13 (g), and 6.13 (h) show very similar patterns in the relative signs and strengths of the turbulent and advective fluxes. The area in the vicinity of the tallest building (x/H=27) shows higher levels of advective fluxes without a corresponding spike in turbulent fluxes. The magnitudes and directions of the two fluxes also do not correlate in shape or location above the building.

Figure 6.14 shows wall parallel slices of the turbulent and advective components of the vertical scalar flux. Figures 6.14(a) and 6.14(b) are taken at position 1 in figure 6.4, while figures 6.14(c) and 6.14(d) are taken at position 2 on figure 6.4. All slices of data were taken at a height of z/H = 3.

Figures 6.14(a) and 6.14(b) show the behaviour of the plume along the centreline of the model. These figures show the advective flux having a uniform upwards direction and a magnitude that only varies slightly over the measurement area while the turbulent flux

6.3. Results 93

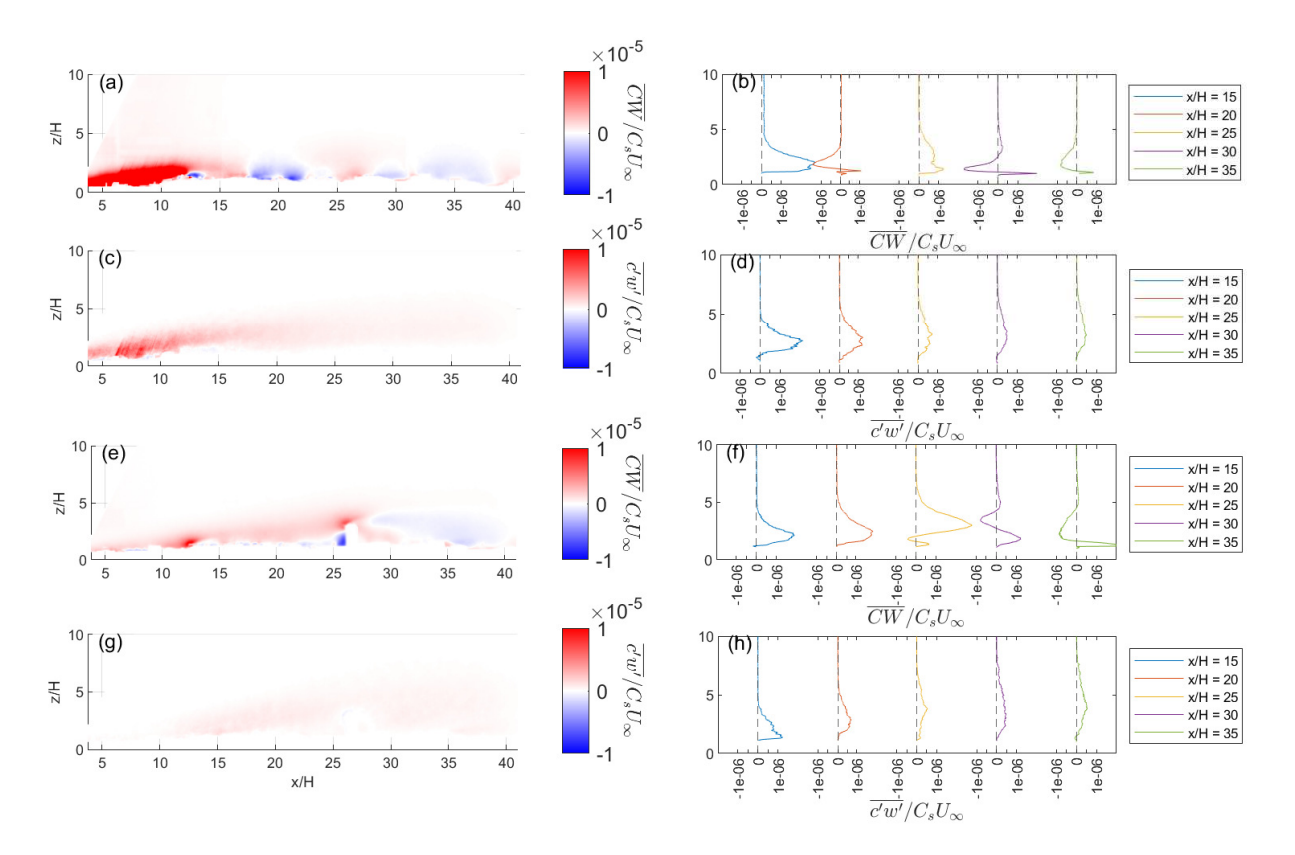


FIGURE 6.13: Figures (a) and (b) show the vertical advective scalar flux field on the centreline and profiles extracted from this field respectively. Figures (c) and (d) show the vertical turbulent scalar flux field on the centreline and profiles extracted from this field respectively. Figures (e) and (f) show the vertical advective scalar flux field at y/H=-5 and profiles extracted from this field respectively. Figures (g) and (h) show the vertical turbulent scalar flux field at y/H=-5 and profiles extracted from this field respectively. All scalar flux fields are shown on the same colourmap and all profiles are scaled the same as each other to aid in comparison.

has a shape more localised towards the centreline of the plume, and switches direction at each side of the field of view. In this field of view the magnitude of the turbulent flux at its peak is higher than that of the advective flux.

Figures 6.14(c) and 6.14(d) show the vertical scalar fluxes above the tallest building in the model. Figure 6.14(c) shows much higher magnitudes of advective fluxes than figure 6.14(a) does. It also shows a large negative region in the wake of the tall building. In contrast, figure 6.14(d) shows turbulent fluxes of a similar magnitude to those visible in figure 6.14(b). These fluxes have a general positive sign with a small negative region emanating from the back of the tall building. This negative region does not follow the direction of the mean flow and instead travels normal to the backward face of this building. The absence of a rooftop shear layer in the turbulent flux map behind the tall building in figure 6.13(g), is explained by figure 6.14(d). This figure shows that the rooftop shear layer does exist, but due to the fact that it does not follow the mean flow direction it is not visible in figure 6.13(g), despite the building being visible. It can be seen on figure 6.14(d) that a line following y/h = -5 does not hit any high points in turbulent flux. However, a line at the same point in figure 6.14(c) does show the same maximum then minimum peak in advective flux that is visible in figure 6.13(e).

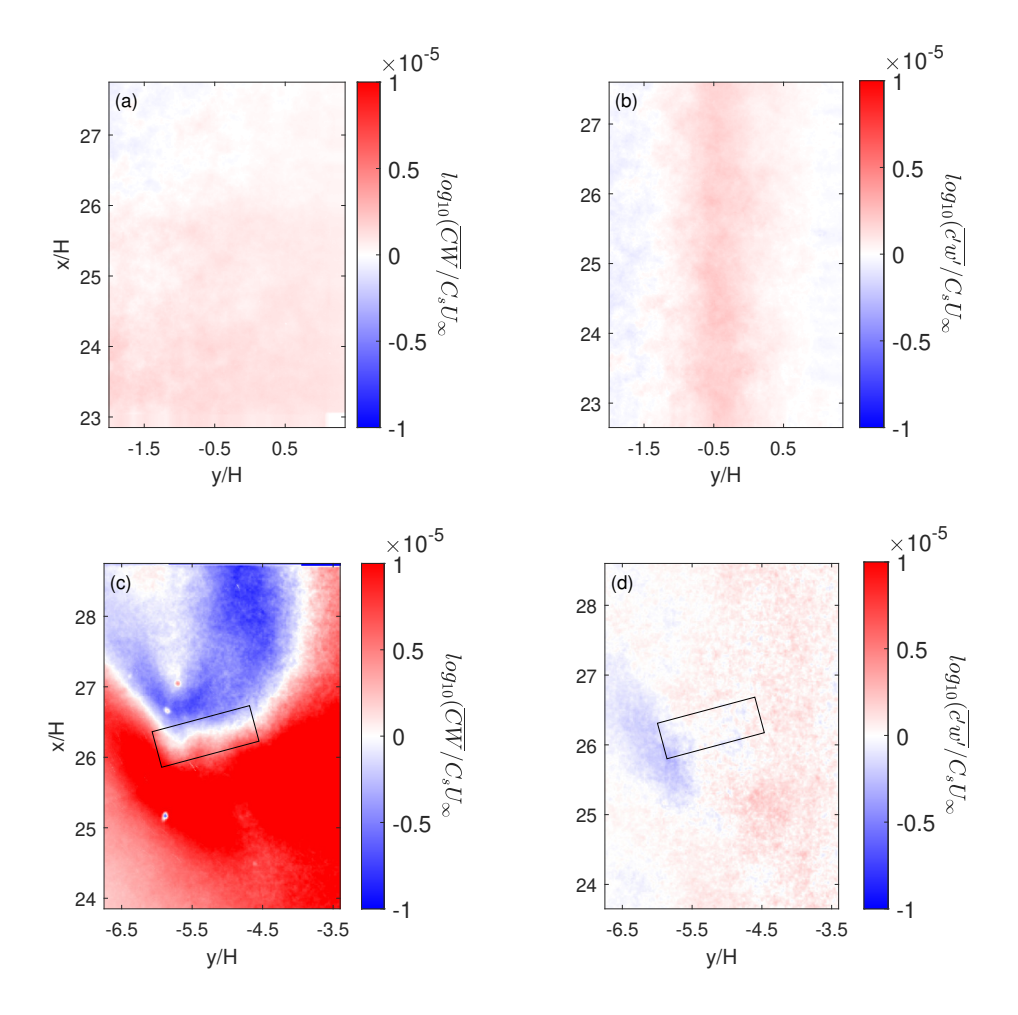


FIGURE 6.14: The vertical turbulent and advective flux fields above the centreline and tallest building of the city model, as marked in figure 6.4. Planes (a) and (b) were extracted at position 1 in figure 6.4, graphs (c) and (d) were extracted at position 2. These slices were extracted at 3H (60 mm) above the tunnel floor. The location of the tall building is outlined by a black rectangle in figures 6.14 (c) and 6.14 (d).

In both locations, the turbulent and advective flux components show localised patterns that are distinct from each other. They also have a magnitude that is comparable to each other and to the fluxes measured in the planar slices (figure 6.13). This is with the exception of the advective fluxes in the immediate vicinity of the tall building (figure 6.14(c)). The shape of the flux components around the tall building are highly three dimensional, in part due to its angle relative to the mean flow. This makes fully resolving the shape of these components complex, even with multiple slices of data.

6.4. Discussion 95

6.4 Discussion

6.4.1 The Fluid Dynamic Characteristics of a City

The influence of the urban environment on a fluid flow can be summarised in three ways. These can be described as, firstly, an area with high average roughness which increases turbulence and mixing. The second characteristic is as regions of large scale order in which patterns of buildings create neighbourhood scale structures. The third characteristic is the effect of the few buildings that are disproportionately large relative to the mean building height, these create localised unpredictable areas.

The effect of the high average roughness is what has caused the high rate of plume growth (figures 6.9 and 6.12). It can be concluded, because of the high Schmidt number of these experiments, that most of the cross stream mixing is due to cross stream turbulent and advective fluxes, instead of molecular diffusion. These are presumed to be caused by the local surface roughness of the model. In particular, figures 6.13 and 6.14 show that in nearly all locations the vertical turbulent fluxes are smaller than the vertical advective fluxes but of a comparable magnitude. This again implies that the turbulence generated by the city model is having a large effect on the behaviour and growth of the scalar plume.

The most noticeable neighbourhood scale order visible in the city model is present in the form of an ordered grid of street canyons aligned North-South and East-West. Due to the flow direction being South-South-West the street canyon grid is slightly misaligned with the mean flow direction, towards the negative y direction. It is presumed that the deviation of the mean plume direction from the mean flow direction is a consequence of the flows misalignment with the street canyons, as the plume is deviating towards the street canyon direction. This is visible in figures 6.10 (a) and 6.10 (c), and is supported by the observation of a high scalar concentration and low vertical transport inside a street canyon in figure 6.11. These values imply that scalar within these street canyons is being transported along the direction of the canyons.

The disproportionate effect of tall buildings is illustrated well by the y/H=-5 slice and how it causes most measurements in its vicinity to be distinctly different to those over the rest of the city model. For example, the velocity profiles over the city model shown in figure 6.6 deviate much further from the mean boundary layer when in line with the tall building. It is also unique that the wall parallel slice above the tall building shown in figures 6.14 (c) and 6.14 (d) is the only area in the flow in which the magnitude of the advective flux is much higher than that of the turbulent flux. Figure 6.8(b) shows that in the immediate wake of the tall building the scalar concentration is lower than in the mean flow, but that the outer edge of the plume is driven higher in the region of the rooftop shear layer. This is consistent with the measurements of Lim et al. (2022) on a different city model with a tall building present. The gradient diffusion hypothesis implies that scalar will be mixed down concentration gradients, towards low

concentration regions (Britter and Hanna 2003). Applying this assumption, it is possible to hypothesize that the negative turbulent flux region visible in figure 6.14 (d) is being caused by the low concentration region in the wake of the tall building (visible in figure 6.8 (a)). This has created an unusual circumstance in which the direction of the local concentration gradient is inverted compared to the rest of the flow. The presence of this region shows that correctly predicting the behaviour of turbulent fluxes in the vicinity of this tall building is challenging, and is highly reliant on knowing the mean concentration field accurately.

6.4.2 With Regards to Modelling the Plume

In this specific experimental case, a Gaussian model would struggle to accurately model the plume for several reasons. A Gaussian model would fail to accurately resolve the erratic growth of the plume in the near-field, and would instead average the effects of individual buildings. It would also fail to model the scalar being channelled in the street canyons, and deflected by the tall building. In this case, the uncertainties in the Gaussian approximation would cause a significant deviation from the measured experimental result.

This result is notable because it points out the problems with using, the widely used, Gaussian plume model to predict dispersion. RANS or LES simulations will fully simulate the advective scalar fluxes and retain higher accuracy; however most fast response models, such as ADMS and ALOHA, purely use a Gaussian model.

The ADMS and ALOHA models are particularly relevant to mention because the case that was experimentally simulated here is the type of problem that a fast response model, such as these, would be used for. These failings are caused by inaccurately modelled turbulent fluxes and oversimplification of urban heterogeneity.

The current hypothesis presented here is that the key street canyons, at the centre of this model, are trapping dye and acting as a secondary line source. This behaviour is hard to predict due to it being an effect of non homogenous roughness in the urban environment. One existing study that observed a similar effect was that by Marucci and Carpentieri (2020), and this is because the idealised array tested in that case was examined at a small angle to the incoming flow. It is possible that the inaccuracy in the Gaussian plume model observed in this study is caused by similar behaviour, in which street canyons are misaligned with the mean flow direction. This requires study through further investigations into realistic urban environments; it is important because these flows, in which a pollutant plume is slightly misaligned with key street canyons, are likely more common for realistic cities than in studies into idealised arrays.

6.5. Conclusion 97

6.5 Conclusion

Carrying out this experiment has provided unique measurements and maps of the turbulent processes over a realistic city model. These measurements are important as they show the limitations of studying idealised models, and possibly indicate where inaccuracy may be arising. These measurements and this dataset, while highly valuable in the perspective they offer, are highly case specific. This data is most valuable as either a validation for modelling techniques, or a point of contrast for studies into idealised arrays. It is suggested that further study is carried out to test if the characteristics observed in this case are replicated in other realistic models.

One of the main goals of this study was to observe the comparative magnitudes of the vertical turbulent and advective fluxes. This is important information as it can be compared to modelled results, and particularly the turbulent flux is a characteristic that is rarely measured experimentally. In the experimental case, it was found that at nearly all areas (asides from in the vicinity of the tall building) the relative magnitudes of the vertical turbulent and advective fluxes were comparable. This is visible in figures 6.13 and 6.14, and is in agreement with the previous study of a tall building carried out by Rich and Vanderwel (2024).

The shape of the mean plume shows some strong influence from the urban landscape. Its deflection from the mean flow direction is hypothesized to be caused by the neighbourhood scale structure that is the street canyon grid. This is visible in figures 6.12 (a), and 6.12 (b), and is supported by the high scalar concentration measured in the street canyon in figure 6.11 (a). The plume still largely follows a Gaussian distribution, but the width and height of this Gaussian distribution is sensitive to local building geometry.

These results have implications that should be considered in city design, when the cities have similar characteristics to Southampton. It is implied by the scalar channelling that has been observed, that when busy pedestrian streets must be down-wind, and in proximity, to pollutant sources, they should not be aligned towards the pollutant source. If they are aligned towards the pollutant source then it is safer to have them limited in length, or broken up into smaller street-canyons. Despite the fact that the results that were acquired here are case-specific, this conclusion for city design is generalisable to other cities with industry in close proximity to pedestrianised areas.

To summarise, the effect of the urban environment on the flow and the scalar plume is complex but it can be decomposed into three main components. These are the high mean roughness caused by the presence of the buildings and their typically random distributions, neighbourhood scale order, and disproportionately large individual buildings.

Chapter 7

Conclusions

7.1 Summary of Content

The aims of this thesis were set out as:

- 1. Objective 1 was to develop and validate the PLIF methodology for passive scalar measurements in a water tunnel. Specifically, to assess and improve the validity and accuracy of the process of translating the measured fluorescence intensity to concentration. An additional objective was to assess the suitability of the new consumer LaVision software package compared to custom MATLAB analyses. This goal was intended to result in the development of a methodology allowing for the PLIF technique to be carried out accurately.
- 2. Objective 2 was to utilise coupled PIV/PLIF to explore the fundamental features of air pollution transport in boundary layer flows. This was used as a baseline to compare to previous studies into idealised geometries, with the goal of providing new insights, while also being a reasonable starting point for carrying out PIV/PLIF experiments.
- 3. Objective 3 was to build a model of the city of Southampton, and obtain high-fidelity measurements of air pollution distribution and transport. The completion of this goal required the acquisition of a simultaneous PIV-PLIF dataset over a realistic city model.

In the course of this PhD all of these goals have been met.

In this thesis, developments were made on the PLIF technique (chapter 4), and simultaneous PIV-PLIF was used to study both an idealised individual building model (chapter 5), and a realistic scaled city model (chapter 6). Both studies used planar and stereo PIV-PLIF to measure simultaneous velocity and concentration statistics at a high spatial resolution. This data was used to calculate fields of turbulent and advective scalar fluxes.

The investigation into the PLIF technique highlighted problems with the Davis 10.2 PLIF module offered by LaVision and these problems have been communicated back to the developers of the module. As an alternative, a Matlab code package was developed and made available on Github which offers the functions required for an acceptable level of accuracy. Several novel features were also added in this package along with the base functions that were deemed necessary. The new features added in the code were a scaling background subtraction, and an algorithmic calculation of the absorptivity variable from calibration data. The scaling background subtraction was added to mitigate dye build up during an experimental measurement. It works by taking a baseline measurement of the background from before an experiment begins and adjusting it according to a calculated gradient. This gradient is calculated using a mean light intensity of a defined freestream section of the experimental images. The algorithmic absorptivity correction iterates the calibration process until the concentration images intensities align with the known concentration values in the calibration tanks. This process optimises the attenuation correction for a particular area of the image which can be chosen to be the area of interest.

The studies of an individual tall building in chapter 5 measured both centre-line planar PIV-PLIF and cross-stream stereo PIV-PLIF. It was found that the rooftop shear layer was not transporting as high an amount of dye as was expected based on previous literature on the same building model (Lim et al. 2022). Plotting vertical profiles of the mean scalar concentration and vertical velocity ahead of the individual building showed that 94% of the scalar was impinging below the stagnation point. It was hypothesised that the majority of scalar impinging below this point was being transported laterally into the horseshoe vortex around the base of the building. This hypothesis was supported by the stereo PIV-PLIF showing a dual peak shape in the concentration profile at all points downstream of the individual building. The tall building results are useful in expanding on the behaviours of scalars in the presence of idealised structures, in contrast, chapter 6 deals with a realistic 3D printed city model. The results of a study like this are harder to generalise but hold valuable insights towards understanding the behaviour of real world cases. These studies focused on the plume characteristics and respective strengths of the turbulent and advective scalar fluxes.

The investigation into plume behaviour found the city structure below the plume causing a deflection in the mean plume direction away from the mean flow direction. Further investigation into the concentrations and fluxes revealed that high concentrations were present within the street canyons of the model. Due to the street canyons diverting from the mean flow direction to the same side as the plume deflection it is hypothesised that these street canyons are at least partially responsible for redirecting the plume sideways.

Plume growth was found to be variable due to the plume interacting with the city landscape in the measurement area. Nevertheless, it was found that, when defining plume growth using the half-width at half-max, the plume was found to be growing at a similar rate both vertically and horizontally. The plume growth rate horizontally was

difficult to quantify due to noise, and therefore quantifying it was attempted using two methods. It was found that both calculated exponents, of 0.55 and 0.90, exceeded the expected exponent of 0.5 (Castro and Vanderwel 2021). The vertical growth rate was found to be less noisy and had an exponent of 0.68, again exceeding 0.5.

The vertical scalar flux statistics have comparable magnitudes between turbulent and advective values. At most points, the magnitude of the advective fluxes are larger than that of the turbulent fluxes but they stay within the same order of magnitude. The advective fluxes show much more local variation than the turbulent fluxes and vary between positive and negative across the city model, whereas the turbulent fluxes are, generally, uniformly positive.

7.2 Main Novel Contributions

The results of these studies have helped advance our experimental capabilities and theoretical understanding in several ways.

The developments into the PLIF methodology (chapter 4) enabled the subsequent studies in this thesis (chapters 5 and 6) to be carried out to an acceptable level of accuracy. They have also provided insights into good practice for carrying out an experimental technique that is not studied as extensively within the aerospace community as other optical techniques. It is hoped that when the validation data of the PLIF technique is published it will increase trust and perception of PLIF within groups that would normally use more long-standing techniques like fast flame ionisation. The release of the Matlab PLIF code on Github will allow for more research groups to begin working with PLIF measurements.

The study into scalar dispersion around an individual building provides value to the scientific community due to the relatively low amount of literature studying idealised bluff bodies that includes scalar dispersion measurements. More specifically, very little of the existing literature is also experimental due to the difficulties in fully mapping a plume experimentally without the PLIF technique. The insights from this study have provided a new perspective on scalar interactions with flow structures around a bluff body, which draws attention to the leading edge stagnation point. The structures visible in the turbulent fluxes in the wake of the building are also of interest.

This thesis was focused around working towards the Southampton city study and, as such, it represents the largest section of work. It was carried out because full fields of scalar fluxes have never been experimentally measured over a realistic city model, as was done here. Therefore, this is a unique dataset and a valuable reference for the point measurements and computational studies done by other groups. The dataset has already shown insights into relative strengths of scalar fluxes, and draws attention to the plume deflection possible above a city model like this.

This project has also created several resources that might in future be useful for collaborative studies or for other group members.

7.2.1 Papers

- 1. Modelling Pollutant Dispersion around an Individual Tall Building (**Published**)
 The content of this paper was included in full in chapter 5. This paper has been published in Boundary-Layer Meteorology.
- 2. A Planar Laser Induced Fluorescence Software Package (In review)

 The content of this draft paper has been included in chapter 4.1. This paper has been submitted to the Journal of Open Source Software and is currently in review.
- 3. Scale-model experiments of turbulent dispersion over a realistic urban environment (**Future Work**)
 - The content of this draft paper has been included in chapter 6. This paper will soon be submitted to Building and the Environment.
- 4. Assessing the accuracy of the Planar Laser Induced Fluorescence technique using a Mass Balance experimental case (**Future Work**)
 - The content of this draft paper has been included in section 4.2. This paper is still being written currently and finishing it is intended for future work. Experiments and data analysis has been completed.

7.2.2 Conferences Attended

- Urban Fluid Mechanics Special Interest Group Meeting, September 2022, University of Reading - Poster
- 2. UK Fluid Conference, September 2022, University of Sheffield Presentation
- 3. Urban Fluid Mechanics Special Interest Group Meeting, April 2023, University of Surrey Poster
- 4. Wind Engineering Society Research Day, June 2023, University of Southampton Presentation
- 5. European Turbulence Conference, September 2023, University of Valencia Presentation
- 6. UK Fluid Conference, October 2023, University of Glasgow Presentation
- 7. Turbulence and Shear Flow Phenomena Symposium, July 2024, McGill University (Montreal) Presentation
- 8. UK Fluid Conference, September 2024, Swansea University Presentation

7.3. Future Work 103

7.2.3 Awards

During this PhD I won second place poster at the University of Southampton's Aeronautic / Astronautic research day, and second best student presentation at the Wind Engineering Society Research Day 2023. This second award gave me the opportunity to present my work at an Institute of Civil Engineers evening lecture in London, in February 2024.

7.3 Future Work

Research into dispersion over urban landscapes has progressed; however, one of the most significant unsolved problem is still bridging the gap between idealised and realistic models. The devolution of the complex urban model into the less complex aspects of roughness, neighborhood scale order, and tall buildings that is suggested in chapter 6 is a step in the right direction. There is still work to do towards the accurate modelling of sub-canopy urban flows, and particularly turbulent dispersion. However, in this thesis research has been carried out that both made progress towards understanding these flows, and enabled the further research of others.

A large assumption that has been made in all experiments carried out in this paper is the absence of buoyant effects on dispersion and turbulence. In a real city, an urban heat island would cause a thermally buoyant plume which would have some effect on a plume. It is important that similar experiments be carried out with that thermal plume present.

Looking further towards the future, it is important that work is continued into gathering more real-world data. This will allow the results of experimental studies, like those carried out in this thesis, to be useful in explaining pollution in real cities.

References

- Adrian RJ, Westerweel J (2011) Particle image velocimetry. 30 Cambridge university press
- Arya SP, et al. (1999) Air pollution meteorology and dispersion ,vol 310. Oxford University Press New York
- Baj P, Bruce PJ, Buxton OR (2016) On a PLIF quantification methodology in a nonlinear dye response regime. Experiments in Fluids 57(6):1–19
- Barlow JF (2014) Progress in observing and modelling the urban boundary layer. Urban Climate 10:216–240
- Barlow JF, Coceal O (2009) Meteorology research and development a review of urban roughness sublayer turbulence. Met Office technical report 527
- Bermous I, Steinle P (2015) Efficient performance of the met office unified model v8.2 on intel xeon partially used nodes. Geoscientific Model Development 8:769–779
- Best MJ (2005) Representing urban areas within operational numerical weather prediction models. Boundary-Layer Meteorology 114(1):91–109
- Boppana VB, Xie ZT, Castro IP (2010) Large-eddy simulation of dispersion from surface sources in arrays of obstacles. Boundary-Layer Meteorology 135(3):433–454
- Braun AL, Awruch AM (2009) Aerodynamic and aeroelastic analyses on the caarc standard tall building model using numerical simulation. Computers and Structures 87:564–581
- Britter RE, Hanna SR (2003) Flow and dispersion in urban areas. Annual Review of Fluid Mechanics 35:469–496
- Bruchhausen M, Guillard F, Lemoine F (2005) Instantaneous measurement of two-dimensional temperature distributions by means of two-color planar laser induced fluorescence (PLIF). Experiments in Fluids 38(1):123–131
- Buch KA, Dahm WJ (1996) Experimental study of the fine-scale structure of conserved scalar mixing in turbulent shear flows. part 1. sc [gt] 1. Journal of Fluid Mechanics 317:21–71

Bush M, Allen T, Bain C, Boutle I, Edwards J, Finnenkoetter A, Franklin C, Hanley K, Lean H, Lock A, Manners J, Mittermaier M, Morcrette C, North R, Petch J, Short C, Vosper S, Walters D, Webster S, Weeks M, Wilkinson J, Wood N, Zerroukat M (2020) The first Met Office Unified Model-JULES Regional Atmosphere and Land configuration, RAL1. Geoscientific Model Development 13(4):1999–2029

- Cambridge Environmental Research Consultants (2023) Adms 6 atmospheric dispersion modelling system user guide cerc adms 6 atmospheric dispersion modelling system user guide. www.cerc.co.uk
- Carpentieri M, Corti A, Zipoli L (2004) Wind tunnel experiments of tracer dispersion downwind from a small-scale physical model of a landfill. Environmental Modelling and Software 19:881–885
- Carpentieri M, Hayden P, Robins AG (2012) Wind tunnel measurements of pollutant turbulent fluxes in urban intersections. Atmospheric Environment 46:669–674
- Castro IP, Robins AG (1977) The flow around a surface-mounted cube in uniform and turbulent streams. Journal of Fluid Mechanics 79:307–335
- Castro IP, Vanderwel C (2021) Turbulent flows: an introduction. IOP Publishing
- Cheng H, Castro IP (2002) Near wall flow over urban-like roughness. Boundary-Layer Meteorology 104:229–259
- City of London (2022) City of London, Micro climate Guidelines kernel description. https:
 - //www.cityoflondon.gov.uk/services/planning/microclimate-guidelines
- Clements D, Coburn M, Cox SJ, Bulot FMJ, Xie ZT, Vanderwel C (2024) Comparing large-eddy simulation and gaussian plume model to sensor measurements of an urban smoke plume. Atmosphere 15:1089
- Cowell N, Baldo C, Chapman L, Bloss W, Zhong J (2024) What can we learn from nested iot low-cost sensor networks for air quality? a case study of pm2.5 in birmingham, uk. Meteorological Applications 31
- Cowen EA, Chang KA, Liao Q (2001) A single-camera coupled PTV-LIF technique. Experiments in Fluids 31(1):63–73
- Crimaldi JP (2008) Planar laser induced fluorescence in aqueous flows. Experiments in Fluids 44:851–863
- Djenidi L, Antonia RA, Amielh M, Anselmet F (2008) A turbulent boundary layer over a two-dimensional rough wall. Experiments in Fluids 44:37–47
- Dziubanek G, Spychała A, Marchwińska-Wyrwał E, Rusin M, Hajok I, Ćwieląg-Drabek M, Piekut A (2017) Long-term exposure to urban air pollution and the relationship with life expectancy in cohort of 3.5 million people in Silesia. Science of the Total Environment 580:1–8

Elshaer A, Aboshosha H, Bitsuamlak G, Damatty AE, Dagnew A (2016) Les evaluation of wind-induced responses for an isolated and a surrounded tall building. Engineering Structures 115:179–195

- EPA US (1981) Guideline for fluid modeling of atmospheric diffusion. EPA, Office of Air Quality Planning and Standards, Research Triangle Park
- European Cooperation in Science and Technology (2015) Cost es1006 model evaluation case studies: approach and results cost action es1006 evaluation, improvement and guidance for the use of local-scale emergency prediction and response tools for airborne hazards in built environments. https://www.mi.uni-hamburg.de/en/arbeitsgruppen/windkanallabor/documents.html
- Fackrell JE, Robins AG (1982a) Concentration fluctuations and fluxes in plumes from point sources in a turbulent boundary layer. Journal of Fluid Mechanics 117:1–26
- Fackrell JE, Robins AG (1982b) The effects of source size on concentration fluctuations in plumes. Boundary-Layer Meteorology 22(3):335–350
- Fernando HJ (2010) Fluid dynamics of urban atmospheres in complex terrain. Annual Review of Fluid Mechanics 42:365–389
- Fuka V, Xie ZT, Castro IP, Hayden P, Carpentieri M, Robins AG (2018) Scalar Fluxes Near a Tall Building in an Aligned Array of Rectangular Buildings. Boundary-Layer Meteorology 167(1):53–76
- Garratt JR (1994) The atmospheric boundary layer. Earth-Science Reviews 37(1-2):89-134
- Georgantopoulou CG, Georgantopoulos GA (2018) International Standard Atmosphere, in BS. Fluid Mechanics in Channel, Pipe and Aerodynamic Design Geometries 2 pp 251–258
- Goulart EV, Coceal O, Branford S, Thomas TG, Belcher SE (2016) Spatial and Temporal Variability of the Concentration Field from Localized Releases in a Regular Building Array. Boundary-Layer Meteorology 159(2):241–257
- Gregg W (1923) Standard Atmosphere. Report No. 147. NASA
- Grimmond CS, Oke TR (1999) Aerodynamic properties of urban areas derived from analysis of surface form. Journal of Applied Meteorology 38(9):1262–1292
- Hearst RJ, Gomit G, Ganapathisubramani B (2016) Effect of turbulence on the wake of a wall-mounted cube. Journal of Fluid Mechanics 804:513–530
- Heist DK, Brixey LA, Richmond-Bryant J, Bowker GE, Perry SG, Wiener RW (2009) The effect of a tall tower on flow and dispersion through a model urban neighborhood: Part 1. flow characteristics. Journal of Environmental Monitoring 11:2163–2170
- Hertwig D, Soulhac L, Fuka V, Auerswald T, Carpentieri M, Hayden P, Robins A, Xie ZT, Coceal O (2018) Evaluation of fast atmospheric dispersion models in a regular street network. Environmental Fluid Mechanics 18:1007–1044

Hertwig D, Gough HL, Grimmond S, Barlow JF, Kent CW, Lin WE, Robins AG, Hayden P (2019) Wake characteristics of tall buildings in a realistic urban canopy. Boundary-Layer Meteorology 172(2):239–270

- Higuchi Y, Takeuchi K, Nunome Y, Tomioka S, Sakaki K, Kudo T, Hayakawa A, Kobayashi H (2019) Oh planar laser-induced fluorescence measurement for h2/o2 jet diffusion flames in rocket combustion condition up to 7.0 mpa. Journal of Thermal Science and Technology 14(2):Article 19–00,196
- Hoxey RP, Richards PJ (1992) Structure of the atmospheric boundary layer below 25 m and implications to wind loading on low-rise buildings. Journal of Wind Engineering and Industrial Aerodynamics 41(1-3):317–327
- Hu X, Morgans AS (2022) Attenuation of the unsteady loading on a high-rise building using feedback control. Journal of Fluid Mechanics 944:A10
- Jackson P (1981) On the displacement height in the logarithmic velocity profile. Journal of fluid mechanics 111:15–25
- Karasso PS, Mungal MG (1997) Plif measurements in aqueous flows using the nd: Yag laser. Experiments in Fluids 23:382–387
- Karra S, Malki-Epshtein L, Neophytou MK (2017) Air flow and pollution in a real, heterogeneous urban street canyon: A field and laboratory study. Atmospheric Environment 165:370–384
- Lim H, Vanderwel C (2023) Turbulent dispersion of a passive scalar in a smooth-wall turbulent boundary layer. Journal of Fluid Mechanics 969:A26
- Lim H, Hertwig D, Grylls T, Gough H, Reeuwijk Mv, Grimmond S, Vanderwel C (2022) Pollutant dispersion by tall buildings: laboratory experiments and large-eddy simulation. Experiments in Fluids 63(6):92
- Lim HC, Castro IP, Hoxey RP (2007) Bluff bodies in deep turbulent boundary layers: Reynolds-number issues. Journal of Fluid Mechanics 571:97–118
- Lim KE, Watkins S, Clothier R, Ladani R, Mohamed A, Palmer JL (2016) Full-scale flow measurement on a tall building with a continuous-wave doppler lidar anemometer. Journal of Wind Engineering and Industrial Aerodynamics 154:69–75
- Liu X, Zhang H, Wu S, Wang Q, He Z, Zhang J, Li R, Liu S, Zhang X (2022) Effects of buildings on wind shear at the airport: Field measurement by coherent doppler lidar. Journal of Wind Engineering and Industrial Aerodynamics 230:105,194
- Makedonas A, Carpentieri M, Placidi M (2021) Urban boundary layers over dense and tall canopies. Boundary-Layer Meteorology 181:73–93
- Martin D, Nickless G, Price C, Britter R, Neophytou M, Cheng H, Robins A, Dobre A, Belcher SE, Barlow JF, et al. (2010) Urban tracer dispersion experiment in london

(dapple) 2003: field study and comparison with empirical prediction. Atmospheric Science Letters 11(4):241–248

- Martinuzzi R, Tropea C (1993) The flow around surface-mounted, prismatic obstacles placed in a fully developed channel flow. Journal of Fluids Engineering 115:115(1): 85–92
- Marucci D, Carpentieri M (2020) Dispersion in an array of buildings in stable and convective atmospheric conditions. Atmospheric Environment 222:117,100
- Matthews JC, Coburn M, Khan MAH, Shallcross DE, Xie ZT (2024) Sensor measurements and large-eddy simulation of point source plumes over a complex urban terrain. 14th UK Conference on Wind Engineering. https://eprints.soton.ac.uk/493282/1/52Matthews.pdf
- Met Office (2016) Our Supercomputer for Climate and Weather Forecasting. https://www.metoffice.gov.uk/about-us/who-we-are/innovation/supercomputer
- Met Office (2022) The Cray XC40 supercomputing system kernel description. https://www.metoffice.gov.uk/about-us/what/technology/supercomputer
- Met Office (2024) Numerical weather prediction at the met office. https://www.metoffice.gov.uk/research/approach/modelling-systems/unified-model/weather-forecasting
- Milton-McGurk L, Williamson N, Armfield S, Kirkpatrick M (2020) Experimental investigation into turbulent negatively buoyant jets using combined piv and plif measurements. International Journal of Heat and Fluid Flow 82:108,561
- Ming De Gan B, Vanderwel C, Loxham M (2023) Simulation of outdoor air pollution in southampton. In: International Conference on Evolving Cities 2022
- Ono A, Nozu T (2024) Comparison between wind tunnel experiment and large-eddy simulation of concentration fluctuations in pollutant dispersion in a realistic urban area. Journal of Wind Engineering and Industrial Aerodynamics 253
- Owusu-Mfum S, Hudson MD, Osborne PE, Roberts TJ, Zapata-Restrepo LM, Williams ID (2023) Atmospheric pollution in port cities. Atmosphere 14(7):1135
- Placidi M, Ganapathisubramani B (2015) Effects of frontal and plan solidities on aerodynamic parameters and the roughness sublayer in turbulent boundary layers. Journal of Fluid Mechanics 782:541–566
- Plate EJ (1999) Methods of investigating urban wind fields-physical models. Atmospheric Environment 33:3981–3989
- Pope SB (2001) Turbulent Flowsvol 12. Cambridge University Press
- Rich T, Vanderwel C (2024) Pollutant dispersion around a single tall building. Boundary-Layer Meteorology 190(8):34

- Rich T (2024) A Planar Laser Induced Fluorescence Software Package. https://github.com/TomosRich/PLIF-Processing
- Rossi R (2010) A numerical study of algebraic flux models for heat and mass transport simulation in complex flows. International Journal of Heat and Mass Transfer 53:4511–4524
- Samad A, Kiseleva O, Holst CC, Wegener R, Kossmann M, Meusel G, Fiehn A, Erbertseder T, Becker R, Roiger A, Stanislawsky P, Klemp D, Emeis S, Kalthoff N, Vogt U (2023) Meteorological and air quality measurements in a city region with complex terrain: influence of meteorological phenomena on urban climate. Meteorologische Zeitschrift 32:293–315
- Sarathi P, Gurka R, Kopp GA, Sullivan PJ (2012) A calibration scheme for quantitative concentration measurements using simultaneous PIV and PLIF. Experiments in Fluids 52(1):247–259
- da Silva CB, Pereira JC (2007) Analysis of the gradient-diffusion hypothesis in large-eddy simulations based on transport equations. Physics of Fluids 19:035,106
- Soulhac L, Perkins RJ, Salizzoni P (2008) Flow in a street canyon for any external wind direction. Boundary-Layer Meteorology 126:365–388
- Sousa J, García-Sánchez C, Gorlé C (2018) Improving urban flow predictions through data assimilation. Building and Environment 132:282–290
- Southampton City Council (2021) Southampton air quality report kernel description. https://www.southampton.gov.uk/environmental-issues/pollution/air-quality/monitoring-and-reporting/air-quality-reports/
- Swinehart DF (1962) The beer-lambert law. Journal of chemical education 39(7):333
- Sützl BS, Rooney GG, Finnenkoetter A, Bohnenstengel SI, Grimmond S, v Reeuwijk M (2021) Distributed urban drag parametrization for sub-kilometre scale numerical weather prediction. Quarterly Journal of the Royal Meteorological Society 147:3940–3956
- Talluru KM, Philip J, Chauhan KA (2018) Local transport of passive scalar released from a point source in a turbulent boundary layer. Journal of Fluid Mechanics 846:292–317
- Tomas JM, Eisma HE, Pourquie MJ, Elsinga GE, Jonker HJ, Westerweel J (2017) Pollutant Dispersion in Boundary Layers Exposed to Rural-to-Urban Transitions: Varying the Spanwise Length Scale of the Roughness. Boundary-Layer Meteorology 163(2):225–251
- Tominaga Y, Stathopoulos T (2011) CFD modeling of pollution dispersion in a street canyon: Comparison between LES and RANS. Journal of Wind Engineering and Industrial Aerodynamics 99(4):340–348

Tominaga Y, Stathopoulos T (2012) Cfd modeling of pollution dispersion in building array: Evaluation of turbulent scalar flux modeling in rans model using les results. Journal of Wind Engineering and Industrial Aerodynamics 104-106:484–491

- Torres P, Le Clainche S, Vinuesa R (2021) On the Experimental, Numerical and Data-Driven Methods to Study Urban Flows. Energies 14(5):1310
- UK Government (2023) Air Quality Strategy. https://www.gov.uk/government/publications/the-air-quality-strategy-for-england/air-quality-strategy-framework-for-local-authority-delivery
- UK Government (2024) Public Health England Air Pollution.

https://www.gov.uk/government/publications/health-matters-air-pollution/health-matters-air-pollution

- United Nations (2015) Transforming our world: the 2030 agenda for sustainable development. United Nations: New York, NY, USA
- United Nations Department of Economic and Social Affairs (2018) 68% of the world population projected to live in urban areas by 2050, says UN kernel description. https://www.un.org/development/desa/en/news/population/2018-revision-of-world-urbanization-prospects.html
- US Environmental Protection Agency (2004) Aermod model formulation. https://gaftp.epa.gov/Air/aqmg/SCRAM/models/preferred/aermod/aermod_mfd.pdf
- US Environmental Protection Agency (2021) Aerscreen user's guide. https://www.epa.gov/scram/air-quality-dispersion-modeling-screening-models
- US National Oceanic and Atmospheric Administration (2013) Aloha (areal locations of hazardous atmospheres) 5.4.4: Technical documentation. https://www.epa.gov/cameo/aloha-software
- Van Buren T, Williams O, Smits AJ (2017) Turbulent boundary layer response to the introduction of stable stratification. Journal of Fluid Mechanics 811(1):569–581
- Vanderwel C, Ganapathisubramani B (2019) Turbulent Boundary Layers Over Multiscale Rough Patches. Boundary-Layer Meteorology 172(1):1–16
- Vanderwel C, Tavoularis S (2014) Measurements of turbulent diffusion in uniformly sheared flow. Journal of Fluid Mechanics 754:488–514
- Vanderwel C, Tavoularis S (2016) Scalar dispersion by coherent structures in uniformly sheared flow generated in a water tunnel. Journal of Turbulence 17(7):633–650
- Vanderwel C, Simmonds O, Peng ZX (2024) Identifying regional air quality trends from sensor network data . University of Southampton.

https://eprints.soton.ac.uk/494987/

Williams M, Barrowcliffe R, Laxen D, Monks P (2011) Review of air quality modelling in defra. A report by the Air Quality Modeling Review Steering Group p 1:44

World Health Organisation (2021) WHO air quality guidelines kernel description. https://www.c40knowledgehub.org/s/article/WHO-Air-Quality-Guidelines? language=en_US

- Xie ZT, Coceal O, Castro IP (2008) Large-Eddy simulation of flows over random urban-like obstacles. Boundary-Layer Meteorology 129(1):1–23
- Zhao R, Feng Z, Dan D, Wu Y, Li X (2022) Numerical simulation of caarc standard high-rise building model based on mrt-lbm large eddy simulation. Shock and Vibration 2022(1):1907,356